

Arbeitsbericht NAB 14-16

Long-term Evolution of the Engineered Gas Transport System

November 2014

G. Kosakowski & P. Smith

Nationale Genossenschaft
für die Lagerung
radioaktiver Abfälle

Hardstrasse 73
CH-5430 Wettingen
Telefon 056-437 11 11

www.nagra.ch

Arbeitsbericht NAB 14-16

Long-term Evolution of the Engineered Gas Transport System

November 2014

G. Kosakowski¹ & P. Smith²

¹Paul Scherrer Institute

²Safety Assessment Management (Switzerland)

KEYWORDS

SGT-E2, Engineered gas transport system, EGTS, L/ILW, modelling, 1-D model, 2-D model, repository-generated gas

Nationale Genossenschaft
für die Lagerung
radioaktiver Abfälle

Hardstrasse 73
CH-5430 Wetingen
Telefon 056-437 11 11

www.nagra.ch

Nagra Working Reports concern work in progress that may have had limited review. They are intended to provide rapid dissemination of information. The viewpoints presented and conclusions reached are those of the author(s) and do not necessarily represent those of Nagra.

"Copyright © 2014 by Nagra, Wettingen (Switzerland) / All rights reserved.

All parts of this work are protected by copyright. Any utilisation outwith the remit of the copyright law is unlawful and liable to prosecution. This applies in particular to translations, storage and processing in electronic systems and programs, microfilms, reproductions, etc."

Summary

An "engineered gas transport system" (EGTS), i.e. a backfill and sealing system that allows the controlled transport of gases along the access structures, is an option to limit the gas pressure in a repository for low- and intermediate-level waste (L/ILW) and in the emplacement rooms for long-lived intermediate level waste in a high-level waste repository. This report assesses whether such a system, suitably designed, will function as required over a 100 000 year time frame, taking relevant chemical interactions into account.

It is currently foreseen that high-porosity cementitious mortars will be used as backfill materials for the emplacement rooms and sand/bentonite mixtures will be used to backfill and seal the access tunnels. If these materials were to be in direct contact, there is a possibility that long-term mineralogical changes and corresponding changes in porosity could occur. This could result in the pore spaces becoming clogged and, in an extreme case, in the materials locally becoming impermeable to gas. Of particular relevance is the formation of calcium silicate hydrate (C-S-H) precipitates from the reaction of dissolved Si, released from sand/bentonite when exposed to high pH pore fluid from the cement, with dissolved Ca released from the cement minerals. A transition layer between the cementitious mortars and the sand/bentonite, of suitable length and filled with a suitable material, is a possibility to avoid or reduce such unfavourable chemical interactions.

In the present report, an example EGTS design is considered in which limestone gravel is used to fill the transition layer. This choice of limestone (with calcite as the key mineral) is motivated by the fact that bentonite, cement and Opalinus Clay all contain small amounts of this mineral, and are in thermodynamic equilibrium with it. Geochemical gradients between cementitious and other backfill materials are however not completely avoided by this choice. Their impacts are analysed in illustrative calculations of the evolution of mineralogy and porosity using state-of-the-art coupled reactive transport modelling. Two types of calculations are carried out: simplified 1-D calculations and more realistic 2-D calculations. The 1-D calculations are performed for a simplified system with fully saturated conditions, considering only diffusive transport. The 2-D calculations are performed for partially saturated conditions and include advective as well as diffusive transport. In the modelling work described in the present report, cementitious materials are represented as a generic concrete of average composition, with limestone aggregate. Furthermore, the limestone in the aggregate and in the transition layer is represented as calcite for simplicity.

The 1-D calculations for the example EGTS design indicate that porosity changes are relatively minor and caused either by the replacement of mineral phases with phases that have a different molar volume, or by spatially distributed precipitation of minerals due to diffusive mixing of solutes originating from different materials. A portlandite dissolution front is observed in the concrete and a montmorillonite dissolution front in the sand/bentonite, both of which migrate away from the interfaces with the transition layer over time. As a result of the release of Ca and Si from these migrating fronts, C-S-H precipitation is observed. This precipitation is not, however, highly localised at the material interfaces, but rather is widely distributed across the transition layer. Changes in porosity are small and there are no indications for porosity clogging in the calculations. Montmorillonite dissolution could have a potential detrimental effect on the radionuclide retention properties of the affected sand/bentonite. However, the migration of the montmorillonite dissolution front is limited to just a few metres over 100 000 years and thus only a small part of the access tunnel system backfilled with sand/ bentonite is affected.

On the basis of earlier modelling studies of the saturation of the L/ILW repository, the 2-D model addresses a scenario in which water flows from the sand/bentonite-filled access tunnel system along the lower part of the partially saturated transition layer towards the emplacement rooms, leading to advective as well as diffusive transport. The earlier studies suggest that such flows will persist for about 1000 years during the early evolution of the repository, but the 2-D model represents the hypothetical, more extreme case where the flows are maintained up to 100 000 years. The results indicate that the main chemical interactions, and hence mineralogical and porosity changes, occur in the saturated material at the bottom of the modelled system, as in the 1-D calculations. However, the 2-D model also demonstrates that changes in the partially saturated materials towards the top of the modelled system are much more limited than towards the bottom, where materials are fully saturated.

A limited sensitivity analysis is also carried out to examine the influence of the length of the transition layer on the evolution of the system. Progress of dissolution fronts in the concrete and in the sand/bentonite is found to depend on the length of the transition layer within the modelled time period. Porosity changes remain small across the range of transition layer lengths considered. Sensitivity to the use of quartz as an alternative fill material for the transition layer and as an alternative concrete aggregate material is also examined, to provide insight into possible consequences in terms of mineralogical and porosity changes when materials within the EGTS are not in thermodynamic equilibrium. When quartz aggregate is used, the most significant mineralogical changes are those that occur in the concrete, where large amounts of C-S-H precipitation occur. The precipitates are, however, distributed fairly broadly throughout the concrete, and there are no indications that these could lead to pore clogging. When, in addition, quartz gravel is used to fill the transition layer, no significant further changes in mineralogical evolution are observed.

Overall, qualitative reasoning and quantitative illustrative analyses indicate that, for an appropriately chosen EGTS design, chemical interactions will not lead to a significant reduction in porosity and to a loss of gas permeability, and the EGTS should function as required over a 100 000 year time frame.

Zusammenfassung

Ein "Engineered Gas Transport System" (EGTS), d.h. ein System aus Verfüll- und Versiegelungsbauwerken zur kontrollierten Ableitung von Gasen entlang der Zugangsbauwerke, ist eine Möglichkeit, um den Gasdruck in den Lagerkammern eines geologischen Tiefenlagers für schwach- und mittelaktive Abfälle (SMA) bzw. für langlebige mittelaktive Abfälle zu begrenzen. Der vorliegende Bericht untersucht, ob ein geeignet ausgelegtes EGTS über einen Zeitraum von 100'000 Jahren wie vorgesehen funktioniert, unter Berücksichtigung der massgeblichen chemischen Prozesse.

Es ist vorgesehen, die Hohlräume in den SMA-Lagerkammern mit hochporösem Zementmörtel und die Zugangsbauwerke mit Sand/Bentonitmischungen zu verfüllen bzw. zu versiegeln. Wenn sich beide Materialien in direktem Kontakt befinden, besteht die Möglichkeit, dass langfristige mineralogische Umwandlungen den Porenraum in der Kontaktzone verschliessen. Im Extremfall könnte der Porenraum undurchlässig für Gas werden. Eine wahrscheinliche Reaktion ist die Bildung von Calciumsilikathydraten (C-S-H). Das benötigte Calcium wird aus dem Mörtel freigesetzt und diffundiert zur Kontaktzone, wo es mit Silizium reagiert, das aus Auflösungsprozessen in den Sand/Bentonitmischungen unter dem Einfluss von basischen Zementwässern stammt. Eine Übergangsschicht, die aus geeigneten Materialien besteht und einen ausreichenden Abstand zwischen den zementhaltigen Materialien und der Sand/Bentonitmischung gewährleistet, ist eine Möglichkeit, die nachteiligen Mineralreaktionen zu vermeiden oder zumindest abzuschwächen.

Im vorliegenden Bericht wird ein beispielhaftes EGTS mit einer Übergangsschicht aus Kalksteinschotter (mit Calcit als Hauptbestandteil) untersucht. Zusätzlich wird angenommen, dass auch der Zuschlagstoff des Verfüllmörtels aus dem gleichen Material besteht. Calcit ist in kleinen Anteilen im Opalinuston, im Zement und im Bentonit enthalten und diese Materialien sind chemisch mit Calcit im Gleichgewicht. Geochemische Gradienten zwischen zementhaltigen Materialien und anderen Verfüllmaterialien können allerdings auch durch eine solche Materialwahl nicht vollständig vermieden werden. Der Einfluss solcher Gradienten auf die Entwicklung der Mineralogie und Porosität in den verwendeten Materialien wird mit Hilfe von *state-of-the-art* numerischen Modellrechnungen illustriert, welche chemische Prozesse und Stofftransport miteinander koppeln. Zwei Modellierungsansätze wurden verwendet: Vereinfachende 1-D-Modelle wurden für die Berechnung von Mineralreaktionen in Kombination mit diffusivem Stofftransport in vollständig wassergesättigten Medien angewendet. Ein aufwändigerer 2-D-Modellansatz wurde zur Berechnung von Mineralreaktionen auf Grund von diffusivem und advektivem Stofftransport in nur teilweise wassergesättigten Systemen verwendet.

Die 1-D-Modelle für das beispielhafte EGTS zeigen auf, dass die Porositätsänderungen, verursacht entweder durch Austausch von Mineralphasen mit anderen Phasen, welche ein anderes molares Volumen haben, oder durch räumlich verteilte Ausfällung von Mineralien aufgrund der Mischung von Porenwässern aus den verschiedenen Materialien, relativ geringfügig sind. Sowohl in den zementhaltigen Materialien als auch in den Sand/Bentonitmischungen sind Mineralauflösungs- und Mineralneubildungsfronten sichtbar, die zur Bildung von C-S-H führen. Diese Mineralphasen werden allerdings nicht lokalisiert an Materialgrenzflächen abgelagert, sondern sie werden räumlich verteilt in der Übergangsschicht ausgeschieden. Die Computersimulationen zeigen nur geringfügige Änderungen der Porosität, die nicht ausreichen, um zu einer Versiegelung des Porenraums zu führen. Die grossräumige Auflösung des Tonanteils im Bentonit könnte zu einer Beeinträchtigung der Radionuklidrückhaltung für den betroffenen Bereich der Sand/Bentonitverfüllung führen. Allerdings ist die Auflösung auf wenige Meter in einem Zeitraum von 100'000 Jahren beschränkt, so dass nur ein kleiner Teil der mit Sand/Bentonitmischungen verfüllten und versiegelten Zugangsbauwerke betroffen ist.

Das 2-D-Modell simuliert ein Szenario mit diffusivem und advektivem Stofftransport, bei dem das Wasser von den mit Sand/Bentonit verfüllten bzw. versiegelten Zugangsbauwerken zuerst entlang der Sohle durch die Übergangsschicht und dann in die mit Zementmörtel verfüllten Lagerkammern fliesst. Frühere Modellierungsstudien haben aufgezeigt, dass solche Wasserflüsse nur bis etwa 1000 Jahre nach dem Verschluss des Tiefenlagers auftreten. Das 2-D-Modell berechnet einen hypothetischen und extremen Fall, in dem angenommen wird, dass solche Wasserflüsse bis zu 100'000 Jahre andauern. Die 2-D-Modelle zeigen in dem vollständig wassergesättigten unteren Modellbereich ähnliche chemische Reaktionen wie die 1-D-Modelle. Insbesondere die Mineralreaktionen und Porositätsänderungen in den mit zementhaltigen Materialien verfüllten Lagerkammern sind in beiden Modellansätzen ähnlich. Das 2-D-Modell zeigt aber auch, dass der Umfang und die Intensität der mineralogischen Umwandlungen und der damit verbundenen Porositätsänderungen stark von der Wassersättigung abhängen. In den teilgesättigten Materialien in den oberen Bereichen des Modellgebiets fallen solche Änderungen viel geringer aus als in den vollgesättigten Materialien in den unteren Bereichen des Modellgebiets.

Der Einfluss der Dimensionierung (Länge) der Übergangsschicht auf die Entwicklung des EGTS wurde mit einer eingeschränkten Sensitivitätsstudie untersucht. Sowohl in den zementhaltigen Verfüllmaterialien als auch in den Sand/Bentonitmischungen hängt der Fortschritt der Reaktionsfronten von der Länge der Übergangsschicht ab. Längere Übergangsschichten verlangsamen die Materialauflösung (d.h. den Fortschritt der Reaktionsfronten). Für die untersuchten Längen der Übergangsschicht sind Porositätsänderungen minimal. Um aufzuzeigen, welche Konsequenzen die Wahl von Materialien für das EGTS hätte, welche nicht im thermodynamischen Gleichgewicht sind, wurden auch Fälle untersucht, in welchen Quarz als alternatives Material in der Übergangsschicht und als Zuschlagsstoff im Verfüllmörtel angenommen wurde. Für letzteren Fall ist die massgebliche Auswirkung die Ausfällung von grösseren Mengen an C-S-H im Verfüllmörtel. Die Ausfällungen sind aber gleichmässig im Mörtel verteilt und es gibt keine volumetrisch begründeten Hinweise, dass dies zu einem Porenverschluss führen könnte. Bei einem Rechenfall, bei dem zusätzlich auch Quarzkies in der Übergangsschicht verwendet wurde, konnten keine weiteren Änderungen in der mineralogischen Entwicklung beobachtet werden.

Die qualitativen Argumente und die quantitativen Beispielrechnungen in diesem Bericht zeigen, dass in einem geeignet ausgelegten EGTS die chemischen Reaktionen nicht zu einer signifikanten Porositätsreduktion mit einem Verlust der Gasdurchlässigkeit führen werden, und dass ein solches EGTS auch über einen Zeitraum von 100'000 Jahren wie vorgesehen funktionieren wird.

List of Contents

Summary	I
Zusammenfassung.....	III
List of Contents.....	V
List of Tables.....	VII
List of Figures	VIII
1 Introduction	1
1.1 Background and aims	1
1.2 Repository concept	2
1.3 Mineralogical evolution and the issue of clogging	3
1.4 Methodology to evaluate long-term evolution of the Engineered Gas Transport System.....	5
1.5 Structure of this report	6
2 Design of the Engineered Gas Transport System	7
2.1 General features	7
2.2 Design variables	8
3 Evaluation of evolution for an example design for an Engineered Gas Transport System.....	9
3.1 Example design and its rationale	9
3.2 Illustrative 1-D calculation of evolution for a saturated system	9
3.2.1 Model domain and main model assumptions	9
3.2.2 Model implementation.....	11
3.2.3 Calculation results	11
3.2.4 Interpretation of results.....	15
3.3 Impact of initial partial saturation: illustrative 2-D calculation.....	17
3.3.1 Model domain and additional model assumptions	18
3.3.2 Model implementation.....	21
3.3.3 Evolution of saturation	22
3.3.4 Evolution of porewater chemistry and mineralogy.....	24
3.3.5 Interpretation of results.....	31
3.4 Main findings for the example design	33
4 Sensitivity to Design Variables	35
4.1 Sensitivity to length extent of the transition layer	35
4.2 Sensitivity to choice of filling material for transition layer and concrete aggregate.....	39
4.2.1 Calculation cases	39
4.2.2 Calculation results	40

4.2.3	Interpretation of results.....	48
4.3	Main findings of the sensitivity analyses.....	49
5	Conclusions	53
6	References	55
Appendix A: Details of Numerical Models A-1		
A.1	Governing equations for flow and transport.....	A-1
A.2	Coupling to the chemical system and evaluation of porosity changes	A-2
A.3	Material and thermodynamic setup and initial porewater compositions	A-3
A.4	Implementation of kinetic control	A-5
Appendix B: Additional Parameter Values B-1		
B.1	Flow and transport parameters.....	B-1
B.2	Kinetic parameters for 1-D calculations	B-4
B.3	Kinetic parameters for 2-D calculations	B-4
Appendix C: Additional Calculation Cases C-1		
C.1	1-D modelling of the case with a hypothetical inert concrete aggregate.....	C-1
C.2	2-D modelling of the case with quartz-filled transition layer and quartz aggregate.....	C-2
C.2.1	Porewater chemistry and mineralogy after 1000 years.....	C-3
C.2.2	Longer-term evolution.....	C-9
C.2.3	Increased inflow from the access tunnel system.....	C-13
Appendix D: Model Accuracy and Uncertainties D-1		
D.1	Influence of mesh size on porosity evaluation.....	D-1
D.2	Equilibrium chemistry vs. kinetic control of precipitation/dissolution	D-3
D.3	Numerical oscillations in the simulations.....	D-7
D.4	CO ₂ migration in the gas phase.....	D-9
D.5	Mechanical effects.....	D-10
Appendix E: Thermodynamic Data E-1		
E.1	Thermodynamic data for the 1-D modelling	E-1
E.2	Thermodynamic data for the 2-D modelling	E-5

List of Tables

Tab. A-1:	Material composition from Kosakowski & Berner (2011) in terms of mass fractions for 1-D calculations.	A-3
Tab. A-2:	Initial porewater composition for sand/bentonite, sand/gravel and concrete (Kosakowski & Berner 2011).	A-4
Tab. A-3:	Water balance, cation exchange capacity (CEC) and porosity of sand/bentonite mixture (Kosakowski & Berner 2011).	A-5
Tab. B-1:	Comparison of two-phase flow Van Genuchten input parameters (liquid phase only) for OpenGeoSys and TOUGH 2.	B-1
Tab. B-2:	Conversion of TOUGH 2 input parameters (Senger & Ewing 2009) to OpenGeoSys.	B-2
Tab. B-3:	Transport parameters for the 2-D calculations.	B-3
Tab. B-4:	Kinetic parameters used in 1-D calculations. Mineral phases not listed were not kinetically controlled.	B-4
Tab. B-5:	Kinetic parameters used in 2-D calculations. Mineral phases not listed were not kinetically controlled.	B-4
Tab. C-1:	Kinetic parameters as used in the 1-D diffusive calculations that explore the influence of transition layer length.	C-1
Tab. E-1:	Thermodynamic data for Dependent Components (Species).	E-1
Tab. E-2:	Thermodynamic data for Dependent Components (Species).	E-5

List of Figures

Fig. 1-1:	Example layout for the L/ILW repository.	2
Fig. 1-2:	Porosity profile across a 5 year old interface between claystone and shotcrete (from Gaboreau et al. 2012).	4
Fig. 1-3:	Concept of a clogging interface between reactive quartz sand (or a sand/ bentonite mixture) (left) and concrete (right) in a diffusive transport regime.	4
Fig. 2-1:	Schematic illustration of an EGTS (modified from Nagra 2008c).	7
Fig. 3-1:	Main features and geometry for 1-D modelling.	10
Fig. 3-2:	Mineralogical profiles at different times across a 10 m long transition layer composed of calcite and the adjoining regions after 0, 1000, 20 000 and 100 000 years.	12
Fig. 3-3:	Evolution of porosity within a 10 m long transition layer composed of calcite and the adjoining regions.	14
Fig. 3-4:	Evolution of pH within a 10 m long transition layer composed of calcite and the adjoining regions.	14
Fig. 3-5:	Schematic illustration of major processes in an EGTS where concrete and sand/ bentonite compartments are separated by a 10 m layer of calcite gravel after 100 000 years.	15
Fig. 3-6:	pH dependence of calcite solubility calculated for a simple NaCl water (0.001 g NaCl per 1 kg water) with GEMS-PSI for data from PSI/Nagra TDB.	17
Fig. 3-7:	Main features and geometry for 2-D modelling.	18
Fig. 3-8:	Initial capillary pressure distribution in Pa (upper figure) and saturation distribution (lower figure) for 2-D modelling.	19
Fig. 3-9:	Figure 4-7 (left) and 4-17 (right) from Senger & Ewing (2009).	20
Fig. 3-10:	Evolution of saturation (from top to bottom): after 10 years, after 100 years, after 1000 years and after 100 000 years.	22
Fig. 3-11:	Mineralogical profiles along the top (upper picture) and the bottom (lower picture) of the model domain at 1000 years.	24
Fig. 3-12:	Mineralogical profiles along the top (upper picture) and the bottom (lower picture) of the model domain after 100 000 years.	25
Fig. 3-13:	Map of the spatial distribution of selected total component concentrations in the liquid phase at 100 000 years.	26
Fig. 3-14:	Map of the spatial distribution of main concrete mineral phases at 100 000 years.	28
Fig. 3-15:	Map of porosity distribution (top) and porosity change (bottom) at 100 000 years.	30
Fig. 3-16:	Map of pH at 100 000 years.	30
Fig. 3-17:	Schematic illustration of major processes in an EGTS where concrete and sand/ bentonite compartments are separated by a 10 m layer of calcite gravel according to the 2-D model.	31

Fig. 4-1:	Mineralogical profiles across a 1 m, a 2 m, a 5 m and a 10 m long layer (from top to bottom) composed of calcite after 2000 years.....	35
Fig. 4-2:	Progress of montmorillonite dissolution front in sand/bentonite and progress of portlandite dissolution front in concrete with time for different transition layer lengths (TLL).....	37
Fig. 4-3:	Progress of montmorillonite dissolution fronts in transition layer and in sand/bentonite with time for different transition layer lengths.	38
Fig. 4-4:	Overview of the three calculation cases analysed in this section.	39
Fig. 4-5:	Mineralogical profiles at different times across a 1 m long transition layer composed of calcite and the adjoining regions in a case where calcite aggregate in the concrete is replaced by quartz aggregate.....	42
Fig. 4-6:	Evolution of pH within a 1 m long transition layer composed of calcite and the adjoining regions in a case where calcite aggregate in the concrete is replaced by quartz aggregate.	44
Fig. 4-7:	Evolution of porosity within a 1 m long transition layer composed of calcite and the adjoining regions in a case where calcite aggregate in the concrete is replaced by quartz aggregate.	44
Fig. 4-8:	Mineralogical profiles at different times across a 1 m long transition layer composed of quartz gravel and the adjoining regions in a case where calcite aggregate in the concrete is replaced by quartz aggregate.....	45
Fig. 4-9:	Evolution of pH within a 1 m long transition layer composed of quartz gravel and the adjoining regions in a case where calcite aggregate in the concrete is replaced by quartz aggregate.	47
Fig. 4-10:	Evolution of porosity within a 1 m long transition layer composed of quartz gravel and the adjoining regions in a case where calcite aggregate in the concrete is replaced by quartz aggregate.	47
Fig. 4-11:	Solubility of SiO ₂ (quartz), as indicated by the concentration of total Si in solution, as a function of pH, calculated for a simplified system consisting of 5 200 g quartz, 1000 g water and 1 g NaCl.	49
Fig. 4-12:	Overview of the calculation cases analysed in this section and comparison of main observations with other model variants.	50
Fig. C-1:	Mineralogical profile at 300 years within a 5 m long transition layer composed of quartz gravel and the adjoining regions in a case where calcite aggregate in the concrete is replaced by an inert material.	C-2
Fig. C-2:	Initial mineralogy profile along the bottom of the model.....	C-2
Fig. C-3:	Concentrations [mol/m ³] of total dissolved Na (bottom) and Cl (top) in the porewater after 1000 years.....	C-3
Fig. C-4:	Concentrations [mol/m ³] of total dissolved Ca (bottom) and C (top) in the porewater after 1000 years.....	C-4
Fig. C-5:	Concentrations [mol/m ³] of total dissolved Si in the porewater after 1000 years.....	C-5
Fig. C-6:	Initial pH, and pH evolution at 50 years, 100 years, 500 years and 1000 years (from top to bottom).	C-6

Fig. C-7:	Mineralogical profiles after 1000 years (from bottom to top) at the bottom of the model and at the top of the model (height 5 m).....	C-7
Fig. C-8:	Porosity distribution after 1000 years.....	C-8
Fig. C-9:	Porosity profiles along the bottom (height = 0 m), the middle (height = 2.5 m) and the top (height = 5 m) of the model at 1000 years.....	C-8
Fig. C-10:	Porosity profiles along the bottom (height = 0 m) of the model with fine mesh (top: average node distance 0.1 m) and with coarse mesh (bottom: average node distance 0.5 m) after 1000 years simulation time.....	C-10
Fig. C-11:	Porosity profiles along the bottom (height = 0 m) of the model variants with different discretisation at 1000 years (coarse mesh: average node distance 0.5 m, fine mesh: average node distance 0.1 m).....	C-11
Fig. C-12:	Mineralogical profiles along the bottom (top) and the top (bottom) of the model domain after 100 000 years simulation time for the 2-D case with a coarse discretisation.....	C-12
Fig. C-13:	Porosity (at FE nodes) after 100 000 years.....	C-13
Fig. C-14:	pH (at FE nodes) after 100 000 years.....	C-13
Fig. C-15:	Mineralogical profiles after 1000 years (upper row) 100 000 years (lower row) from the 2-D model with a coarse discretisation and ten-fold increase in porewater inflow from the access tunnel system.....	C-14
Fig. C-16:	Concentration maps [mol/m^3] for gypsum, brucite, calcite and map of porosity (from top to bottom) after 100 000 years using the 2-D model with a coarse discretisation.....	C-15
Fig. C-17:	pH map after 100 000 years using the 2-D model with a coarse discretisation.....	C-16
Fig. D-1:	For nodes (N) and elements (E) where solute concentrations are fixed by mineral equilibria the concentration gradients between neighbouring nodes and elements may depend on the distance between nodes and element centers.....	D-2
Fig. D-2:	Progress of dissolution fronts for Na-montmorillonite with time.....	D-3
Fig. D-3:	Mineralogical profiles at different times (0, 100, 500 and 2000 years) across a 1 m long transition layer composed of quartz gravel and with quartz aggregate in the concrete.....	D-4
Fig. D-4:	Amount of C-S-H (upper figure) and Ca-Si ratio in the C-S-H phase (lower figure) on both sides of the interface between the transition layer (gravel) and the concrete, calculated with a model variant based principally on equilibrium chemistry and with a variant in which all mineral phases are kinetically controlled.....	D-5
Fig. D-5:	Porosity evolution near the material interfaces, calculated with a model variant based principally on equilibrium chemistry and with a variant in which all mineral phases are kinetically controlled.....	D-6
Fig. D-6:	pH evolution near the material interfaces, calculated with a model variant based principally on equilibrium chemistry and with a variant in which all mineral.....	D-7

Fig. D-7: Mineralogical profiles after 300 years for a model variant that implements solid solutions for hydrotalcite and ettringite (top) and a variant with single components phases of these minerals (bottom). D-8

1 Introduction

1.1 Background and aims

In Switzerland, the Nuclear Energy Law requires the disposal of all types of radioactive waste in deep geological repositories (KEG 2003). The Swiss Radioactive Waste Management Program (Nagra 2008a) foresees two types of deep geological repositories: a high-level waste repository (HLW repository¹) for spent fuel (SF)², vitrified high-level waste (HLW) and long-lived intermediate-level waste (ILW), and a repository for low- and intermediate-level waste (L/ILW repository³).

The present report, which concerns the use of an Engineered Gas Transport System (EGTS) to avoid excessive gas pressure build up in the L/ILW repository, is a supporting reference to the report on gas release from the L/ILW repository in the Opalinus Clay in the candidate siting regions of Northern Switzerland (Papafiotou & Senger 2014). Specifically, the present report looks at the long-term evolution of the EGTS taking relevant chemical interactions into account and investigates whether the EGTS can indeed be designed in such a way that it will function as required over the long time frame needed⁴. Although the present report focusses on Opalinus Clay, the key findings are also applicable to the other candidate host rocks for the L/ILW repository identified in Stage 1 of the Sectoral Plan⁵ (Nagra 2008b). Furthermore, the conclusions in this report are also applicable to ILW repository part of the HLW repository.

Gas generation in the L/ILW repository will occur as a result of anaerobic corrosion of metals (which produces H₂), degradation of organic matter (which may produce CO₂ and CH₄) and radiolysis of water (which principally produces H₂). The carbon dioxide is likely to react with cement minerals causing carbonation of the concrete materials in the emplacement rooms. The majority of the gases will, however, not react with concrete and other materials, and will accumulate in the repository emplacement rooms, before escaping via the host rock and the backfilled and sealed access tunnel system (the EGTS).

In the report Nagra (2008c), the concept of backfill and sealing materials designed and optimised to allow the controlled transport of gases along the repository access structures – the engineered gas transport system or EGTS – was introduced. Other design measures to manage repository generated gas are also possible (e.g. waste treatment to reduce the gas source term), but the EGTS, being the focus of the present report, is the only measure considered here.

The basic features of the EGTS are described in Chapter 2. To summarise, high-porosity cementitious mortars are to be used as backfill materials for the emplacement rooms and sand/bentonite mixtures are used to backfill and seal the access tunnels. Sand/bentonite mixtures with low bentonite content exhibit the favourable feature of low permeability to water, whereas gas permeability is significantly increased with respect to pure, compacted bentonite. Thus, the EGTS enables gas transport to take place through the access tunnel system without significant negative impact on the radionuclide retention function. A field experiment to test a gas-permeable seal for deep geological repositories (the GAST Project) is currently underway at the Grimsel Test Site.

¹ German: HAA-Lager.

² According to current legislation, spent fuel is classified as radioactive waste.

³ German: SMA-Lager.

⁴ For the L/ILW repository, the so-called "time period under consideration" ("Betrachtungszeitraum" in German) is 100 000 years (Nagra 2008d).

⁵ German: Sachplan Geologische Tiefenlager (SGT).

1.2 Repository concept

Fig. 1-1 shows an example layout for the L/ILW repository.

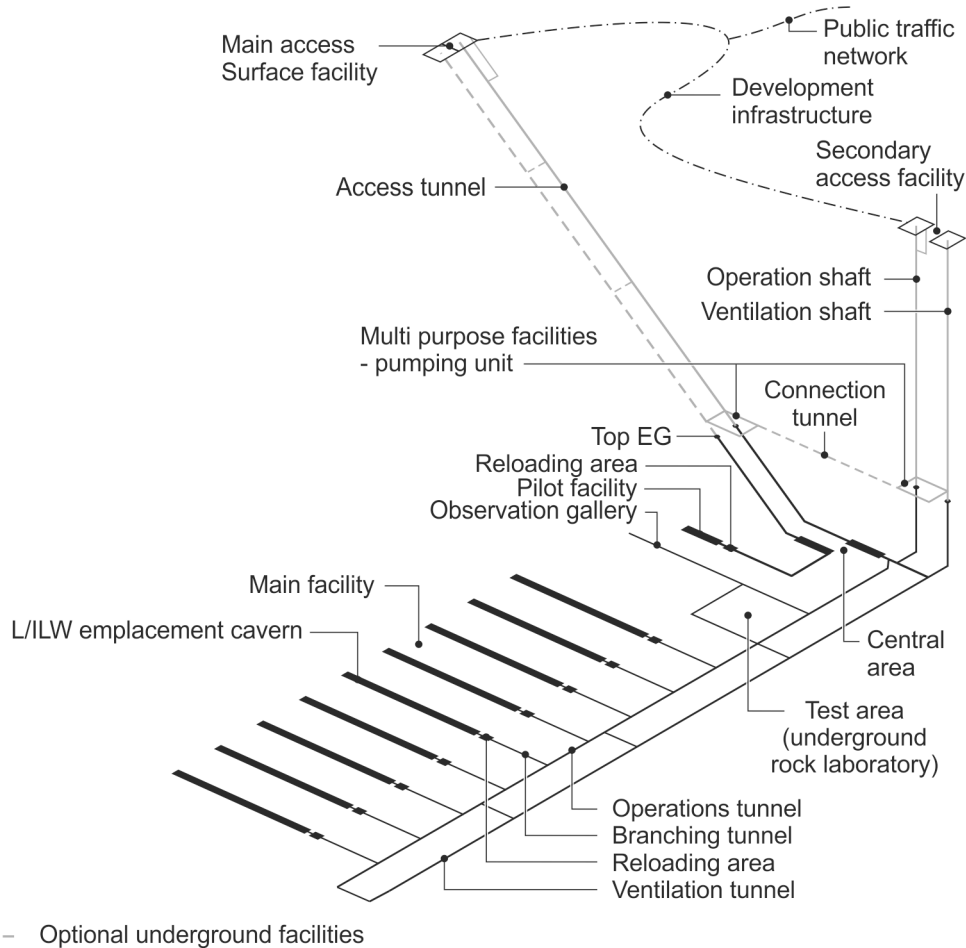


Fig. 1-1: Example layout for the L/ILW repository.

The main elements of the repository layout include:

- surface facilities (entrance facility, head of shaft)
- access ramp and a shaft as well as a central area and operation tunnel at repository level
- pilot facility and test area with dedicated tunnels and a pilot cavern
- an array of L/ILW emplacement caverns, each approximately 200 m in length and with a cross-section of approximately 10×13 m, spaced 100 m apart, in which disposal containers are emplaced

The void spaces within the emplacement rooms are backfilled with cementitious mortar. After backfilling of a room is complete, it is closed with a concrete plug.

Each emplacement room is linked to the operation tunnel by a branch tunnel. The branch tunnel is enlarged at the beginning of the cavern in order to facilitate reloading operations. The back-filling of this and other access routes constitutes the EGTS, which is described further in Chapter 2.

1.3 Mineralogical evolution and the issue of clogging

The barrier systems provided by the L/ILW repository consist of materials that, in some cases, have contrasting geochemical properties, e.g. concretes and materials containing clay minerals, such as the sand/bentonite mixture proposed for the EGTS (see Chapter 2). If these materials are in contact, long term mineralogical changes and corresponding changes in porosity and other relevant properties can occur (Berner et al. 2013; Gaucher and Blanc 2006; Kosakowski & Berner 2013; Savage 2009; Savage et al. 2010). In the case of the EGTS, depending on the choice of layout and materials, mineralogical changes could occur such that the pore spaces become clogged. Several modelling studies (e.g. Bildstein et al. 2007; Kosakowski & Berner 2013; Kosakowski et al. 2009; Marty et al. 2009; Trotignon et al. 2005, 2006, 2007; De Windt 2004) predict a long term porosity clogging at clay/cement interfaces under fully water saturated conditions. Furthermore, there is some evidence from experiments and analogues for porosity clogging at direct clay/cement interfaces. Fig. 1-2, from Gaboreau et al. (2012), shows one of the few experiments that indicate fast porosity clogging at clay/cement interfaces. The experiment relates to a 5 year old contact between shotcrete and claystone. An important result is that the evolution of porosity was not homogeneous along the interface. Porosity was reduced or enlarged, depending on the (local) hydrochemical situation of the materials and the liquid saturation. As the chemical reactions leading to clogging are fast, the spatial scale of porosity reduction is around 0.1 mm (which is much smaller than the minimum discretisation of the models described in this report). Further evidence on the centimetre scale comes from studies of the Maqarin natural analogue (Shao et al. 2013; Smellie 1998; Steefel & Lichtner 1998).

Savage (2009) reviewed experimental evidence for the development and properties of cement-bentonite interfaces with implications for gas transport. In his conclusions, he states that geochemical/mineralogical effects are most pronounced at longer timescales, with advective flow and with cement porewater with $\text{pH} > 13$. He did not find indications for geochemical/mineralogical perturbations for partially-saturated systems. For fully saturated, advective systems with very high pH, porosity increase and increase in gas permeability seem most likely. For diffusive transport at fully saturated interfaces with $\text{pH} < 13$, he gives porosity decrease as most likely development.

Generally, porosity clogging at an interface needs two related conditions to occur:

1. reactive mineral phases on either side of the interface that provide dissolved species necessary for precipitation to occur, and
2. transport, normally diffusion, of the dissolved species towards the interface.

A key chemical interaction in these types of systems is that between Si from dissolution of clay minerals (e.g. montmorillonite), or the quartz gravel, or quartz sand usually used in a sand/bentonite mixture, and the minerals in concrete, as illustrated in Fig. 1-3. High pH solution diffusing from the cement across the clay/cement interface will enhance dissolution of SiO_2 in the clay near the interface. The dissolved Si will diffuse towards the concrete and react with dissolved Ca from cement minerals (portlandite and Ca-rich C-S-H) to form new C-S-H phases, which will precipitate. If C-S-H precipitation is localised near the interface, porosity clogging may occur. Note that the dissolution of portlandite is a rather fast process and will be controlled

by the concentration of Ca in the porewater. The formation of this C-S-H phases is understood to be a rapid process and depends only on the availability of dissolved Si and Ca, as well as water. Under saturated conditions, the availability of water is not a limiting factor.

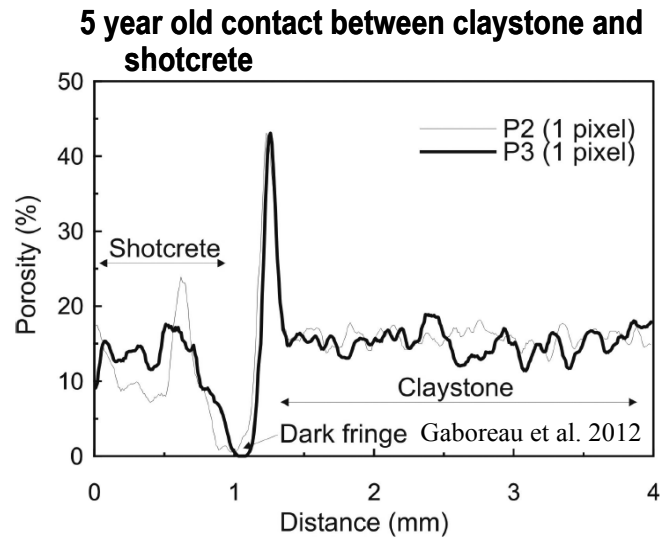


Fig. 1-2: Porosity profile across a 5 year old interface between claystone and shotcrete (from Gaboreau et al. 2012).

Fig. 1-3: Concept of a clogging interface between reactive quartz sand (or a sand/bentonite mixture) (left) and concrete (right) in a diffusive transport regime.

The transformations described above are similar to the so called alkali-silica reaction (ASR) causing expansion, cracking and degradation of concrete (Hou et al. 2004; Multon et al. 2009a; Winter 2009). ASR is caused by the reaction of hydroxyl ions in the porewater with reactive forms of silica aggregate. The long term effects of ASR on cementitious materials in an L/ILW repository are discussed in Kosakowski et al. (2014).

1.4 Methodology to evaluate long-term evolution of the Engineered Gas Transport System

The approach adopted in the present report is to choose an example EGTS design as the basis for the analysis for which there are good qualitative arguments to believe it will perform as intended over the required time frame, and especially that no clogging due to precipitation will occur. Illustrative calculations of the evolution of mineralogy and porosity are then performed for the example design to complement these arguments using state-of-the-art coupled reactive transport modelling. A limited analysis of sensitivity to main design variables is also performed.

In terms of mineralogy and porewater chemistry, the calculations strive for as much realism as reasonably achievable. Thus, for example, in addition to the main minerals initially present in the various model compartments, accessory minerals present in much smaller quantities are included. Also, the (slow) dissolution of minerals often regarded as "inert", such as the quartz aggregate in concrete, is included in the calculations.

Two types of calculations are carried out: simplified 1-D calculations and more realistic 2-D calculations. The 1-D calculations are performed for fully saturated conditions, considering only diffusive transport. The 2-D calculations are performed for partially saturated conditions that include advective transport. Full water saturation ensures the availability of water, which is needed, for example, to build hydrated phases like C-S-H. In addition, it is known that diffusive transport is strongly increased under fully saturated conditions compared with partially saturated conditions (e.g. Martys 1999; Revil & Jougnot 2008), and that permeabilities also increase strongly with saturation. It is therefore expected that the assumption of fully saturated media in the 1-D calculations will induce strongest mineralogical and porosity changes. On the other hand, the 2-D calculations represent as a step towards more realistic conditions, not only by adding a second spatial dimension, but also by taking into account the partially saturated conditions that will initially be present in the emplacement rooms and EGTS and are also expected to be maintained for some time due to the low permeability of the host rock, as well as repository gas generation. It should also be noted that, should pore clogging occur, liquid flow and mass transport will stop completely in a 1-D model; it is not possible to consider redirection of flow or transport due to lateral heterogeneities (which includes porosity and saturation variations). In reality, however, the flow field will be redirected towards permeable regions.

The governing equations for flow and transport in a partially saturated porous medium (for which a fully saturated medium is a special case) are presented in Appendix A, Section A.1. The coupling to the chemical system and evaluation of porosity changes is described in Appendix A, Section A.2. The basic geochemical setup was successfully implemented and tested in (Berner et al. 2013; Kosakowski & Berner 2013; Shao et al. 2013). On this basis, the modelling approach is believed to give good quantitative information on long-term geochemical and mineralogical changes, if porosity changes are limited. For systems with strong spatio-temporal porosity decrease induced by fast mineral precipitation in small zones, it will give good information on the location of zones with porosity clogging, although prediction of exact clogging times is not possible.

1.5 Structure of this report

The remaining chapters of this report are structured as follows:

- Chapter 2 describes further the general features of the EGTS, as well as design variables that are yet to be fixed.
- Chapter 3 presents the example EGTS design, the qualitative arguments that it will perform as intended over the required time frame and illustrative 1-D and 2-D calculations to substantiate and elaborate these arguments.
- Chapter 4 presents a limited sensitivity analysis for the main design variables.
- Chapter 5 presents a discussion and conclusions.

Details of the numerical models, parameter values used, some additional calculation cases and a discussion on model accuracy and uncertainties are presented in the appendices.

2 Design of the Engineered Gas Transport System

2.1 General features

Design options for the EGTS are discussed in Section 2.6.3 of Nagra 2008c). Fig. 2-1 shows a schematic illustration of an EGTS.

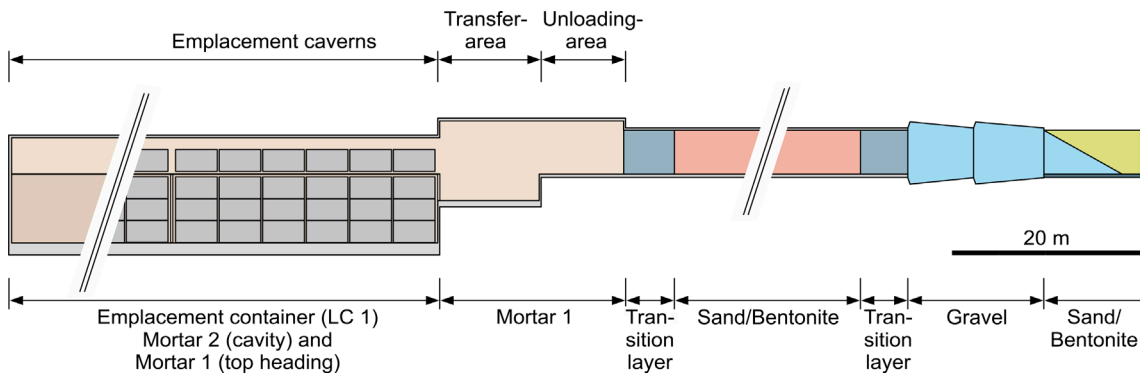


Fig. 2-1: Schematic illustration of an EGTS (modified from Nagra 2008c).

The material foreseen for access tunnel backfilling is a mixture of sand and bentonite. Sand/bentonite mixtures have significantly lower gas entry pressure than pure compacted bentonite, and the sand content allows the gas permeability to be adjusted to a desired value. However, the use of bentonite in the mixture ensures good sorption for many radionuclides, self-sealing and a low hydraulic conductivity and thus ensures the barrier functionality.

The sand/bentonite mixture has a relatively low water retention, but gas can still be trapped in irregular patterns in the inter-granular pore space of the sand/bentonite which may impair the homogenisation of the seal during the resaturation process. However, trapped gas will facilitate still easier gas migration through the sand/bentonite mixture.

Potential mineralogical changes that could lead to porosity clogging at clay/cement interfaces under saturated conditions are described in Section 1.3. For a direct contact of clay and cement, diffusion and mineral precipitation/dissolution are restricted to small volumes near the interface. These small volumes, in combination with high concentration gradients and diffusive solute fluxes, lead to the possibility of significant porosity reduction at the interface and of pore clogging, which, if continuous across the interface, could lead to a significant loss of gas permeability. For these reasons, the EGTS is constructed such that cementitious and clay materials are not in direct contact. Rather, the cementitious backfill of the emplacement rooms and the sand/bentonite backfill of the access tunnels are separated by a so-called 'transition layer' composed of sand, gravel or crushed rock. The details of the design of the transition layer are yet to be determined. Design options are discussed in the next section.

2.2 Design variables

Design options related to the transition layer essentially consist of:

- the length of the layer;
- the composition of the material used to fill the layer; and
- the coarseness of that material (i.e. its surface area to volume ratio).

The length of the transition layer mainly influences diffusive transport of solutes in the liquid phase. For a direct contact of clay and cement materials, diffusive solute fluxes driven by high concentration gradients are likely to be the major reason for any mineralogical and porosity changes. The transition layer is intended to reduce these gradients and fluxes and thus reduce the induced mineralogical changes. Concentration gradients between clay containing and cement materials in the adjoining emplacement rooms and access tunnels should become less as the length of the layer is increased.

In reality, the natural materials that are potential candidates to fill the transition layer often contain potentially reactive mineral phases. The positive effect of the transition layer on the interface mineralogical stability may potentially be overridden if the materials of the transition layer are in thermodynamic disequilibrium with the adjacent materials. Two materials for the transition layer are considered in this report: (i), calcite, which is present in the host rock, in the cement in concrete and in the sand/bentonite and is expected to be in thermodynamic equilibrium with them, and (ii), quartz, which is present in the sand of the sand/bentonite mixture, but could give rise to additional geochemical gradients at the interface between the transition layer and the concrete backfill of the emplacement rooms.

The use of a coarse material (gravel or crushed rock) with roughly uniform grain size in the transition layer has certain advantages compared with a more poorly sorted or finer material. Firstly, with a uniform coarse material, precipitates need to fill much bigger pores (volumes) in order to clog the medium, which would delay the clogging process. Secondly, as long as the transition layer is not fully water saturated, advective and diffusive transport of solutes will occur at highly reduced rates in the unsaturated, upper part of the layer compared with the fully and partially saturated (capillary fringe) lower parts. As capillary rise in very coarse granular media is low, large parts of the EGTS system are likely to be unsaturated if a coarse material is used, making complete clogging of the full cross-sectional area in the transition layer less likely. Thirdly, a coarse grain size would result in slower dissolution, which would potentially delay porosity clogging (Marty et al. 2009).

There is also flexibility in the choice of an aggregate material for the concrete. In this report, the effects of the choice of aggregate material (calcite or quartz) are also investigated as a design variable.

3 Evaluation of evolution for an example design for an Engineered Gas Transport System

3.1 Example design and its rationale

The purpose of the transition layer in the EGTS is to avoid or minimise chemical interactions, especially those of the type described in Section 1.3 that could lead to pore clogging. One option to reduce mineralogical changes in concrete and at its interface with the transition layer is to use a material that is not in chemical disequilibrium with the concrete, thus limiting the availability of solutes necessary to build precipitates locally, i.e. solutes such as Si and Ca need to be transported by diffusion before they can interact and form C-S-H (Fig. 1-3).

On this basis, an example design is considered in which limestone gravel, represented as calcite in the models, is used to fill the transition layer. As bentonite, cement and Opalinus Clay all contain small amounts of calcite, and are in thermodynamic equilibrium with it. In addition, limestone in the form of calcite is assumed as the aggregate used in the concrete backfill for the emplacement rooms. In the models, cementitious materials are represented as a generic concrete of average composition. Although each material contains calcite, geochemical gradients between concrete and other backfill materials cannot be avoided, and their impacts are analysed in the 1-D and 2-D calculations presented in the following sections. It should be noted that previous studies indicate that diffusion-dominated bentonite systems with $\text{Ca}(\text{OH})_2$ pore liquids undergo only minor amounts of ion-exchange and C-S-H precipitation (Savage 2009). On the concrete side, carbonation⁶ is to be expected. In a fully liquid saturated system carbonation is caused by the in-flux of inorganic carbon from neighbouring regions. Transport of inorganic carbon could also cause a re-distribution of calcite, which has a low solubility under high pH conditions, whereas solubility is higher at neutral pH. This issue is addressed in the calculations in the following sections of this chapter for transport in liquid phase (the effects of transport of CO_2 in gas phase are discussed in qualitative terms in Appendix D.4).

The sensitivity of EGTS evolution to other choices of material such as quartz gravel is addressed in Chapter 4. The thickness of the transition layer is set to 10 metre. This is a reasonable, but somewhat arbitrary choice. Again, sensitivity of EGTS evolution to transition layer thickness is addressed in Chapter 4.

3.2 Illustrative 1-D calculation of evolution for a saturated system

3.2.1 Model domain and main model assumptions

The following illustrative 1-D calculation addresses the long-term evolution of mineralogy and porosity at main interfaces of the calcite filled transition layer, with a focus on the interfaces where the greatest changes are likely to occur: i.e. the interfaces with the sand/bentonite tunnel backfill and with the concrete. 1-D diffusive transport is modelled along the axial direction of the EGTS (tunnel) in fully saturated media (saturation of unity throughout the model domain), where solute transport in this direction is the main driving force for mineralogical transformations. Similar calculations on the pH buffering capacity in crushed granite backfills were carried out by Benbow et al. (2002, 2004) for the Swedish repository design.

⁶ Carbonation is the reaction of dissolved inorganic carbon with calcium hydroxide and C-S-H to form additional calcite. At pH values between 7 and 9 inorganic carbon is present in the porewaters of the sand/bentonite and the transition layer as bicarbonate (HCO_3^-), whereas under highly alkaline conditions in the cement porewaters the carbonate (CO_3^{2-}) is the predominant form.

The same pore diffusion coefficient of 1.5×10^{-9} m/s is assumed for all migrating species (Berner et al. 2013; Kosakowski & Berner 2013). The effective diffusion coefficient is calculated according to Eq. A-7 of Appendix A.1, using an exponent $b = 2$. Only diffusive transport is considered in this and other 1-D calculations, so that the definition of permeabilities or other hydraulic parameters/boundary conditions is unnecessary. The thermodynamic setup of the system, the initial compositions and porosities of the materials and the resulting initial porewater compositions are described in Appendix A, Section A.3.

The conceptual setup for the 1-D calculation is shown in Fig. 3-1. The transition layer material is mainly calcite, but also contains in addition minor amounts of other minerals (Appendix A, Tab. A-1). This 10 m thick layer ('calcite gravel' in the figure) is sandwiched between a concrete compartment and a sand/bentonite compartment, of lengths 20 m and 30 m, respectively. The lengths of these compartments ensure that the boundaries do not influence the evolution at their interfaces with the transition layer. Constant concentration boundary conditions for the corresponding material porewaters are applied at the extreme left- and right-hand boundaries in Fig. 3-1.

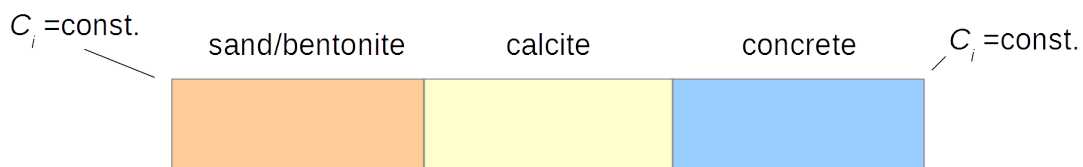


Fig. 3-1: Main features and geometry for 1-D modelling.

Two variants of the model are investigated, differing in the discretisation of the model domain. In the variant with finer numerical mesh, the 1 m wide regions around each of the material interfaces are discretised using a mesh with 1 cm node separation. Node separation increases further away from the material boundaries. The 1 cm discretisation is identical to previous simulations of concrete/host rock interfaces (Kosakowski & Berner 2013), which allows a comparison of time scales for porosity changes between the present results and those of this earlier modelling. The second variant uses a coarse mesh with equidistant node distances of 10 cm. The coarse mesh allows reaching simulation times up to 100 000 years with reasonable time necessary for computing. The results presented in this section are for the second, coarsely discretised variant. A detailed comparison of the results for both variants and an evaluation of the influence of mesh size on model results are given in Appendix D, where it is noted that the effects of discretisation for this particular model set up are minor.

The model uses kinetic control for all minerals that are known to have slow reaction kinetics. The implementation of kinetic control is described in Appendix A, Section A.4. Calcite precipitation/dissolution is not kinetically controlled, as calcite kinetics is fast. The implemented kinetic law for the dissolution of quartz⁷ uses the specific reactive surface area as parameter to describe the coarseness of different materials. For example, a coarse gravel is considered to have the same rate constant as a sand, but a significant lower reactive surface area which would potentially delay porosity clogging (Marty et al. 2009). The influence of kinetic control of other mineral phases is investigated in Appendix D.2.

⁷ Quartz represents all forms of SiO₂. It is a major constituent of sand/bentonite and an accessory mineral in the transition layer.

The model assumes fully liquid saturated conditions and diffusive transport only. As noted in Section 1.4, this is a limiting case that maximises diffusive transport, the driving force for most mineral reactions, as effective diffusion coefficients decrease strongly in partially saturated media compared with saturated media (Martys 1999; Revil & Jougnot 2008; Savoye et al. 2010). The effect of saturation and additional advective transport due to influx of groundwater from the host rock is addressed in the 2-D calculation case presented in Section 3.3.

3.2.2 Model implementation

The general purpose FE code OpenGeoSys (Kolditz et al. 2012a) is used to solve the flow and transport equations. Verification and application examples for single and coupled thermal-hydraulic-mechanical-chemical (THMC) processes can be found in Kolditz et al. (2012b). The OpenGeoSys code has been parallelised with the Message Passing Interface (MPI) (Wang et al. 2009) and an overlapping domain decomposition method has been implemented with the help of the PETSc library (Wang et al. 2013).

The numerical kernel GEMS3K of the chemical solver GEM-Selektor V. 3 (Kulik et al. 2013) was used for the chemical calculations. The general coupling between the two codes for fully liquid saturated media is described in (Shao et al. 2009) and summarised in Appendix A, Section A.2.

3.2.3 Calculation results

Fig. 3-2 shows calculated mineralogical profiles across the EGTS transition layer and the adjoining regions for selected times up to 100 000 years. The evolution of porosity and pH with time is shown in Fig. 3-3 and 3-4, respectively. The results show only minor porosity reduction (as well as some porosity increase) at material interfaces. There are no indications of porosity changes that could result in pore clogging (see discussion in Section 3.2.4). Only relatively small amounts of C-S-H precipitation occur, and the precipitates are distributed fairly broadly throughout the transition layer. The pH in the concrete remains high for long times and a zone of increased pH stretches across the transition layer into the sand/bentonite after 100 000 years. This effectively suppresses re-distribution of calcite in the system and carbonation of concrete (see discussion in Section 3.2.4).

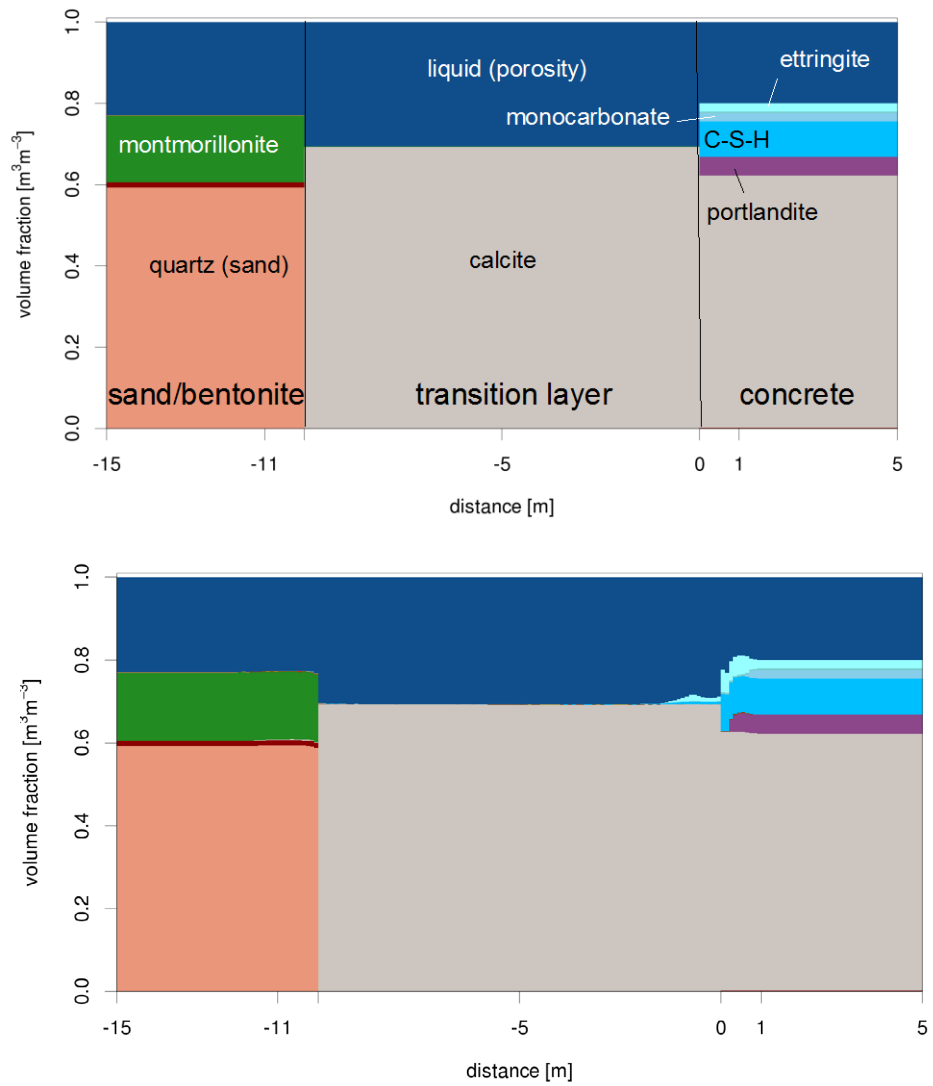


Fig. 3-2: Mineralogical profiles at different times across a 10 m long transition layer composed of calcite and the adjoining regions after 0, 10 000, 20 000 and 100 000 years.

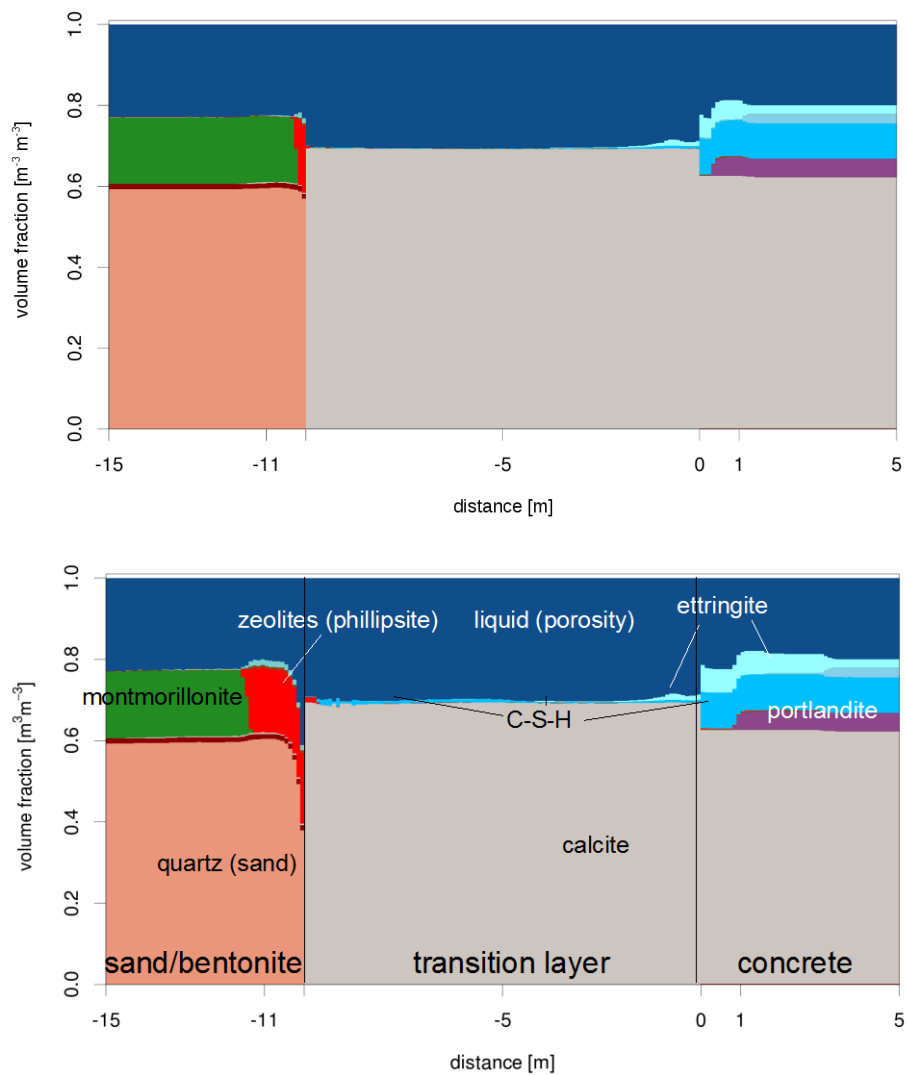


Fig. 3-2: (continued).

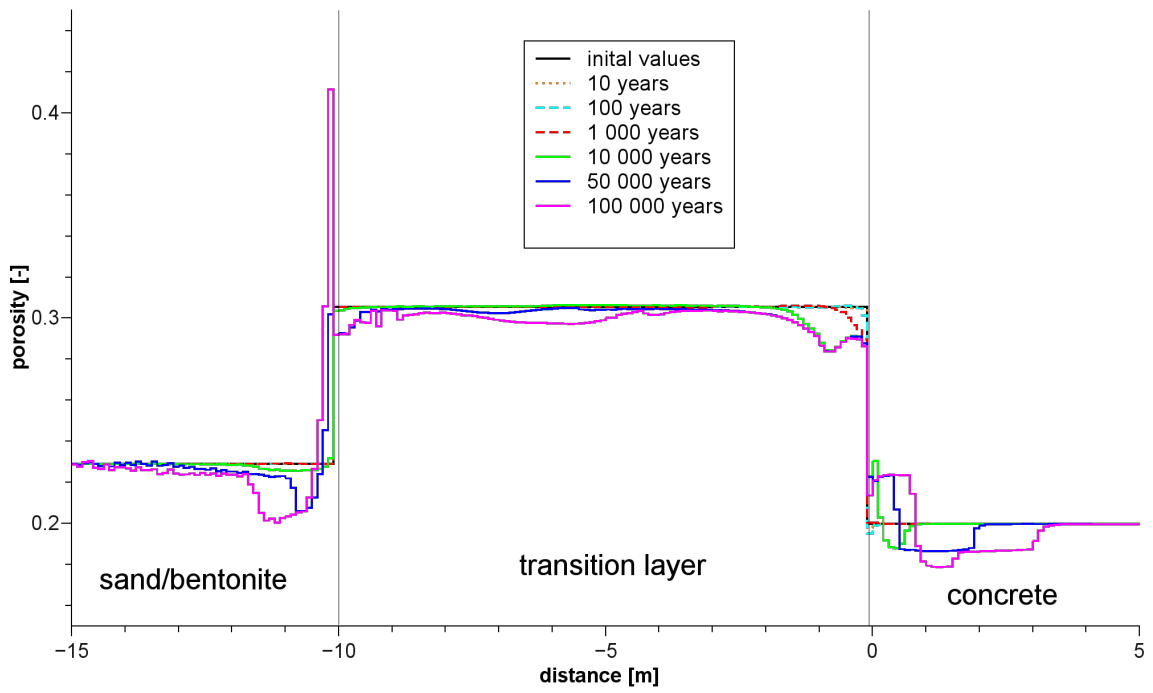


Fig. 3-3: Evolution of porosity within a 10 m long transition layer composed of calcite and the adjoining regions.

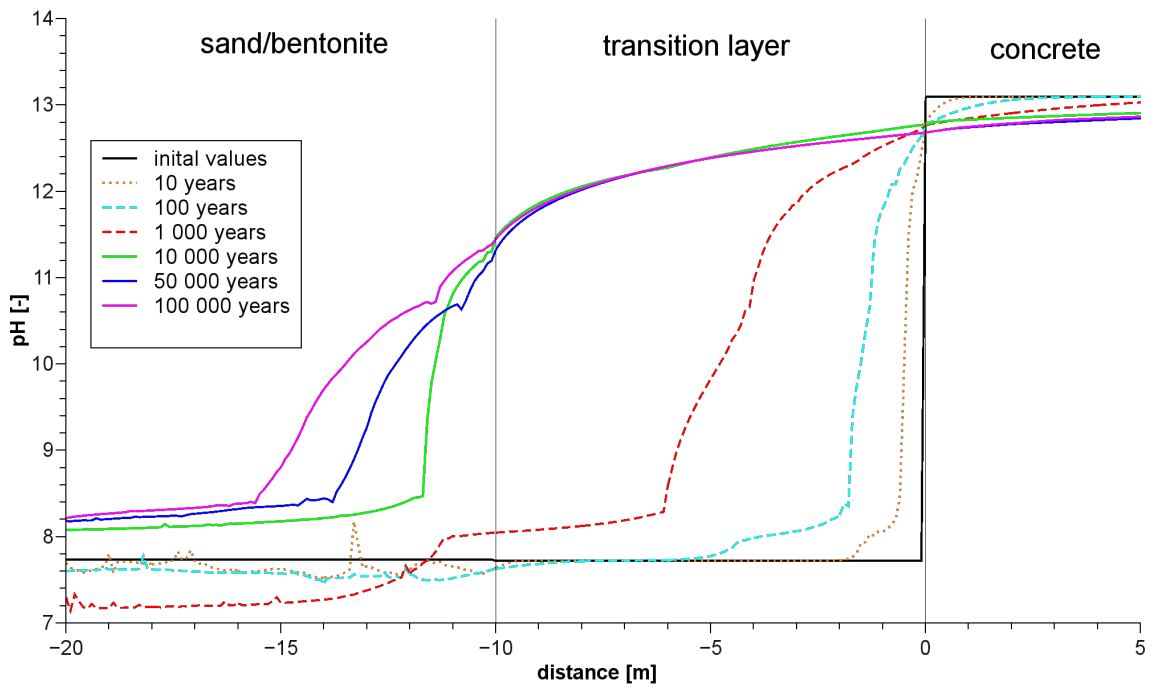


Fig. 3-4: Evolution of pH within a 10 m long transition layer composed of calcite and the adjoining regions.

3.2.4 Interpretation of results

In this example design, the evolution of the EGTS is governed primarily by mineral dissolution and by the diffusion of solutes across the interfaces. Fig. 3-5 summarizes the main processes in a sketch for a system with a 10 m long transition layer. The transition layer provides a layer where solutes from sand/bentonite and from the concrete mix (see below).

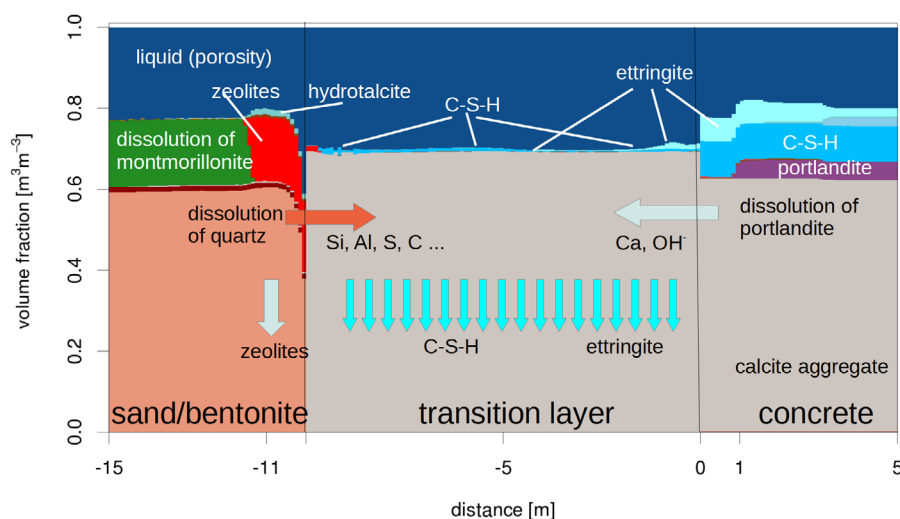


Fig. 3-5: Schematic illustration of major processes in an EGTS where concrete and sand/bentonite compartments are separated by a 10 m layer of calcite gravel after 100 000 years.

The evolution of the mineralogy across the transition layer shown in Fig. 3-5 shows the migration of several reaction fronts caused by solutes migrating from one zone into another. The fronts move with decreasing speed, as expected where diffusion is the rate-controlling process. Progress x with time t follows the relation $x \sim (Dt)^{1/2}$, where D is an apparent mineral-phase-specific diffusion coefficient (see also Section 4.1).

The figure shows that, in the concrete, monocarbonate progressively dissolves and some further ettringite and small amounts of calcite are formed. This is triggered by the in-diffusion of SO_4^{2-} from the transition and sand/bentonite layers saturated with host-rock porewater. Portlandite is also progressively dissolved, but its dissolution front moves slower than the monocarbonate dissolution front. This results in a small decrease in porosity between the dissolving monocarbonate front and the dissolving portlandite front (Fig. 3-3). This is, however, a transient feature that migrates that does not build up over time (no risk of clogging). The progress of these dissolution fronts has been extrapolated in Kosakowski et al. (2014) and is shown to be typically a few meters in 100 000 years for a direct contact between clay and cement materials if, as is the case here, porosity clogging does not occur. In the present calculations, progress of dissolution fronts is less, as large scale concentration gradients between clay and cement materials are reduced by the transition layer.

In the transition layer, the accessory minerals montmorillonite and quartz are quickly dissolved. They provide Si which reacts with Ca from portlandite in the concrete to form C-S-H between the dissolution fronts in the transition layer and the portlandite dissolution front in the concrete. Montmorillonite and quartz are present in the transition layer in much lower quantities than portlandite in concrete. Dissolution fronts in the transition layer thus move much faster than in concrete, which induces also a rapid displacement of the location where C-S-H precipitation occurs. Thus, C-S-H precipitation is not highly localised, but distributed across the whole transition layer, reducing its impact on porosity.

Some ettringite precipitation is also observed in the transition layer, near to the interface with the concrete, which occurs during early stages due to the sulphate inventory in the initial pore-water present in the layer. At later stages, further minor ettringite precipitation is also observed elsewhere within the transition layer.

In the sand/bentonite, montmorillonite and silica in the quartz sand are progressively dissolved due to the influence of the high-pH conditions diffusing through the transition layer and replaced by phillipsite (a mineral of the zeolite group), with, in addition, minor amounts of hydromagnetite and hydrotalcite⁸. The montmorillonite contains structurally and in the inter-layer some amount of Fe which, is taken up to form hydromagnetite (which is also initially present in the bentonite). Excess Al and Mg cause the formation of hydrotalcite. The thermodynamic model setup does currently not contain any magnesium silicate hydrates (M-S-H phases). There are experimental indications that, in reality, M-S-H phases might be built instead of hydrotalcite (Lothenbach, personal communication). Note also that the model variant does not include the additional pH buffering capacity provided by surface complexation in the sand/bentonite, as described in Berner et al. (2013). This is currently a limit of the numerical model, as it is not yet possible to kinetically control mineral phases with associated surface complexation.

For this specific layout (10 m long transition layer which is assumed to contain small amounts of clay minerals), the precipitation is spread over the complete layer, because the dissolution of accessory clay minerals in the transition layer frees silica which is locally consumed for the formation of small amounts of C-S-H. In addition, the silica released from the dissolution of the quartz sand, clay and zeolite minerals from the sand/bentonite diffuses into the transition layer and mixes with calcium diffusing out of the concrete. This triggers the non-localised precipitation of C-S-H phases near (but not at) the interface with sand/bentonite.

Fig. 3-3 shows limited changes of porosity related to the occurrence of reaction fronts. Typically in such fronts, a mineral is dissolved and replaced by another mineral with different molar volume. In the modelled system, such volume changes only cause relatively small porosity changes.

Fig 3-4 shows that a high pH is maintained throughout the concrete because the system does not contain any mineral phases that can take up hydroxide ions. In order to reach the portlandite buffered pH of about 12.5, the hydroxyl ion concentration in the concrete porewater would have to be lowered significantly by out-diffusion towards the transition layer. The pH increase in the sand/bentonite, although sufficient to promote some montmorillonite and silica dissolution, remains moderate, since the pH is buffered by the dissolution and transformation of clay and zeolite minerals.

⁸ The effect of high pH concrete porewater on sand/bentonite mixture was investigated using calculations assuming equilibrium chemistry (Kosakowski 2010). It was found that montmorillonite is dissolved and replaced by zeolites, hydrotalcite and C-S-H. Porosity changes were found to be small (Table 15 in Kosakowski et al. 2014).

In concrete, the amount of dissolved Ca in solution is governed by equilibrium with portlandite or, in absence of portlandite, with C-S-H. In principle, calcite is thermodynamically more stable than portlandite or C-S-H. Transformation of portlandite and C-S-H into calcite is hindered only by the availability of dissolved inorganic carbon. The ingress of inorganic carbon, as gas (CO_2 , which is then dissolved locally) or in dissolved form as bicarbonate, would cause carbonation of concrete, dissolution of portlandite (and later C-S-H) and associated reduction in pH (Glasser et al. 2008; Winter 2009).

Calcite gravel in water at neutral pH shows a concentration of Ca similar to that of concrete (see Appendix A, Tab. A-2), but the amount of dissolved inorganic carbon (in form of bicarbonate HCO_3^-) is higher. The transport of HCO_3^- from gravel compartment towards the adjacent concrete could cause dissolution of calcite gravel and carbonation of concrete. This process is overridden by diffusion of OH^- from concrete towards the gravel which causes an increase of pH. The molar solubility of calcite is decreasing strongly with increasing pH and increases again above pH 11 as shown in Fig. 3-6 for simplified water chemistry. Increase of pH above 11 in the gravel compartment therefore prevents the redistribution of calcite.

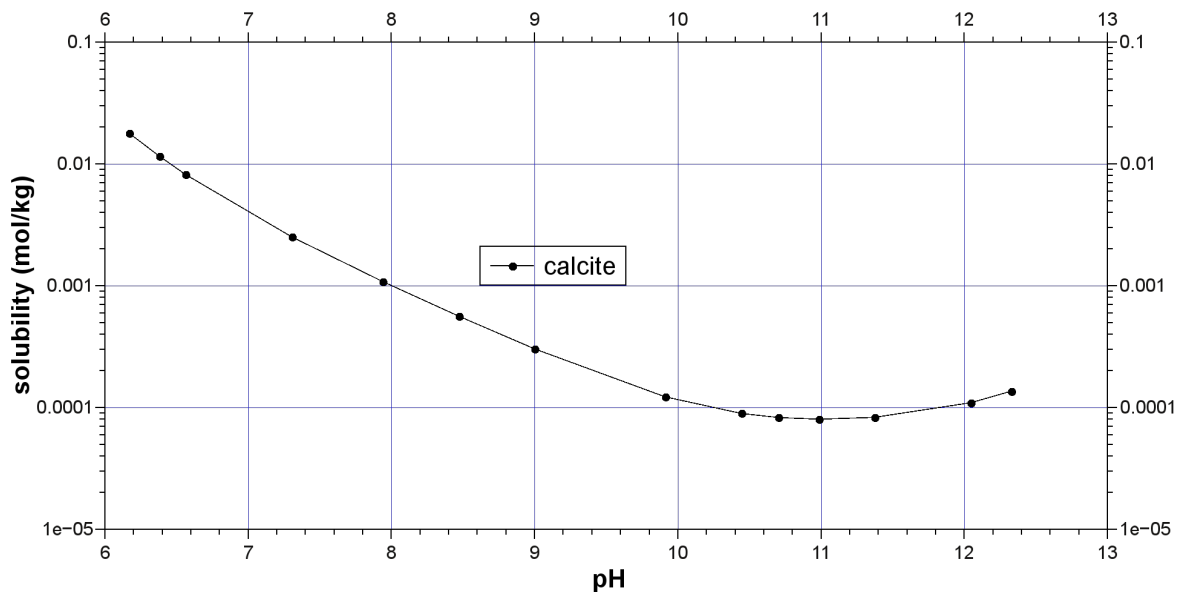


Fig. 3-6: pH dependence of calcite solubility calculated for a simple NaCl water (0.001 g NaCl per 1 kg water) with GEMS-PSI for data from PSI/Nagra TDB.

pH was varied by addition of small amounts of NaOH or HCl.

3.3 Impact of initial partial saturation: illustrative 2-D calculation

The analyses presented in the previous section assumed that the analysed system is fully saturated at all times. In reality, because of the low permeability of the host rock, as well as repository gas generation, the emplacement rooms will saturate relatively slowly and water will accumulate preferentially in the bottom part of the mortar backfill of the emplacement rooms. At the same time, as repository-generated gas is produced, it will mix with any remaining trapped gas and accumulate at the top of the rooms in the high-permeability mortar.

Similarly, in the transition layer of the EGTS, any gas/liquid mixtures that enter this zone will be separated due to the large pore sizes. Liquid will accumulate at the bottom, with a low residual liquid content in the gas saturated upper part of the layer. The low residual water

content in the upper part of the layer will minimise transport in the liquid phase and reduce mineralogical changes and the consequent possibility of pore clogging. Mineralogical changes in the lower part of the layer are expected to proceed in a similar manner to the fully saturated case described in the previous section. Overall, complete clogging of the EGTS across its full cross-sectional area is even less likely than implied by the analysis of the fully saturated, 1-D Case.

Some illustrative 2-D model calculations have been performed to illustrate the behaviour described above. These calculations improve those using the 1-D model by adding a second spatial dimension, by considering the water saturation of the materials and also by adopting an improved thermodynamic setup as described in Shao et al. (2013). However, especially for highly refined mesh sizes, they need more computational resources than the 1-D calculations and it is currently not possible to reach very long simulation times or to carry out an extensive sensitivity analyses of material and transport parameters without the use of relatively coarse meshes (see Section 3.3.2). Nevertheless, they can still give valuable insight in additional process couplings and the influence of spatial heterogeneities.

3.3.1 Model domain and additional model assumptions

Fig. 3-7 shows the basic geometry of the 2-D model. The main elements of the EGTS – the concrete backfill of an emplacement room, the transition layer (calcite gravel) and the sand/bentonite filled access tunnels – are each represented by 10 m long and 5 m high model regions. A model height of 5 m was chosen, which is close to the model dimension used in Senger & Ewing (2009) for the seal and branch tunnels of the local scale model (4.82 m in Figure 2-7 of Senger & Ewing, 2009). The length of the transition layer is the same as the length used in the 1-D model (Section 3.2). The length of the sand/bentonite and the concrete compartments are chosen such that eventual reaction fronts can be observed up to 100 000 years. Note that model height is not a sensitive parameter in this model, as long as fully saturated conditions exist only at the tunnel bottom and as long as the extension of capillary fringe (zone with varying saturation above the water table) is much smaller than the height of the model. These conditions are satisfied in the present calculations; from the model results in Section 3.3.4, it is clear that all major mineralogical and porosity changes are restricted to a zone which is less than half of the model height.

No-flow conditions for liquid and solute transport are imposed at the upper and lower model boundaries. This is motivated by the assumption that the host rock (including EDZ) and materials for tunnel support have much lower permeabilities than tunnel backfill and transition layer materials (see Senger & Ewing 2009), as well as the possibility of pore clogging at the boundary with the host rock (see also the discussion in Section 3.2.1). The permeability and diffusivity contrast between the host rock and the engineered materials in the repository lowers effectively water and solute transport across the host rock – tunnel support – tunnel backfill interface and channels transport in the tunnel.

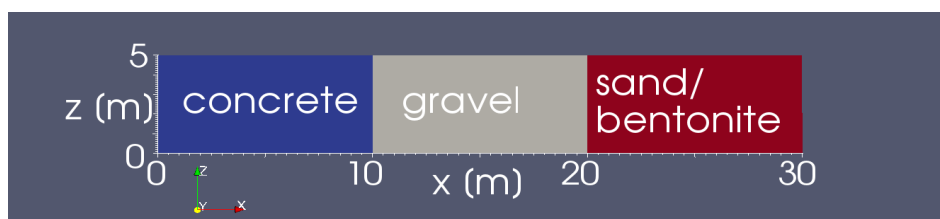


Fig. 3-7: Main features and geometry for 2-D modelling.

The governing equations for flow and transport in a partially saturated porous medium are presented in Appendix A, Section A.1. The model starts with the initial capillary pressure and saturation distribution shown in Fig. 3-8. The capillary pressure is set such that initial saturation at the bottom of the domain is 1, i.e. $P_c(z = 0) = 0$ and $S = 1$. P_c decreases with height $P_c(z) = -z \cdot g \cdot \rho$ which corresponds to the pressure drop in a water column of density $\rho = 1 \times 10^3 \text{ kg/m}^3$ for the gravitational acceleration g of 9.81 m/s^2 . The resulting initial saturation depends on the material dependent capillary-pressure relation with parameters as given in Tab. A-4. In the bottom part of Fig. 3-8, the much lower residual saturation in the middle transition layer compartment compared with the adjoining compartments is clearly seen.

On the left side of the model domain (Fig. 3-7), the capillary pressure distribution is assumed to remain constant over time. On the right side, constant groundwater inflow is assumed to occur from the access tunnel system, with a value based on two-phase flow calculations by Senger & Ewing (2009).

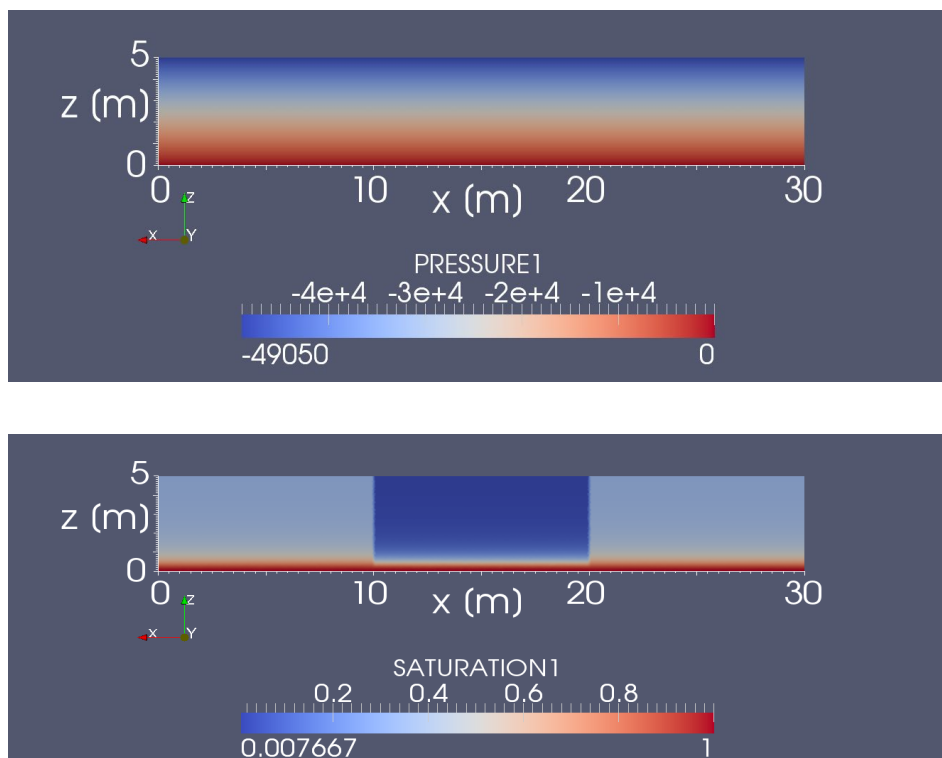


Fig. 3-8: Initial capillary pressure distribution in Pa (upper figure) and saturation distribution (lower figure) for 2-D modelling.

It should be noted that there are significant differences between the assumptions made regarding the transition layer in the present study and in the model used by Senger & Ewing (2009). Firstly, Senger and Ewing treat the transition layer as being filled with low-permeability material, whereas, in the present study, the transition layer is filled with a highly permeable medium. Secondly, unlike in the present study, Senger and Ewing include the EDZ as a transport pathway. From the repository room model of Senger and Ewing it is known that the flow through the EDZ exceeds the flow through the tunnel by orders of magnitude (Figure 4-22 in Senger & Ewing 2009). The consequences of these different assumptions on the overall flow rates through (and around) the transition layer are currently unknown. For the purposes of this

study, however, it is assumed that the flow rate through the currently assumed high-permeability transition layer is similar to that through Senger and Ewing’s low-permeability transition layer and much higher permeability EDZ.

One should also note that the flow calculations presented in this report are based on the Richards' Equation (Appendix A, Equation A-1), which is **not** back-coupled to a similar equation for gas flow. This implementation assumes a constant gas pressure at all locations and at all times throughout the domain. Therefore, the model does not reproduce the two-phase flow model used in Senger & Ewing (2009), which includes explicitly gas flow induced by time varying source terms for gas production. Nevertheless, the modelling approaches used in this report and by Senger & Ewing (2009) are identical in their description of liquid flow in partially saturated media at constant gas pressure (see also the discussion of transport of gaseous species in Appendix D.4).

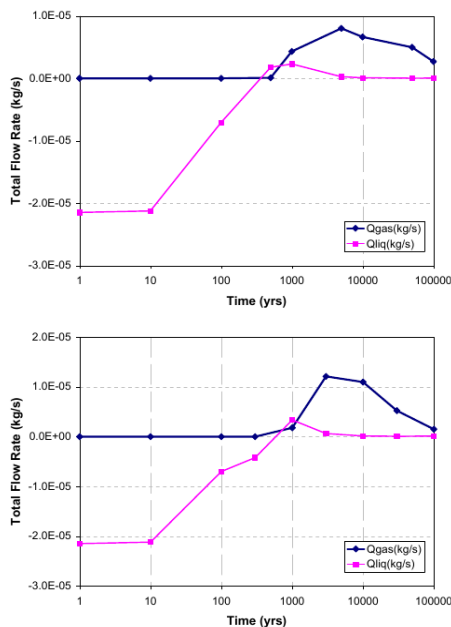


Figure 4-7: L/ILW-Model: Total flow (gas and liquid) through the repository seal (V4) (including EDZ) to the updip access ramp for Simulation Cases R_CM02 (from Senger & Ewing 2009a / revised case)

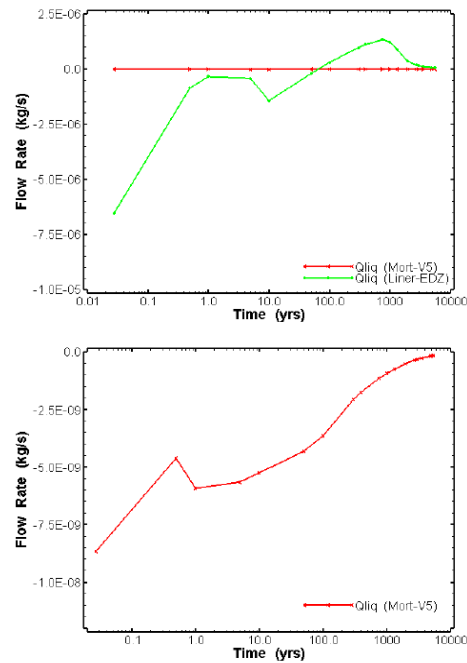


Figure 4-17: Repository Cavern Model: Computed water flow through the V5 cavern seal (Mort-V5) and into the surrounding host rock (Liner - EDZ) through time (top), and detailed resolution for water flow through V5 (bottom).

Fig. 3-9: Figure 4-7 (left) and 4-17 (right) from Senger & Ewing (2009).

The negative values indicate flow from the repository access tunnel system (ramp) into the emplacement room.

The model of Senger & Ewing (2009) assumes that initial gas saturation in an emplacement room is high and that concrete materials, the transition layer and the sand/bentonite backfill of the tunnel branch are close to the residual water saturation (see Figure 4-19 of Senger & Ewing, 2009). Senger and Ewing investigate gas and liquid flow with models of different scale. In their large scale 3-D model of the L/ILW repository the repository starts to de-saturate by inflow of water from the ramp through the repository seal (including EDZ). Water from the host rock formation migrates into the sand/bentonite backfill of the access tunnels and from there migrates into the emplacement rooms. From the results reproduced in Fig. 3-9, it can be deduced that maximum total mass flow rate to the emplacement caverns occurs at early times and are below

about 2×10^{-5} kg/s ($0.6 \text{ m}^3/\text{year}$)⁹. They also calculated models for one repository cavern only, which allow differentiating between water flow through cavern seals and through liner and EDZ. These models indicate that the flow through a cavern seal towards the cavern is very low (less than 10^{-8} kg/s, or 0.3 litres/year). After more than 1000 years, the flow direction is reversed due to increasing pressure of repository-generated gas and the room becomes completely desaturated again.

For the present 2-D modelling, since the initial porewater outflow from an emplacement room is negligible, simulations start with water flowing into the room. Inflow is set to a constant Darcy flux of $5 \times 10^{-11} \text{ m s}^{-1}$, corresponding to a total liquid mass flux of about $10^{-6} \text{ kg/s}^{-1}$ ($0.03 \text{ m}^3/\text{yr}$) in a tunnel with a cross-section area of 20.5 m^2 (branch tunnel according to Table 2-1 in Nagra 2008c). The selected constant Darcy flux is rather arbitrary, but not unrealistic. It corresponds to a kind of averaged flow (including flow through EDZ) for the repository seal model of Senger & Ewing (2009). The flow rate is high enough such that the transport regime is not dominated completely by diffusion and that the effects of advective transport of solutes are visible. The use of much lower values in accordance with the repository cavern model would lead only to very small effects (mineralogical transformations, porosity changes) even after 100 000 years simulation time. Reaction fronts driven by diffusive exchange across the material interfaces would dominate. The consequences of diffusive transport are already investigated by the fully saturated 1-D calculations.

Permeabilities for liquid flow within the model domain depend on the saturation state of the medium and on porosity, which may change in time due to mineral precipitation and dissolution; see Appendix A for details.

Model assumptions regarding geochemical evolution are generally identical to those of the 1-D model. The only difference is that, in this 2-D model, a slightly more refined chemical setup was used that considers more zeolite minerals (see Section 3.3.2).

3.3.2 Model implementation

The model is again implemented in the code OpenGeoSys, coupled to the numerical kernel GEMS3K if the chemical solver GEM-Selektor V. 3. For the 2-D calculations up to 100 000 years, a Finite Element (FE) mesh with 679 nodes (1224 elements) and an average node distance of about 0.5 m is used. This discretisation is about 50 times coarser than for the one-dimensional model (Appendix D.1 discusses the influence of mesh size on porosity evolution). Appendix C2 shows simulations with a refined mesh with 19 645 nodes and 38 596 triangular elements for simulations up to 1000 years. Typical distances between nodes in the refined mesh are 0.1 m. Comparison of coarse and refined 2-D model show in Appendix C, Section C.2.2 that their results on mineralogical changes are in good agreement.

The thermodynamic setup, as given in Appendix E.2, is slightly changed compared to the 1-D models. The simple illite phase is replaced by a solid solution model in order to mimic cation exchange processes. In addition more zeolite minerals were implemented, namely analcime, mordenite, laumontite. Details on the illite model and the zeolite data can be found in Shao et al. (2013). The changed illite model and the additional zeolite phases do not change the equilibrated initial mineralogical (Tab. A-1) and porewater composition (Tab. A-2), as the added minerals are not stable in these materials.

⁹ These flow rates include flow through the backfilled tunnel and the flow through the EDZ.

3.3.3 Evolution of saturation

The calculated evolution of liquid saturation is shown as a result of inflow from the access tunnel system is shown in Fig. 3-10. Because porewater enters at the right boundary over the whole height of the domain, the right boundary is fully saturated. The semi-steady state achieved after 1000 years shows that, for this flow rate, the sand/bentonite compartment will not saturate completely, i.e. porewater only saturates the lower part of the domain. The curvature of the water table is caused by the interplay of the permeability-saturation and the capillary pressure – saturation relationships. In the transition layer and in the concrete, the permeabilities are so high that water is transported rapidly along the bottom of these zones. No significant change in saturation is observed on this timescale. It should be stressed again that the model assumes a constant pressure of the gas phase during the calculation. In this model setup, changes in saturation have to be caused by significant changes in porosity due to mineral reactions, which would result in a re-direction of liquid flow.

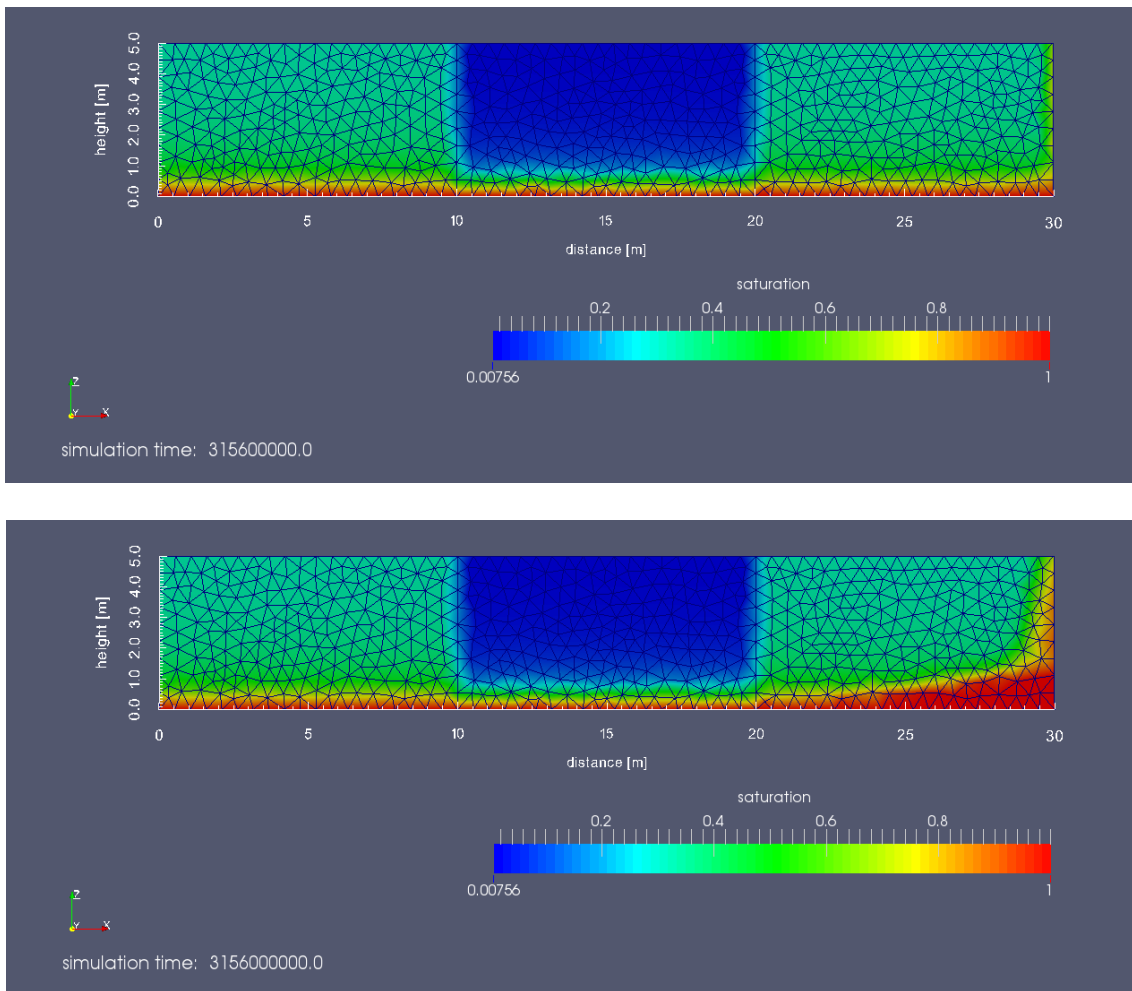


Fig. 3-10: Evolution of saturation (from top to bottom): after 10 years, after 100 years, after 1000 years and after 100 000 years.

The state after 1000 years is close to steady state, if no changes in boundary conditions or porosity occur.

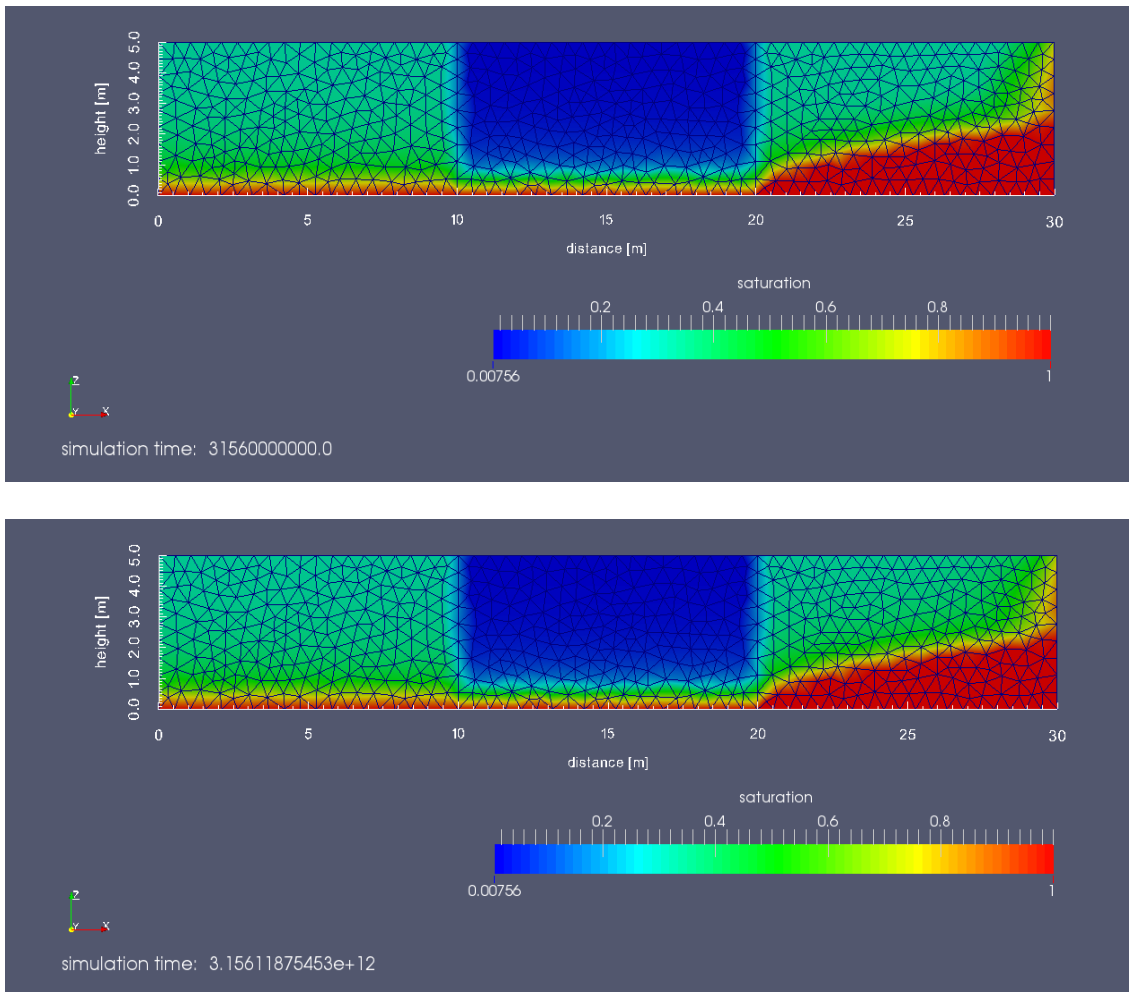


Fig. 3-10: (continued).

3.3.4 Evolution of porewater chemistry and mineralogy

Fig. 3-11 shows the calculated mineralogical profile across the EGTS transition layer and adjoining regions at 1000 years, at which time the models of Senger & Ewing (2009) predict a reversal of flow direction. Mineralogical changes are minimal at this time. At the bottom of the concrete compartment, where there is a small flow of water from transition layer into concrete, an alteration front evolves at which portlandite starts dissolving and ettringite precipitates.

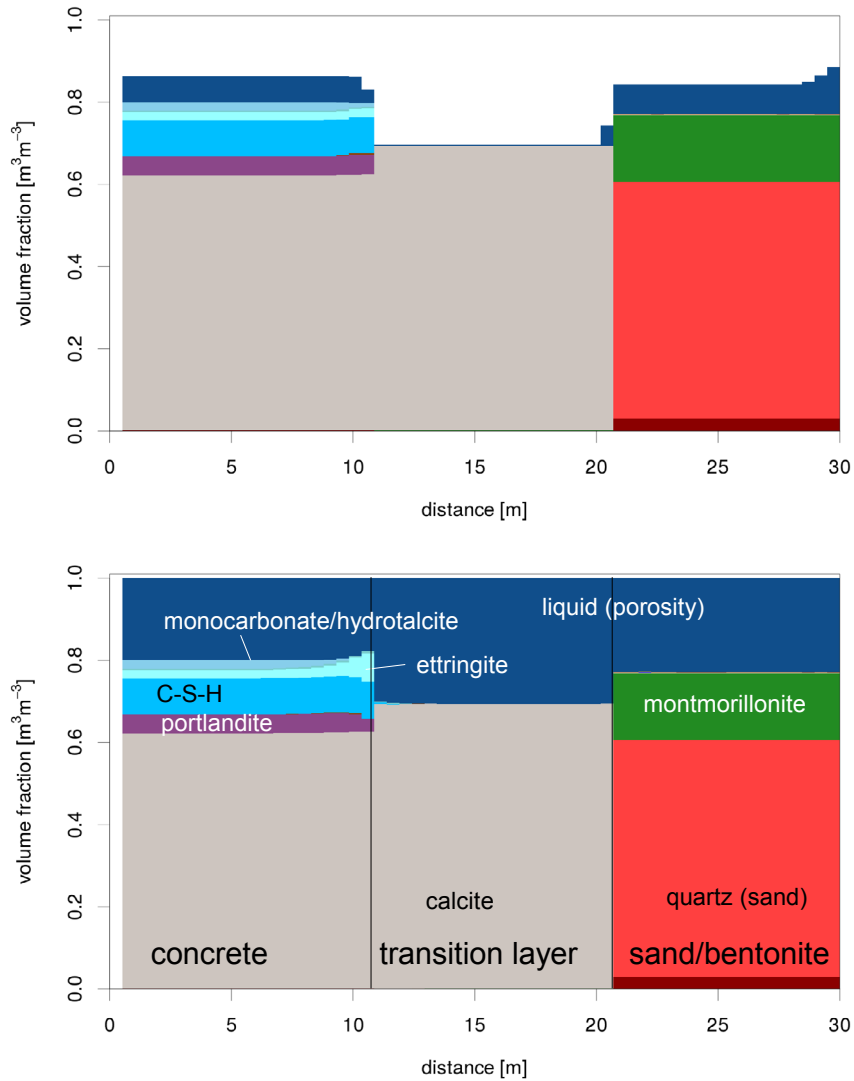


Fig. 3-11: Mineralogical profiles along the top (upper picture) and the bottom (lower picture) of the model domain at 1000 years.

Figs. 3-12 to 3-14 show the state after 100 000 years of constant flow of water into the system. The top mineralogical profile in Fig. 3-12 (upper picture) does not show any significant changes in comparison to the profile after 1000 years. At the bottom (Fig. 3-12 lower picture), under fully saturated conditions and with maximal advective transport, leaching of concrete is visible. This is caused by the ingress of host-rock porewater which has equilibrated with the sand/

bentonite. The spatial concentration distributions of total dissolved components in Fig. 3-13 can be correlated with reaction fronts of certain minerals visible in Fig. 3-14. The changes in mineralogy are also expressed in the porosity map in Fig. 3-15. Finally the evolution of the high-pH plume is shown in Fig. 3-16.

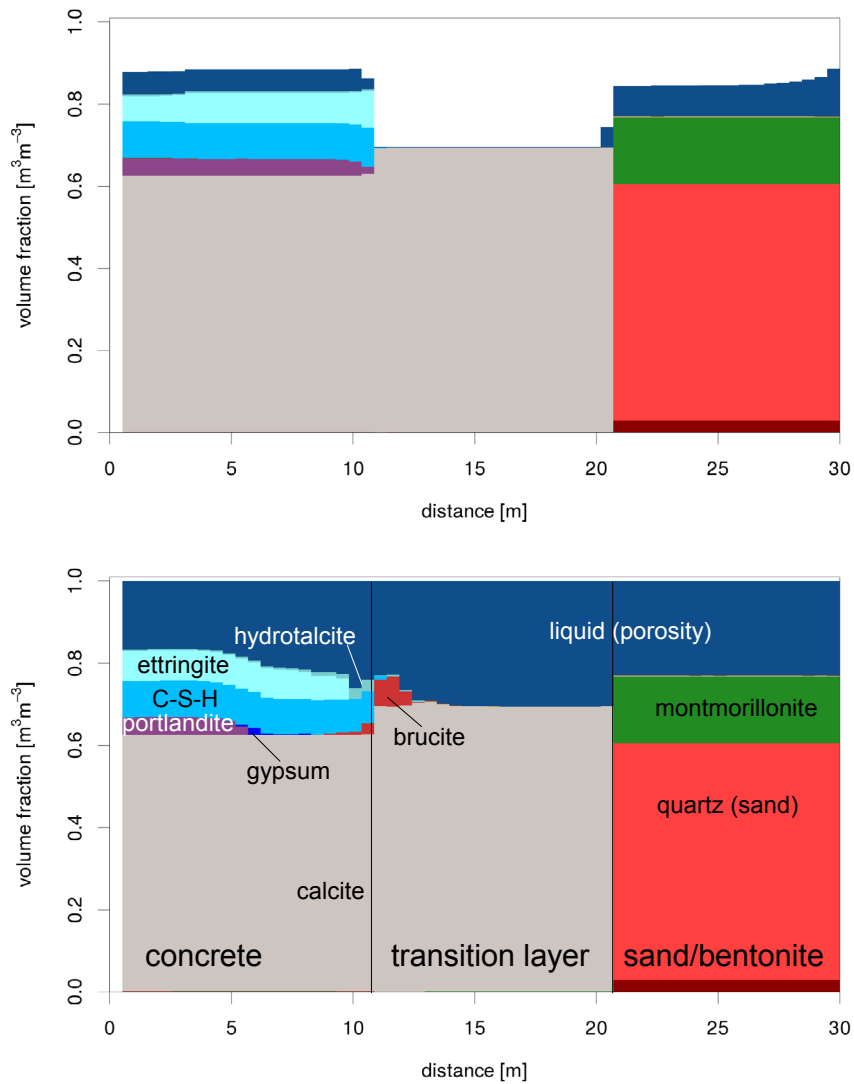


Fig. 3-12: Mineralogical profiles along the top (upper picture) and the bottom (lower picture) of the model domain after 100 000 years.

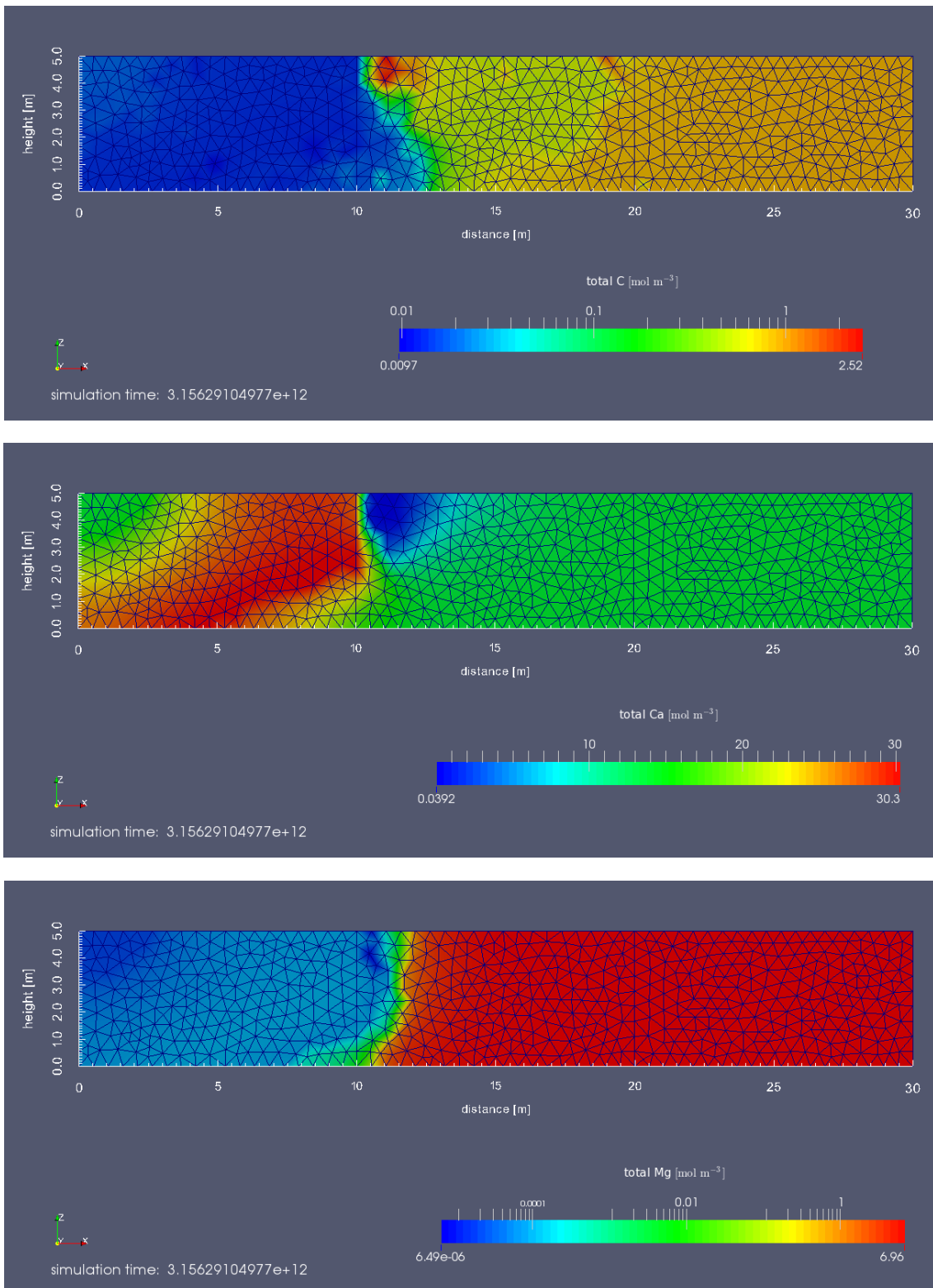


Fig. 3-13: Map of the spatial distribution of selected total component concentrations in the liquid phase at 100 000 years.

From top to bottom: C, Ca, Mg, S, Si.

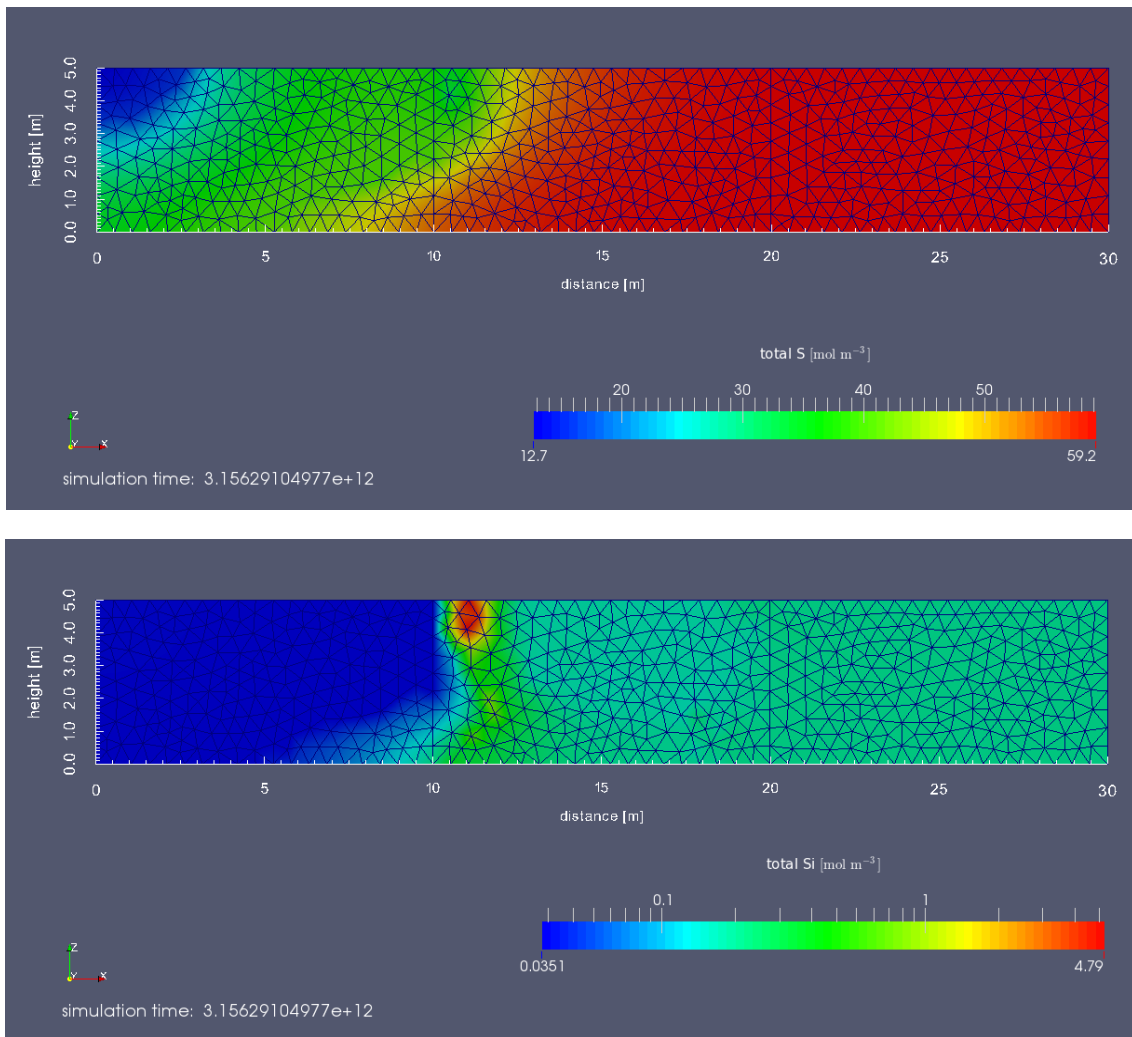


Fig. 3-13: (continued).

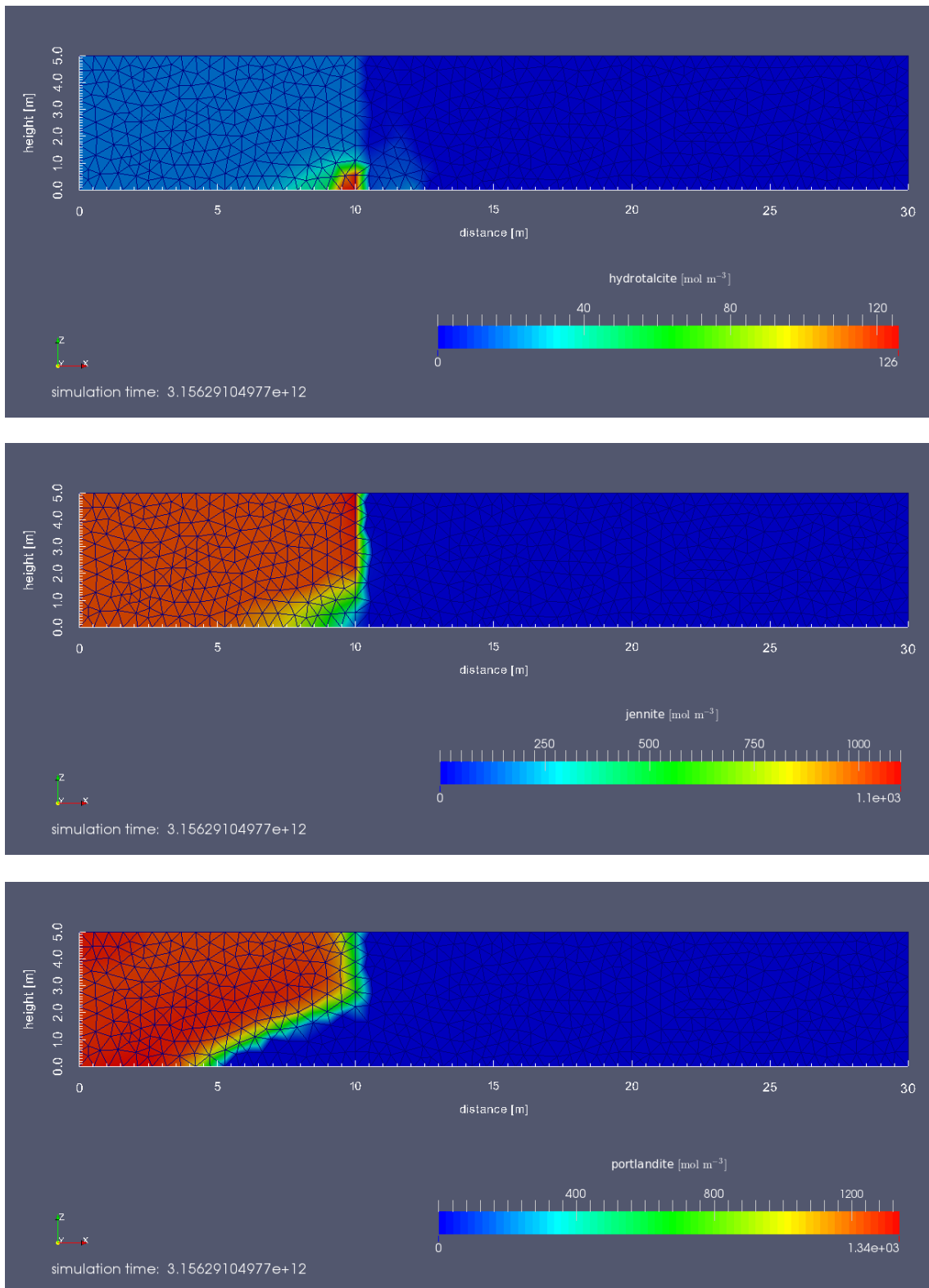


Fig. 3-14: Map of the spatial distribution of main concrete mineral phases at 100 000 years. From top to bottom: hydroxalcite, jennite, portlandite, gypsum, tobermorite, brucite.

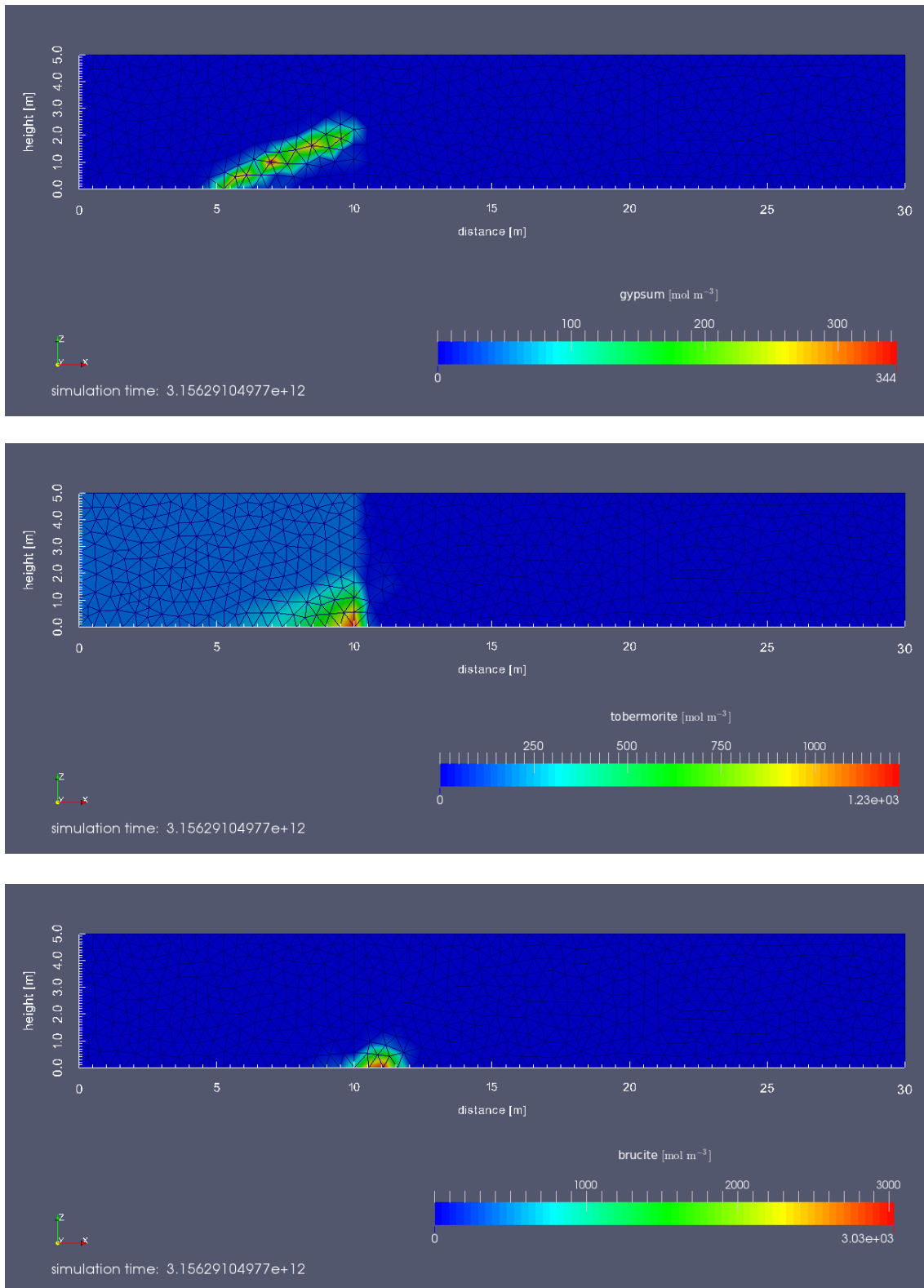


Fig. 3-14: (continued).

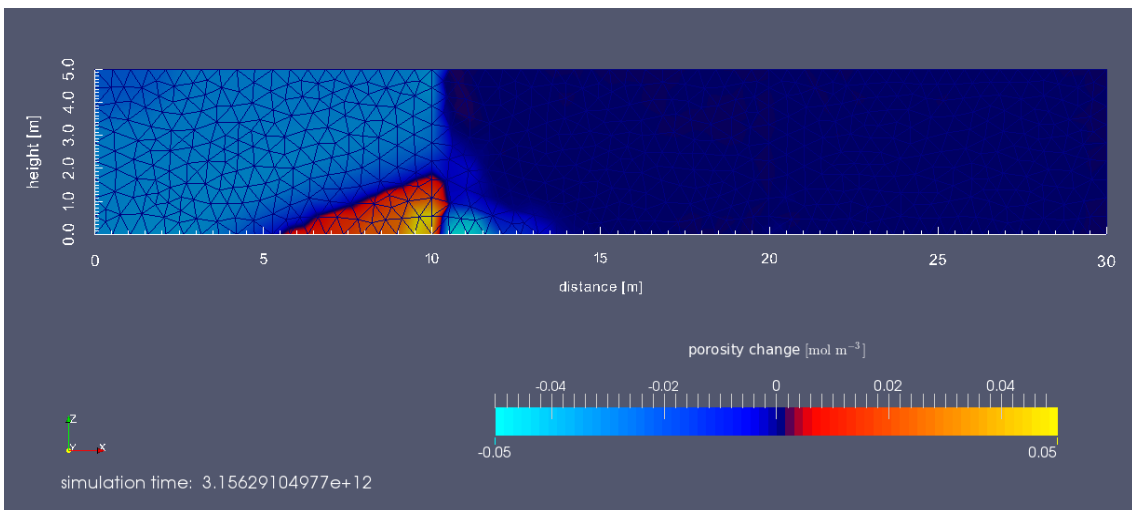
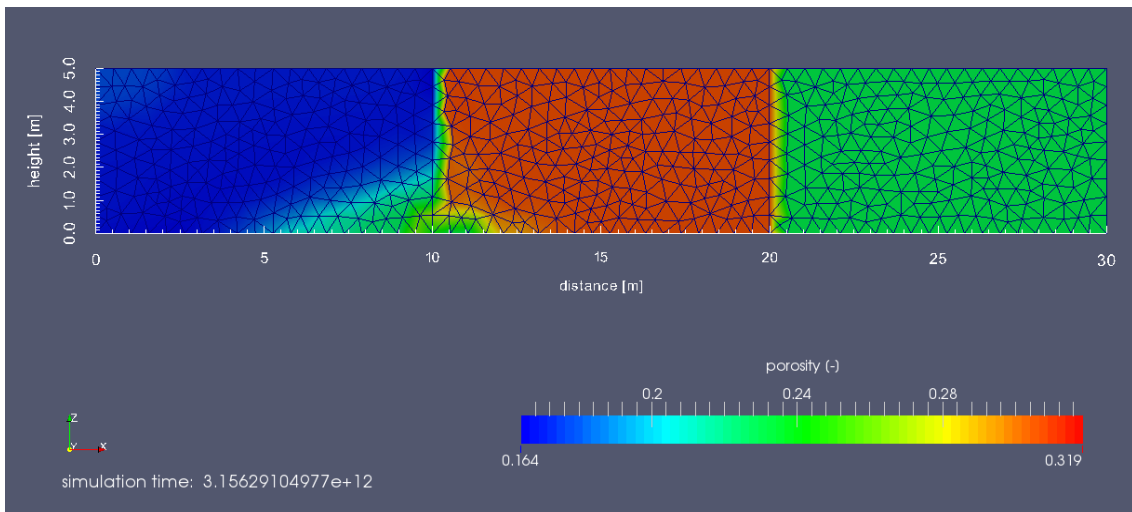


Fig. 3-15: Map of porosity distribution (top) and porosity change (bottom) at 100 000 years. Positive (negative) values of porosity change indicate an absolute increase (decrease) of porosity compared to the initial stage.

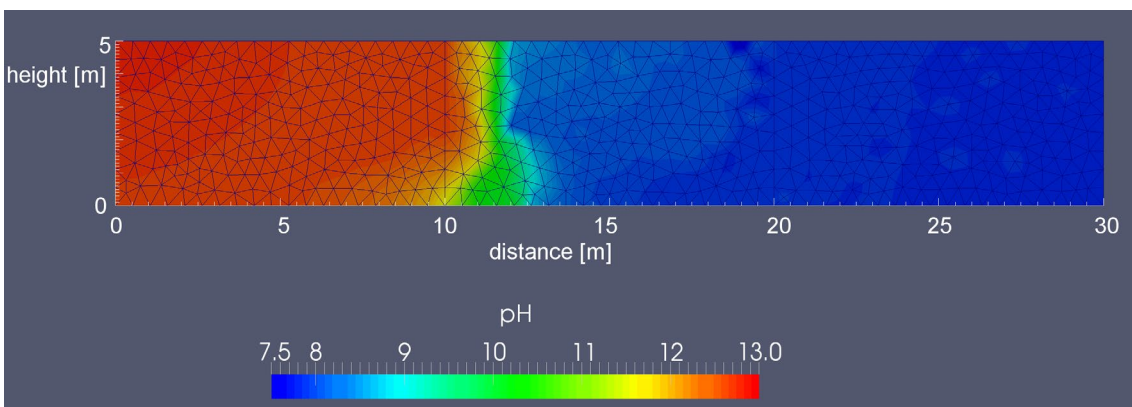


Fig. 3-16: Map of pH at 100 000 years.

3.3.5 Interpretation of results

As explained in the discussion of model assumptions, evolution of saturation and total water flow rates calculated with the present 2-D model are not directly comparable with those calculated by (Senger & Ewing 2009). Water flow in the present model is much higher than in their model and represents a rather extreme case that overestimates the effects of advective transport on the mineralogical and porosity evolution of the system. As there is no purely advective transport regime, i.e. diffusive transport and advective transport are superimposed to a spatially varying degree, it is not possible simply to map the model results to "exchanged pore volumes" in order to de-couple water flow rates from simulation times. Nevertheless, some basic processes can be identified that govern the mineralogical and porosity evolution in the model and will dominate mineralogical evolution for different flow and saturation conditions.

The general model evolution can be described as follows, and as indicated schematically in Fig. 3-17. Host-rock porewater, i.e. Opalinus Clay porewater in the model setup, infiltrates into the access tunnel system and flows along the bottom of the tunnel through the EGTS. As it migrates, the water equilibrates with the different backfill materials. In the present model setup, the sand/bentonite is initially equilibrated with Opalinus Clay porewater and therefore no major mineralogical or compositional changes are to be expected there. Total dissolved components in the sand/bentonite compartment have homogeneous spatial concentrations and there is thus no indication in Fig. 3-13 of reaction fronts originating from the ingress of water from model boundary. Background information on the definition of bentonite and Opalinus Clay porewaters can be found in Berner et al. (2013) and Kosakowski and Berner (2013) and an evaluation of relationship between waters in both media is given in Berner (2011).

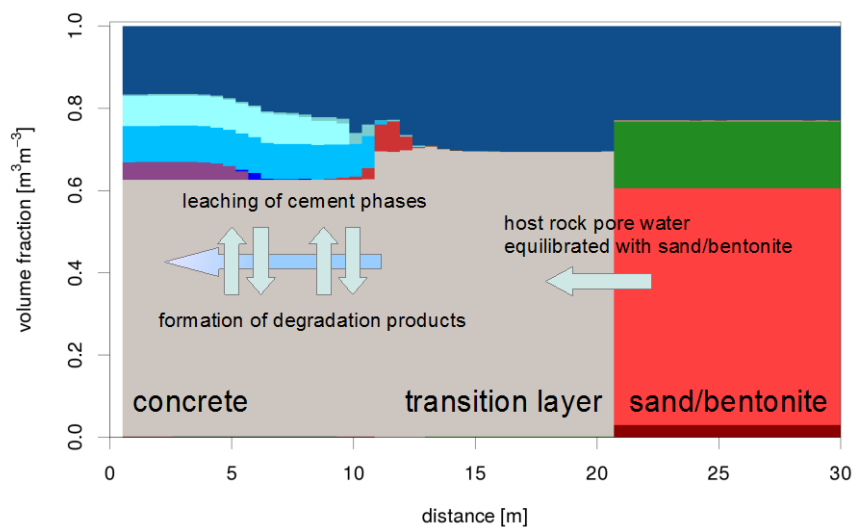


Fig. 3-17: Schematic illustration of major processes in an EGTS where concrete and sand/bentonite compartments are separated by a 10 m layer of calcite gravel according to the 2-D model.

After passing through the sand/bentonite tunnel backfill, water enters the transition layer at the bottom of the model where saturated conditions are present. As in the 1-D model, the transition layer is mainly composed of calcite (Appendix A, Tab. A-1) and is initially equilibrated (or saturated) with Opalinus Clay water. Despite some small differences (e.g. in sulphur) that can be attributed to the slightly different mineral inventories (gypsum), initial water for sand/bentonite and transition layers are very similar.

As the water from the sand/bentonite is not in complete equilibrium with the transition layer material, it causes minor changes in the composition of accessory minerals on entry to the transition layer. The equilibration takes place fastest at the fully saturated bottom and near the interface between the sand/bentonite and the transition layer. Some processes (cation exchange) happen almost instantaneously. Others (clay or zeolite precipitation/dissolution) are kinetically controlled. Changes are slower in the partially saturated part of the transition layer, as the residual saturation is very low and advection and diffusion is thus extremely slow. Dissolution or precipitation of the main transition layer constituent, calcite, due to ingress of water is not expected, since the porewater in both materials is in equilibrium with calcite and the pH of both waters is the same (see the discussion of carbonation in Section 3.2.4). As the equilibration processes are only affected by accessory minerals, there are no significant changes in porosity, as can be seen in Fig. 3-15.

After passing through the transition layer, the hitherto practically unaltered porewater reaches the concrete. The concrete porewater and the water entering into the concrete are in strong disequilibrium (see Appendix A, Tab. A-2). This will cause leaching of the concrete and induces several mineral dissolution and precipitation fronts that evolve with time. As water flux is not very high, even at the saturated bottom of the model domain, a mixed advective-diffusive transport regime is established. Due to the spatial heterogeneity of saturation and the channelling of flow in the saturated bottom of the model domain, the ratio between diffusive and advective solute fluxes is also spatially variable. Mineral precipitation/dissolution fronts move fastest in the lateral direction along the bottom and progress slows down with height (Fig. 3-14). Movement towards the model top is limited due to slow diffusive transport in the residual water.

The different reaction fronts induced in the concrete can be attributed to several processes. The main process causing degradation of concrete is the inflow of water with neutral pH, which affects the stability of cement minerals, i.e. the calcium-hydrates (see e.g. Glasser et al. 2008). Degradation of the concrete follows the model of Berner (1992). After replacement of the initial, stage I concrete porewater (pH > 13), the pH in concrete is buffered at 12.5 by the presence of portlandite (stage II). Ca is released to solution and transported away (Fig. 3-13). After complete dissolution of portlandite, the C-S-H phase is affected (see bottom of Figs. 3-12 and 3-14) and pH drops to ~ 11. Ca is released from C-S-H and the C/S ratio of C-S-H is continuously lowered. In Fig. 3-14, this is reflected by the increased presence of tobermorite, the low C/S end-member of the C-S-H solid solution, in place of jennite, the high C/S end-member of the C-S-H solid solution.

In addition, the inflowing water contains elevated concentrations of S and Mg (Fig. 3-13 and Appendix A, Tab. A-2), causing so-called sulphate and magnesium attacks, respectively. Sulphate attack causes the formation of ettringite (see e.g. Glasser et al. 2008; Taylor 1997; Winter 2009). The Ca necessary to form ettringite is provided by the cement leaching process described above. Note that, in Fig. 3-11, the formation of additional ettringite at 1000 years is only visible near the bottom of the concrete/transition layer interface, whereas, in Fig. 3-12, the volume of the ettringite phase at 100 000 years has increased throughout the concrete domain. The formation of ettringite is limited by the availability of Al from the cement minerals.

Gypsum may form if, as in Fig. 3-14, the supply of Al is exhausted (from dissolution of e.g. monocarbonate, hydrotalcite, see Winter 2009). When the pH drops due to leaching of portlandite and C-S-H, first gypsum and later ettringite dissolve again. The ingress of Mg (Mg-sulphate) rich solutions is characterised by the formation of magnesium hydroxide (brucite) and magnesium silicate hydrates (Taylor 1997; Winter 2009). The model does not show brucite formation at early simulation times. The additional Mg from the water entering the concrete is used instead to form hydrotalcite. In Fig. 3-12 and in Fig. 3-14, brucite formation is visible at 100 000 years at the the concrete/transition layer interface, where concrete degradation is nearly complete and the pH is still elevated. The missing brucite formation at earlier times suggests that, in the model, the formation of brucite needs to be triggered by the dissolution of hydrotalcite, which provides an additional source for Mg. The association of brucite formation with the hydrotalcite dissolution front also prevents brucite accumulating at the interface and clogging porosity.

The strong concentration gradients between the concrete and the transition layer cause diffusion of solutes across the interface between these regions. The diffusive fluxes are low in the partially saturated upper part of the model. They are sufficient to cause some increase in pH in the upper part of the transition layer (Fig. 3-16), but do not cause significant changes in the mineralogical composition near the interface (Fig. 3-12).

CO₂ migration in the gas phase, which is not included in the present model, is discussed further in Appendix D.4.

3.4 Main findings for the example design

Overall, the 1-D calculations for the example EGTS design indicate that porosity changes are relatively minor and caused either by the replacement of mineral phases with phases that have a different molar volume, or by distributed precipitation of minerals due to diffusive mixing of solutes originating from different materials. The porosity changes are far less than would be required for clogging to occur.

The EGTS design, with calcite as transition layer backfill material and as concrete aggregate, is chosen such that neighbouring materials do not impose strong geochemical gradients across the interfaces. In particular, the porewaters of the sand/bentonite tunnel backfill (quartz, montmorillonite and small amounts of calcite) and the calcite transition layer (calcite, with minor amounts of quartz and montmorillonite) are nearly identical, each having the same pH and similar porewater compositions. Not surprisingly, there are no reaction fronts originating from the interface between these materials. Stronger gradients exist across the interface between the calcite transition layer and the concrete backfill. In particular, concrete porewater has a much higher pH than that initially present in the transition layer and has a substantially different initial composition. C-S-H is precipitated in the transition layer. This reaction is driven by the availability of Si provided by the montmorillonite/quartz dissolution, primarily in the sand/ bentonite backfill, and Ca originating from portlandite dissolution in the concrete. C-S-H precipitation is not, however, highly localised, but distributed across the whole transition layer, reducing its impact on porosity.

To test the influence of saturation on the mineralogical evolution of the EGTS, an illustrative 2-D model was set up. It consists of a simplified cross-section through a concrete and sand/bentonite separated by a calcite gravel layer. It implements full saturation at the bottom of the model and a transition (partially saturated) layer above. The model calculates a scenario where water flows through the transition layer towards the concrete. The simulation results for the repository cavern model of Senger & Ewing (2009) provide no indication that significant amounts of high pH concrete porewater will flow from the emplacement rooms into the sand/bentonite backfill. Rather, liquid flow from the access tunnel system through the transition layer and into the emplacement rooms is to be expected for about 1000 years. The model represents the hypothetical, more extreme case where such flow is maintained up to 100 000 years. In the transition layer, liquid will flow along the bottom of the tunnel into emplacement room. Although water flow is effectively restricted to the fully saturated parts of the model, they are low enough that diffusive transport strongly influences the evolution of the system.

Essentially, chemical interactions in the saturated material at the bottom of the modelled system occur as in the 1-D calculations. In particular, calculated mineralogical and porosity changes are similar in both model approaches. Concrete degradation is further advanced in the 2-D model, as inflow of water causes much higher fluxes of S and Mg into the concrete. However, the 2-D model demonstrates that the extent and magnitude of mineralogical and porosity changes at material interfaces strongly depends on the change of diffusive and advective transport with saturation. Thus, changes towards the top of the modelled system are much more limited than towards the bottom.

4 Sensitivity to Design Variables

4.1 Sensitivity to length extent of the transition layer

The calculations shown in Fig. 4.1 illustrate the effects of the length of the transition layer on the mineralogical evolution of the system. As in the calculations in Chapter 3, the calculations assume that calcite material is used in the transition layer and the concrete uses calcite aggregate. The length of the transition layer is varied between 1 m and 10 m, 10 m being the assumed length in the calculations in Chapter 3.

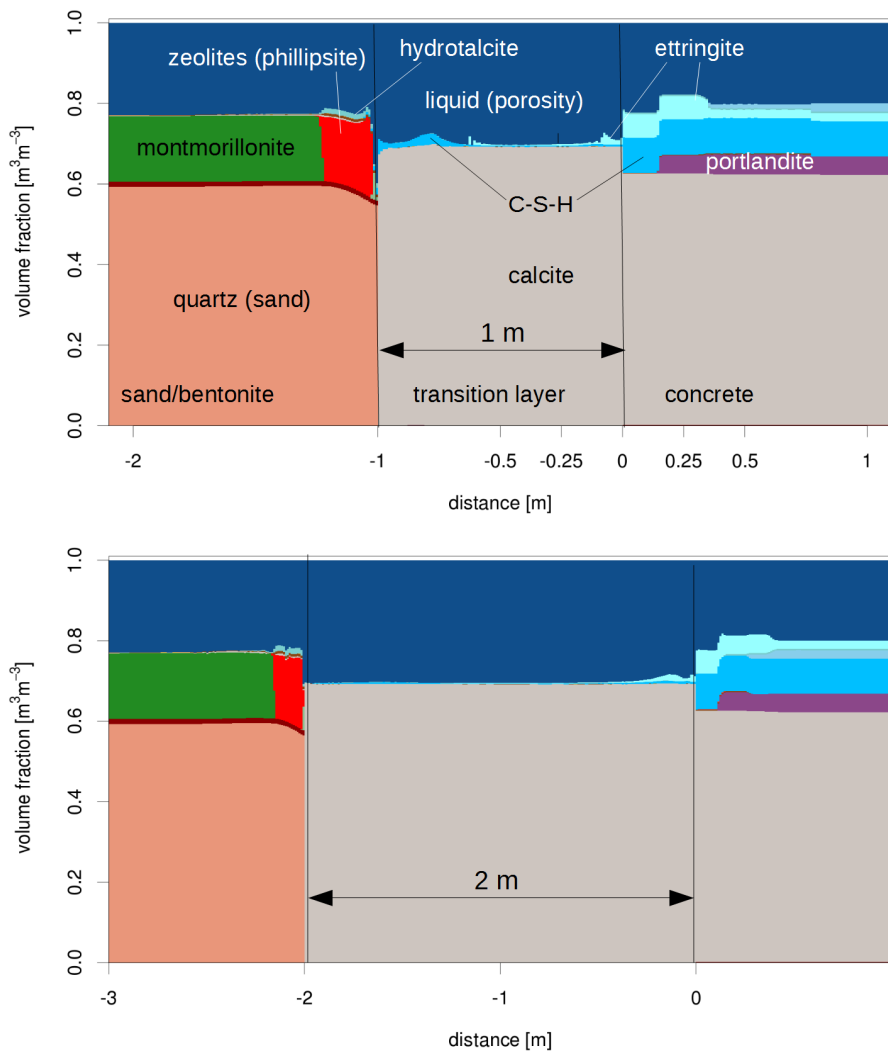


Fig. 4-1: Mineralogical profiles across a 1 m, a 2 m, a 5 m and a 10 m long layer (from top to bottom) composed of calcite after 2000 years.

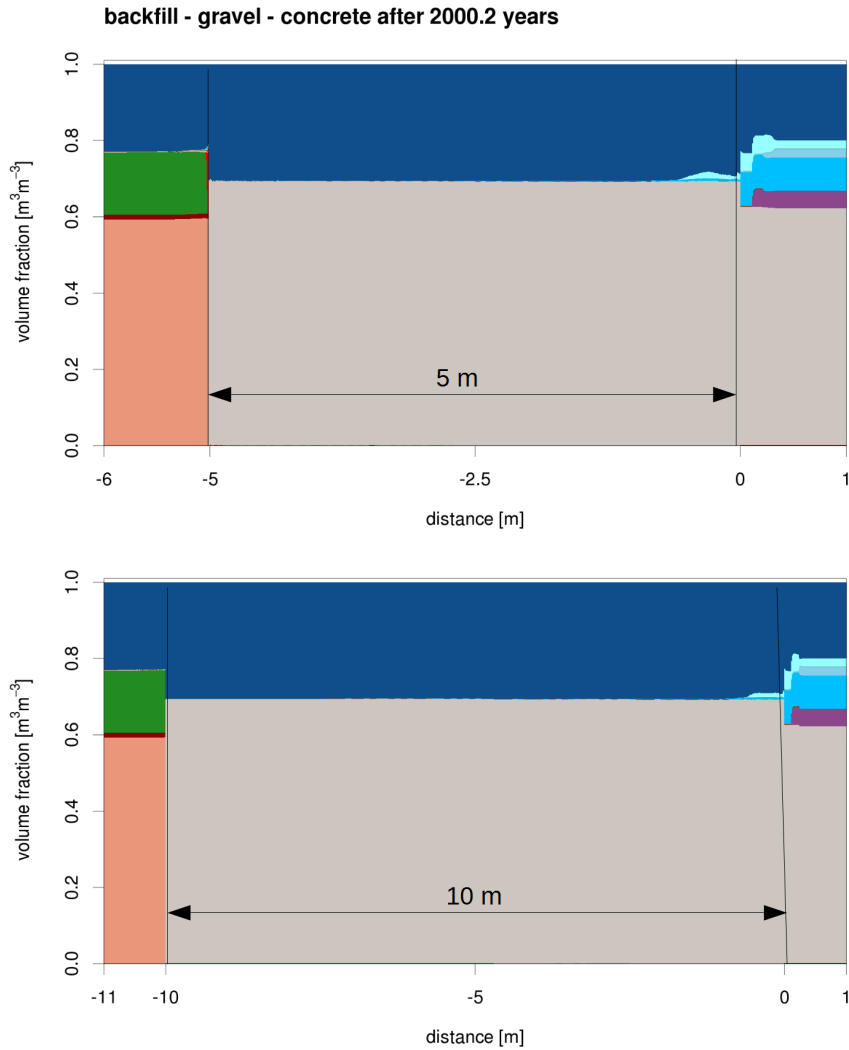


Fig. 4-1: (continued).

The progress of the portlandite dissolution front in concrete, as well as the montmorillonite dissolution front in the sand/bentonite is sensitive to the length of the transition layer (Fig. 4-2). The progress of these fronts after 2000 years is much larger in the case of a 1 m long transition layer compared with the longer transition layers. For a 10 m long transition layer, no alteration front in the sand/bentonite is visible at this time. The progress of montmorillonite dissolution in the sand/bentonite layer depends on the transition layer length, as global solute concentration gradients between the sand/bentonite and the concrete depend on the distance between both materials. Concentration gradients across longer transition layers result in lower solute fluxes and a reduced montmorillonite dissolution rate. Fig. 4-2 plots the progress of the montmorillonite dissolution fronts in the sand/bentonite for different transition layer lengths. For the 1 m transition layer montmorillonite dissolution is fastest and for the 10 m transition layer is slowest. The results for models with different transition layer length are normalized such that at approximately the same time (0 years) montmorillonite dissolution starts at the sand/bentonite to gravel interface (distance = 0 m).

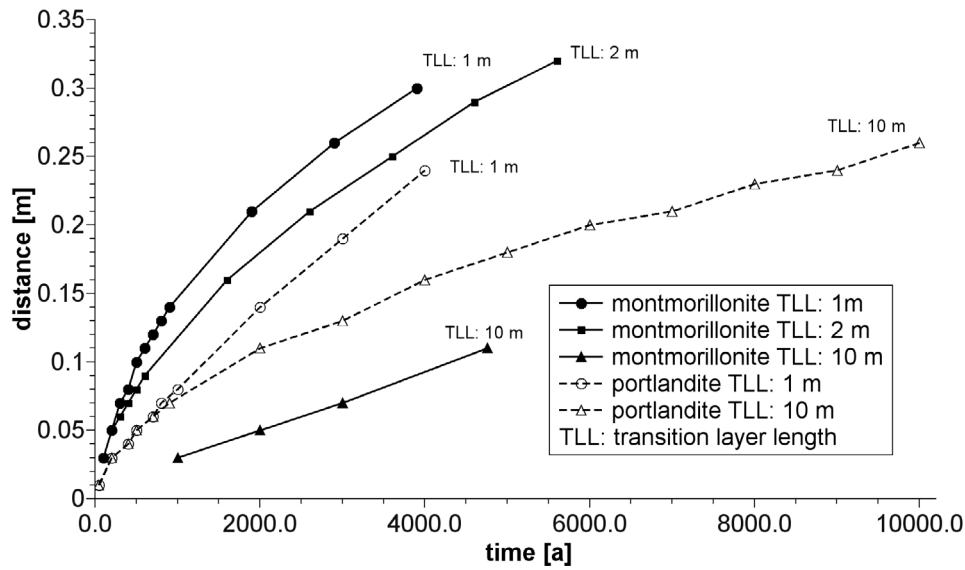


Fig. 4-2: Progress of montmorillonite dissolution front in sand/bentonite and progress of portlandite dissolution front in concrete with time for different transition layer lengths (TLL).

Simulation times for montmorillonite fronts are normalized such that dissolution starts at 0 years at the interface between sand/bentonite and transition layer (distance = 0 m). Portlandite dissolution starts at the transition layer/concrete interface (distance = 0 m).

Dissolution of montmorillonite in the sand/bentonite occurs once high-pH pore liquid from the concrete diffuses across the transition layer. The time taken for this to occur clearly increases with transition layer thickness. To understand the dependency in a more quantitative manner, it should be noted that, according to Appendix A, Tab. A-1, the calcite layer contains small amounts of accessory minerals (consistent with the methodological aim noted in Section 1.4 of striving for realism in the representation of mineralogy and porewater chemistry). One of these minerals is montmorillonite. Montmorillonite is dissolved as soon as high-pH porewater from the concrete diffuses into the transition layer. Associated porosity changes in the layer are minimal, since the relative mass of accessory minerals initially present is low, amounting to only about 2 ‰ of the overall mass. Fig. 4-3 shows the position of the montmorillonite dissolution front first in the transition layer and, subsequently, in the sand/bentonite layer as a function of time. The speed of the dissolution front (slope of curve) is related to the amount of montmorillonite present and is therefore different in the transition layer (only minimal amounts) and in the sand/bentonite (montmorillonite mass fraction is 0.183 based on dry weight).

Typically in diffusive systems, the progress of a dissolution fronts $x(t)$ can be described by a square root dependence with time t :

$$x = \sqrt{D_a t}. \quad (4-1)$$

Here, D_a is a proportionality constant in form of an apparent diffusion coefficient. The value of D_a depends on the reactions occurring at the dissolution front and the amount of reactants. In Fig. 4-2 shows clearly the square root shape for layer length of 1 and 2 meters and in Fig. 4-3 the square root dependence is visible in the linear behaviour of the double-logarithmic plot at late times which shows progress in the sand/bentonite.

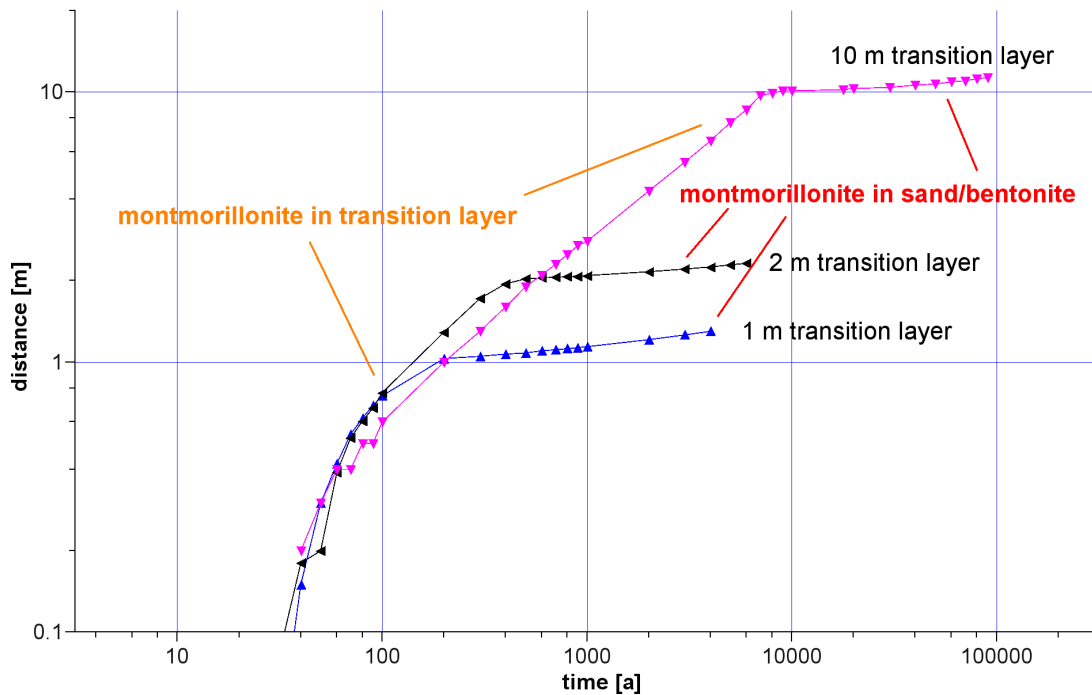


Fig. 4-3: Progress of montmorillonite dissolution fronts in transition layer and in sand/bentonite with time for different transition layer lengths.

Distance refers to the distance from the concrete/transition layer interface. For a 1 (10) m long transition layer the dissolution front moves into the sand/bentonite compartment at a distance of 1 (10) m. Please note the logarithmic scale of time and distance axis.

Where the montmorillonite dissolution is influenced by reaction kinetics in addition to the diffusive transport of solutes, progress of the fronts is expected to be non-linear on a double-logarithmic plot. This is the case at early times in Fig. 4-3. Thereafter, the diffusion-controlled dissolution of montmorillonite in the transition layer is apparent in the relatively high-gradient, linear behaviour. Once the front reaches the sand/bentonite compartment, the progress of the dissolution front is slowed, since more montmorillonite has to be dissolved for the front to progress by a given distance. The gradient of the lines plotted in Fig. 4-3 falls after a certain time, this time being a function of transition layer length. This is more clearly visible in Fig. 4-2, which plots the progress of dissolution fronts in the sand/bentonite and in concrete for different transition layer lengths. A longer transition layer results in lower concentration gradients across the transition layer and delays the progress of the dissolution fronts.

The progress of dissolution fronts arising from a direct contact of host rocks and concrete has been extrapolated in Kosakowski et al. (2014) and is shown to be typically a few meters in 100 000 years, if, as is the case here, porosity clogging is assumed not to occur. In the present calculation, progress of dissolution fronts is less than this, since large scale concentration gradients between clay and cement materials are reduced by the presence of the transition layer.

4.2 Sensitivity to choice of filling material for transition layer and concrete aggregate

4.2.1 Calculation cases

In this section, sensitivity to the choice of materials for the concrete aggregate and for the filling of the transition layer is examined. Two calculation cases are defined and analysed with the 1-D model:

1. Calcite aggregate in the concrete is replaced by quartz aggregate;
2. Calcite aggregate in the concrete is replaced by quartz aggregate and, in addition, the calcite gravel in the transition layer is replaced by quartz gravel

The cases are illustrated in Fig. 4-4. The second of these cases is also analysed using the 2-D model and the results are presented in Appendix C. An additional, more simplified case in which calcite aggregate in the concrete is replaced by a hypothetical, inert aggregate and, in addition, the calcite gravel in the transition layer is replaced by quartz sand is also presented in Appendix C.

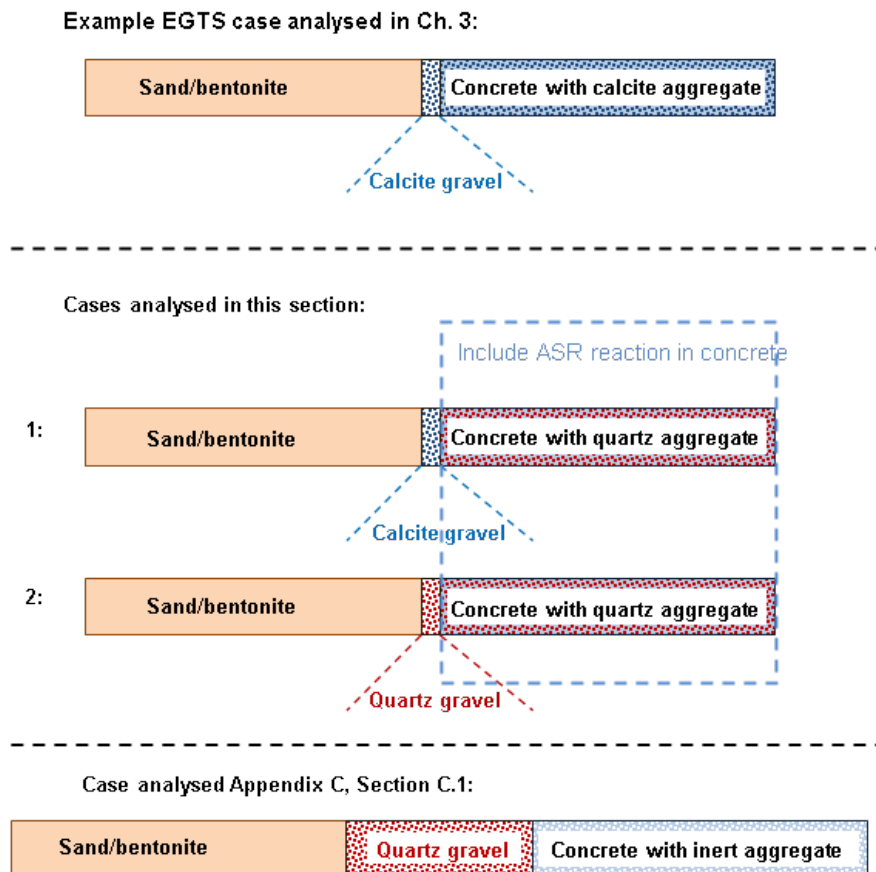


Fig. 4-4: Overview of the three calculation cases analysed in this section. Cases in which the alkali-silica reaction (ASR) in concrete are outlined.

The first two calculation cases provide insight into possible consequences in terms of mineralogical and porosity changes when materials within the EGTS are not in thermodynamic equilibrium. In particular, the replacement of calcite aggregate by quartz aggregate in the concrete will lead to initial chemical disequilibrium in this material and the alkali-silica reaction (ASR) is expected to occur. In short, in the ASR, silica phases in the concrete aggregate react with the calcium and hydroxide ions in the cement porewater to produce C-S-H phases (in gel or crystallised forms). The reaction is thus essentially identical to the C-S-H formation described in Section 1.2, except that the necessary dissolved species that take part in the ASR reaction are already present where the reaction takes place, and do not need to be transported there by diffusion.

From a chemical point of view, the ASR could further reduce the possibility of clogging, since it will act as a sink for calcium hydroxide that could otherwise diffuse into the transition layer. C-S-H will form locally and will therefore be distributed throughout the concrete rather than localised near interfaces with silica-bearing minerals. The formation of C-S-H phases by the ASR is accompanied by cracking and may lead to deterioration of the mechanical performance of the concrete (although, in the present context, this may even be advantageous, since gas permeability would increase). In the very long term, the mineralogy in the concrete is changed and pH drops towards neutral values. There exists a vast literature on this topic and, more generally, on how to test the reactivity of aggregates (see for a recent review Lindgård et al. 2012). Nonetheless, few long term studies exist that cover the typical life time of engineered structures (e.g. Peterson et al. 2006) and uncertainties regarding the long-term development of this reaction are therefore high.

It should be noted that one major difference between the present study and the earlier modelling study of clay/cement interfaces of Kosakowski & Berner (2013) is the treatment of the concrete aggregate. In the present study, the aggregate is composed either of calcite or quartz. Kinetic control is assumed for the dissolution/precipitation reaction for quartz, with reaction constants taken from Palandri & Kharaka (2004), see Appendix B. The reactivity of calcite aggregate is not assumed to be controlled kinetically, since calcite is known to react rapidly compared with the period of investigation. The implemented kinetic law for the dissolution of SiO_2 uses the specific reactive surface area to determine the dissolution rate for a given rate constant. The reactive surface area of the quartz aggregate is set according to the surface area of particles of "Monokorn" sand with a diameter of 2.8 mm, assuming these to be spherical.

The sand in the sand/bentonite backfill is treated in the same way. Where quartz is used as the filling material for the transition layer, the reactive surface area in the layer is set to match gravel of 5 cm diameter.

4.2.2 Calculation results

Fig. 4-5 shows calculated mineralogical profiles and porosities across the EGTS transition layer and the adjoining regions for the case where calcite aggregate in the concrete is replaced by quartz aggregate. The evolution of pH with time is shown in Fig. 4-6 and the evolution of the porosity in Fig. 4-7.

The most striking mineralogical changes are those that occur in the concrete, associated with the ASR reaction (see discussion in Section 3.2.4). The results show only minor porosity changes and there are no indications that these could lead to pore clogging (see discussion in Section 3.2.4). Although large amounts of C-S-H precipitation occur, the precipitates are distributed fairly broadly throughout the concrete (and, to a minor extent, and the interface between the sand/bentonite and the transition layer). Unlike the case analysed in Section 3.2, the pH in the concrete drops significantly after a few hundred years.

Fig. 4-8 shows the mineralogical evolution across the transition layer and the adjoining regions for the case where calcite aggregate in the concrete and the calcite gravel in the transition layer are replaced by quartz aggregate and quartz gravel. The evolution of pH with time is in this case is shown in Fig. 4-9 and the evolution of the porosity in Fig. 4-10.

The mineralogical evolution is very similar to the previous case, in which the transition layer is filled with calcite gravel. The evolution of pH is also very similar in the two cases; again, the pH in the concrete drops significantly after a few hundred years.

Note that the oscillations in the results, e.g. the spikes in the mineralogy shown in the bottom graphs of Fig. 4-8 and in the corresponding figure for the porosity (Fig. 4-10) are identified as numerical artefacts, as discussed further in Appendix D.3.

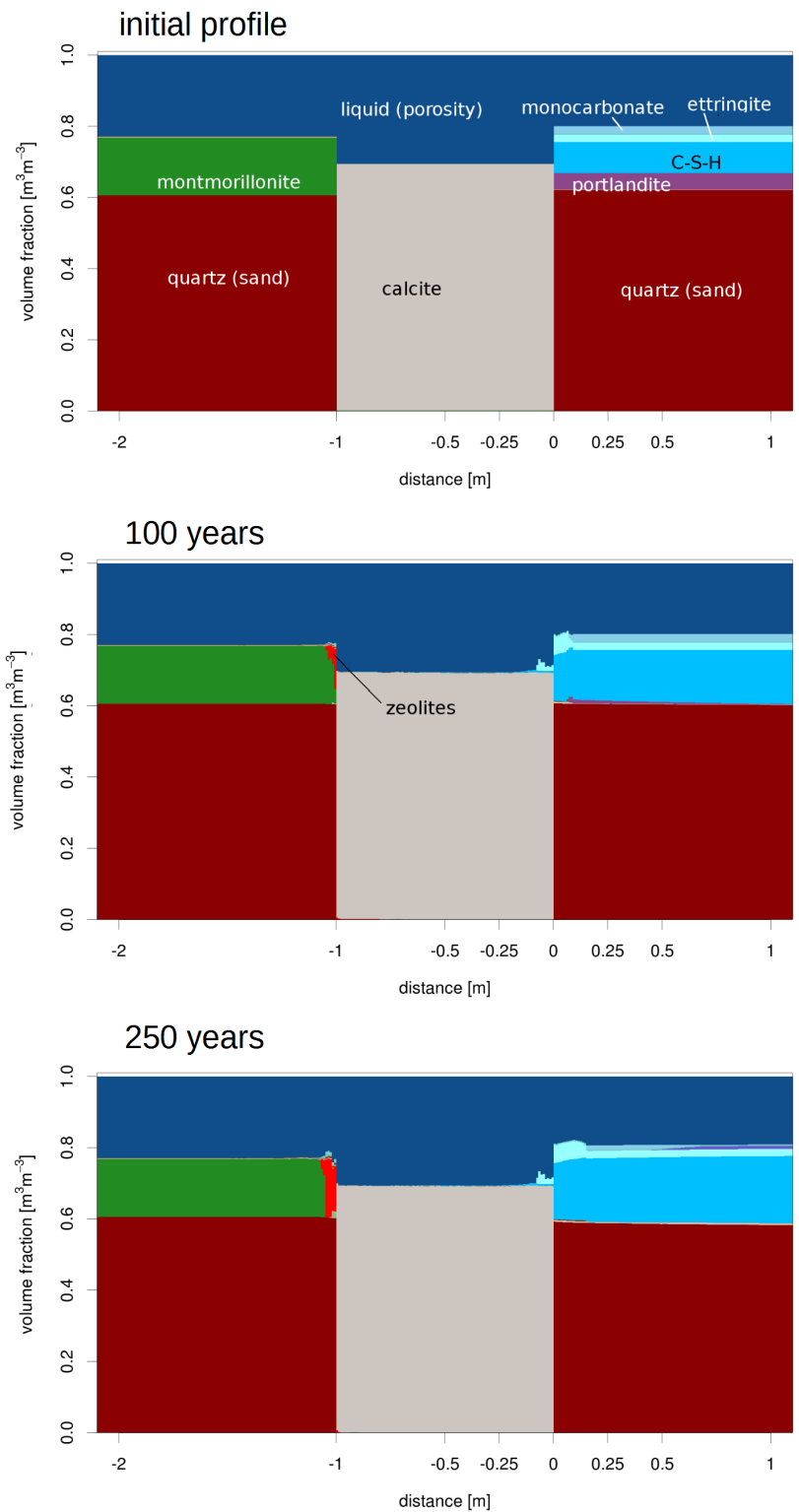


Fig. 4-5: Mineralogical profiles at different times across a 1 m long transition layer composed of calcite and the adjoining regions in a case where calcite aggregate in the concrete is replaced by quartz aggregate.

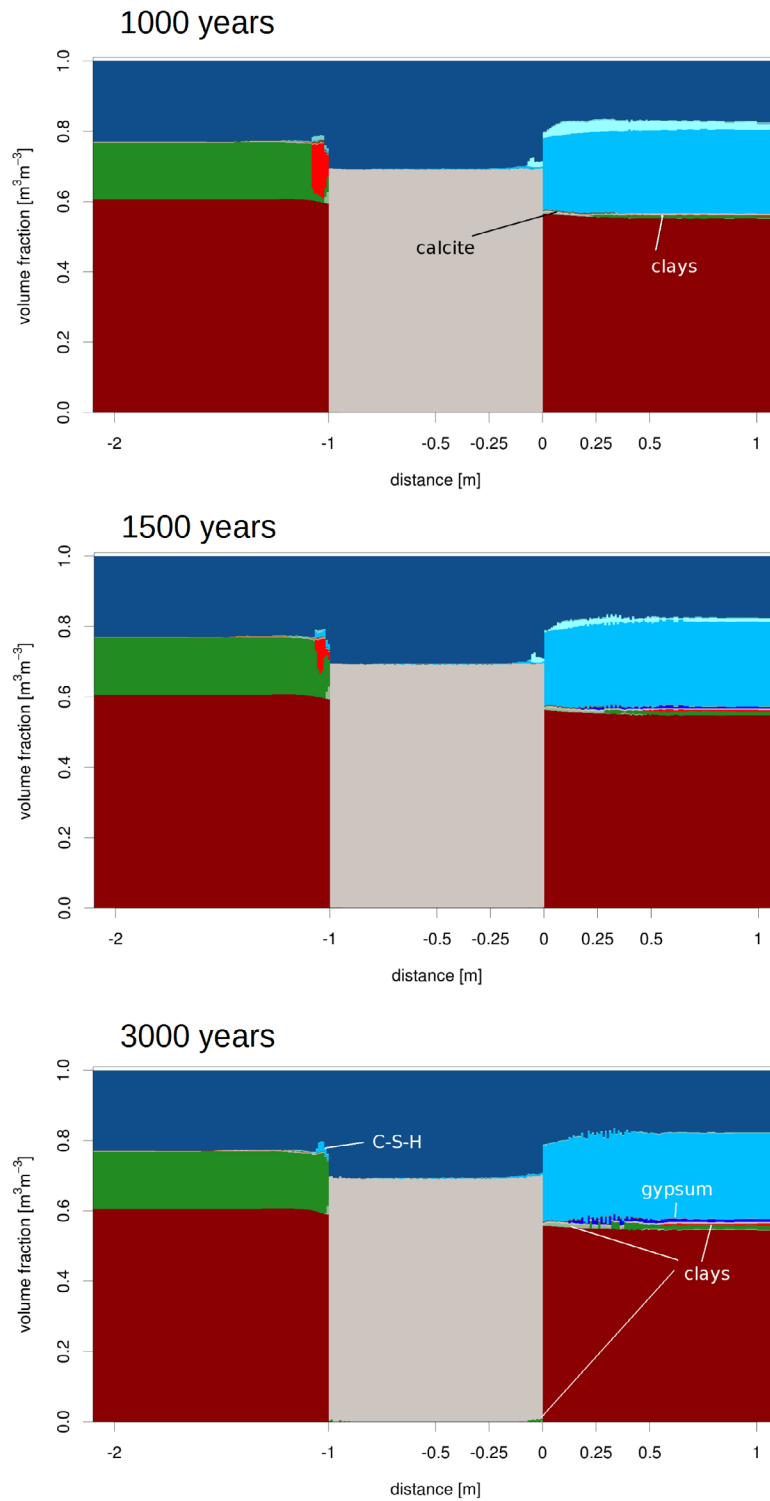


Fig. 4-5: (continued).

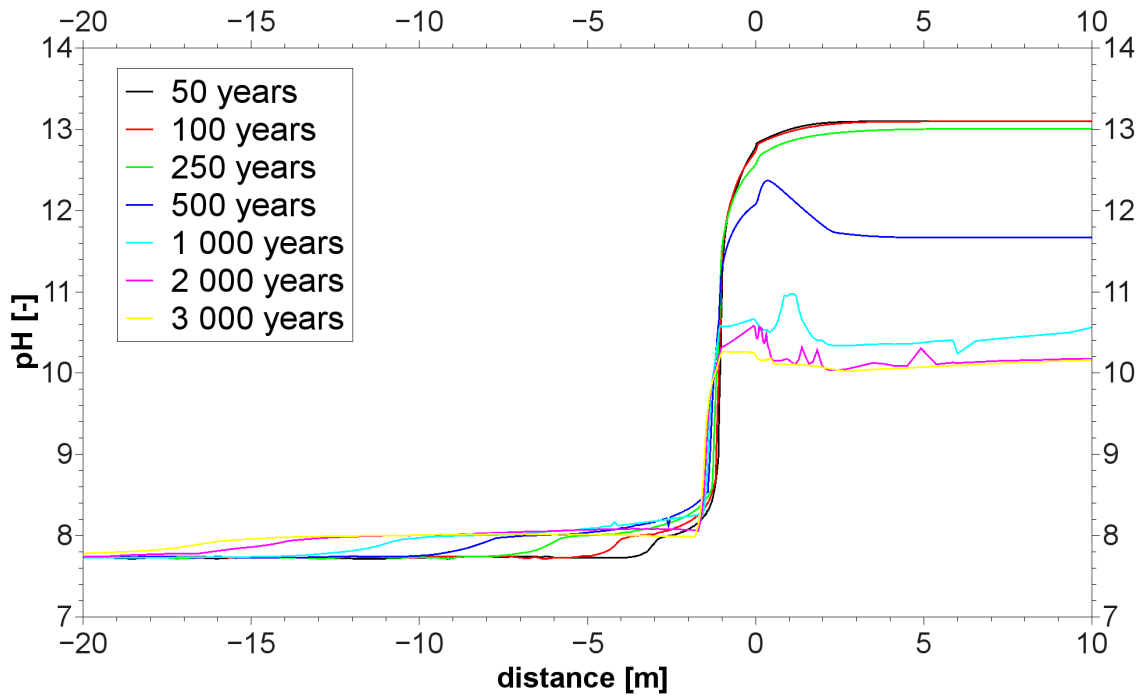


Fig. 4-6: Evolution of pH within a 1 m long transition layer composed of calcite and the adjoining regions in a case where calcite aggregate in the concrete is replaced by quartz aggregate.

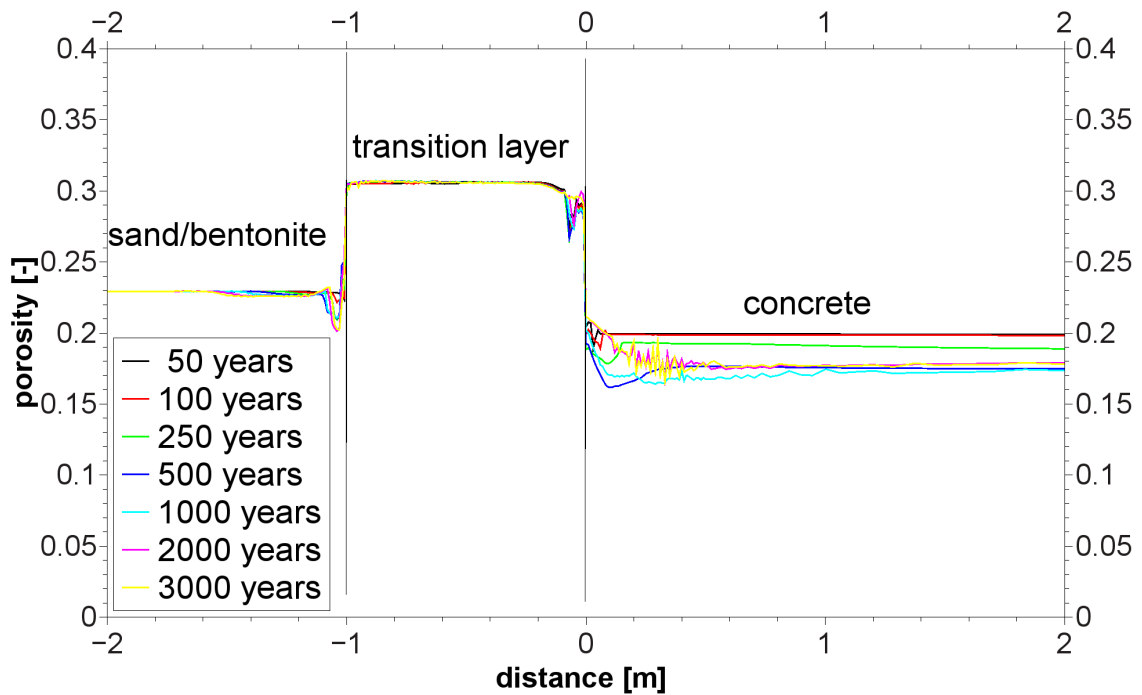


Fig. 4-7: Evolution of porosity within a 1 m long transition layer composed of calcite and the adjoining regions in a case where calcite aggregate in the concrete is replaced by quartz aggregate.

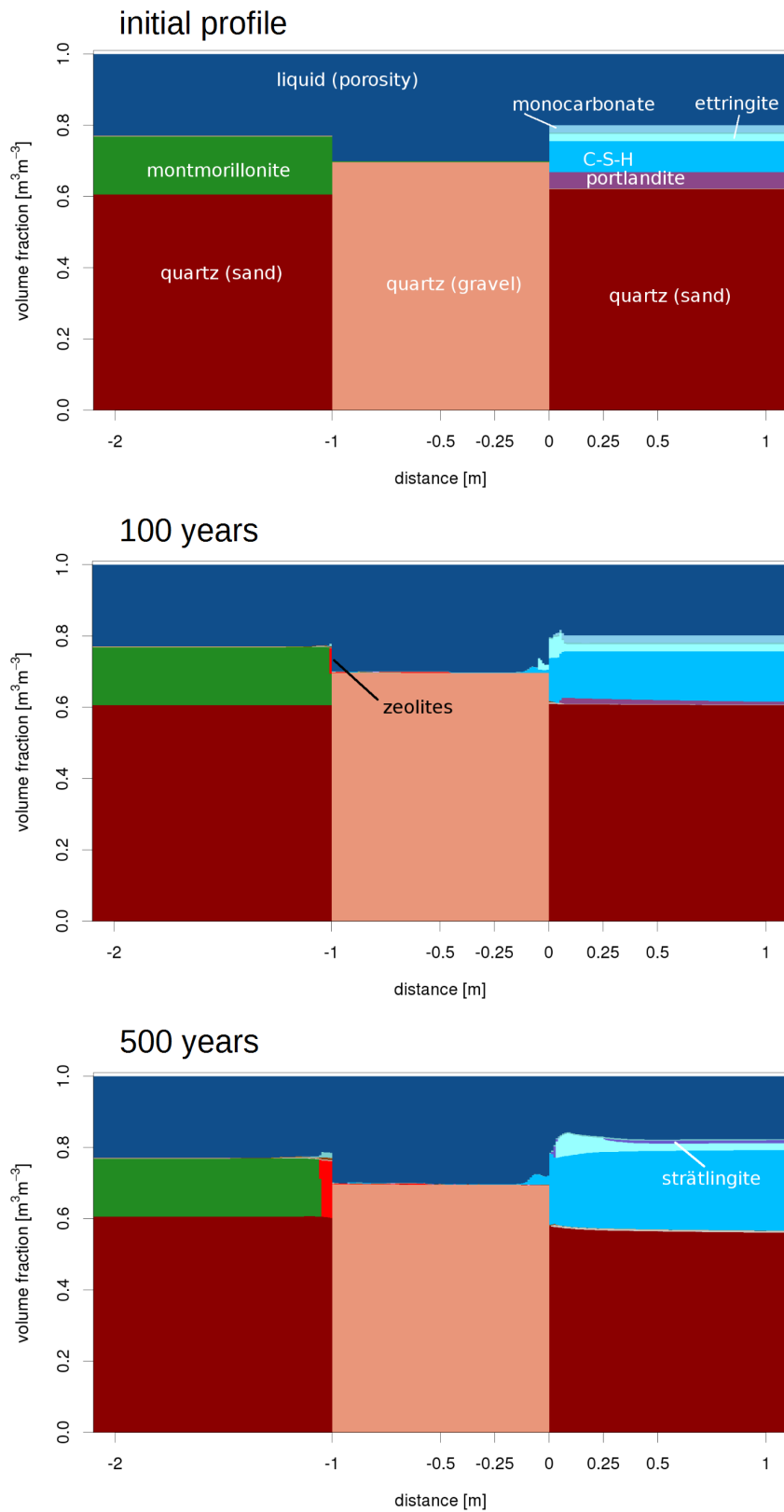


Fig.4-8: Mineralogical profiles at different times across a 1 m long transition layer composed of quartz gravel and the adjoining regions in a case where calcite aggregate in the concrete is replaced by quartz aggregate.

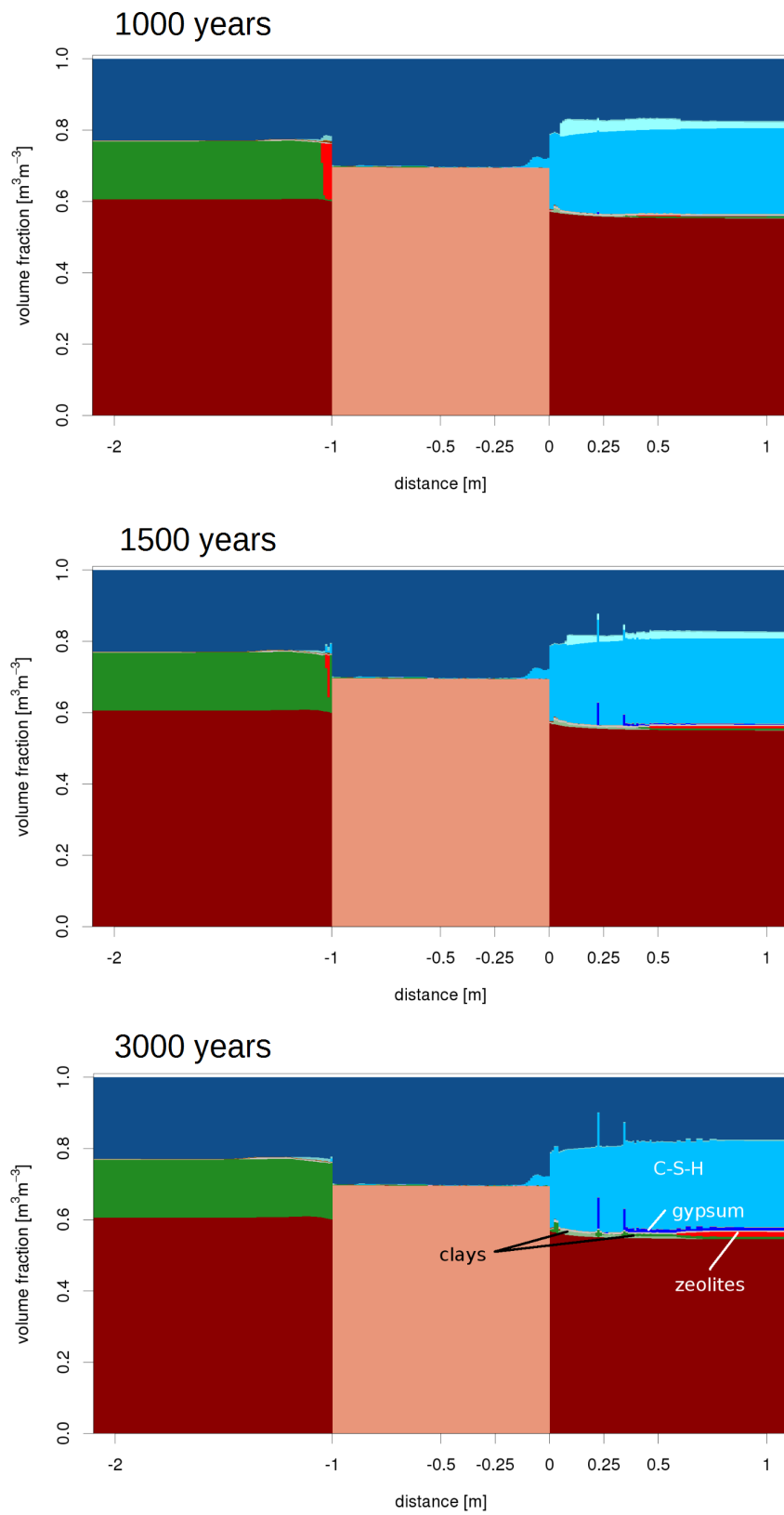


Fig.4-8: (continued).

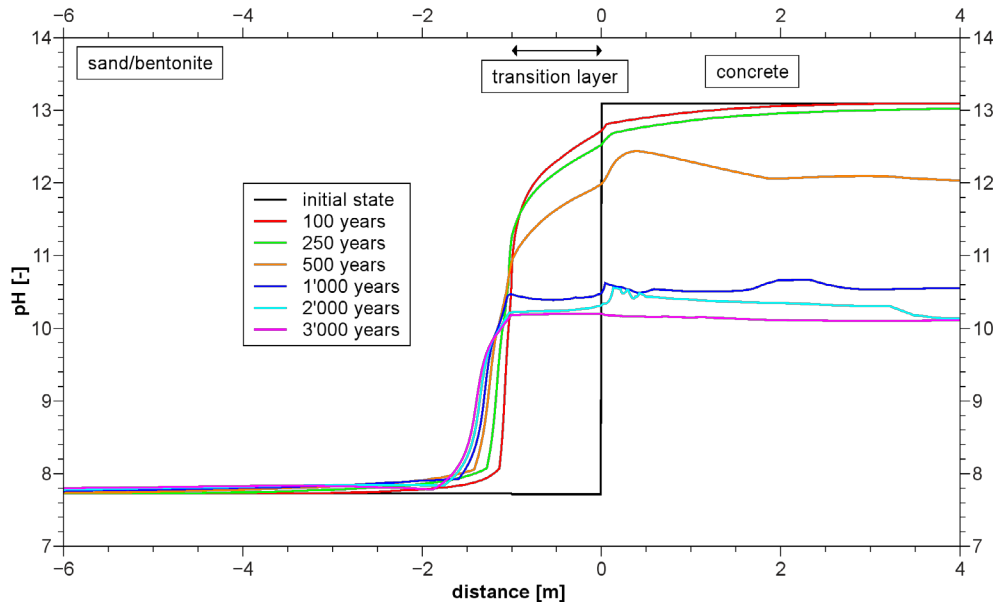


Fig. 4-9: Evolution of pH within a 1 m long transition layer composed of quartz gravel and the adjoining regions in a case where calcite aggregate in the concrete is replaced by quartz aggregate.

This calculation case uses an equilibrium chemistry approach.

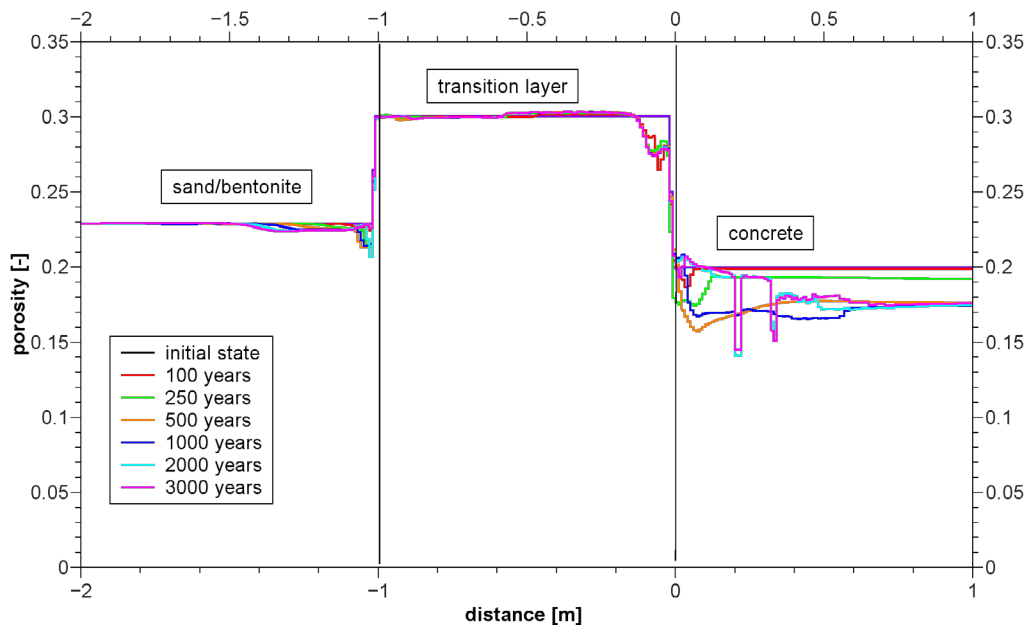


Fig. 4-10: Evolution of porosity within a 1 m long transition layer composed of quartz gravel and the adjoining regions in a case where calcite aggregate in the concrete is replaced by quartz aggregate.

This calculation case uses an equilibrium chemistry approach.

4.2.3 Interpretation of results

In the two calculation cases considered above, where quartz aggregate is used in the concrete, the ASR reaction in the concrete largely governs system evolution. The high pH in the concrete promotes dissolution of the quartz aggregate and frees Si. Portlandite is rapidly consumed within around the first 100 years and frees Ca. Most of this Ca does not, however, diffuse into the transition layer. Rather, the Si and Ca in solution react to precipitate C-S-H phases which replace the dissolved portlandite and quartz.

In the case of the quartz transition layer, the portlandite is dissolved slightly more rapidly near the interface with the transition layer because of the diffusion of Ca towards the transition layer, where it is mostly consumed by the formation of Si-rich C-S-H. In contrast to calcite solubility (Fig. 3-6), the solubility of SiO₂ increases with pH (Fig. 4-11). This causes higher concentrations of total Si at elevated pH. The calculation indicates that the amount of C-S-H precipitation in the quartz transition layer is small, since much of the Ca released from portlandite dissolution is consumed within the concrete by the ASR reaction. In the model setup, the sand in the concrete has a higher reactive surface area than the gravel in the transition layer. In addition, the kinetic parameterisation of quartz dissolution shows a faster dissolution at elevated pH. As a consequence, quartz dissolution is fast in concrete and Ca is mostly already consumed in the concrete. This suppresses the flux of Ca towards the interface and hence also the localised accumulation of C-S-H¹⁰. Only a small amount of C-S-H precipitation is visible in Fig. 4-8 near the interface between the transition layer and the concrete.

In both cases, monocarbonate in the concrete is consumed and temporarily replaced by strätlingite, which then later redissolves. After about 2000 years, ettringite also dissolves. The dissolution of strätlingite and ettringite is accompanied by the precipitation first of zeolites and later of clay minerals. The dissolution of sulphate-rich cement phases results in the precipitation of gypsum. It should be noted that the thermodynamic setup of the model does not include cement mineral phases that adsorb hydroxide ions (or anions like Cl⁻). As a result, the pH in the concrete remains high (in excess of 13) for more than 100 years after the portlandite has dissolved, due to the remaining presence of hydroxide ions, which diffuse only slowly into the transition layer. Only after about 1000 years is the pH low enough (below pH 11) that first zeolites and later clay minerals become stable. Note also that the timing of this drop depends on the model parameterisation of the kinetic control of quartz aggregate dissolution.

The ultimate stage is a completely degraded concrete with silica-rich C-S-H, SiO₂ aggregate and minor amounts of clays and gypsum. Small amounts of ettringite are temporarily precipitated in the transition layer near its interface with the concrete. This is triggered by the sulphate present in the porewater, as there is no sulphate source in the transition layer minerals. After the pH drops due to ASR, the ettringite dissolves again. It should be noted that the ASR causes a relatively small porosity decrease of 0.02, which results in a porosity of ~ 0.18 for the degraded concrete (Figs. 4-7 and 4-10).

As in the case analysed in Chapter 3, the model calculates a slight, but extended increase of pH in the sand/bentonite (Fig. 4-6). This slightly elevated pH causes the dissolution of quartz and, especially in the case of a calcite transition layer, the precipitation of a small amount of C-S-H at the interface between the transition layer and the sand/bentonite. A more pronounced change at the interface in both cases is the development of a small and temporary zone of transformation of montmorillonite to phillipsite (represents zeolites in the model). Unlike the

¹⁰ If Ca was not consumed by the ASR (e.g. because the concrete aggregate is inert or the quartz aggregate has a very low reactive surface area), accumulation of C-S-H at the interface is possible. This scenario is described in Appendix C, Section C.1.

case analysed in Chapter 3, this transformation is reversed once the pH at the interface drops due to ASR in the concrete. The dissolution of montmorillonite is accompanied by the formation of hydromagnetite and hydrotalcite. The hydromagnetite acts as sink for iron originating from the montmorillonite and hydrotalcite takes up excess magnesium.

Although clogging by C-S-H precipitation is not indicated in any of these cases, the role of the model discretisation (mesh size) on the porosity evolution should be noted (see also the discussion in Appendix D.1). For all these cases there is an initial discontinuity in Ca and Si porewater concentrations on either side of the interface between the concrete and the transition layer, since instantaneous C-S-H precipitation (equilibrium chemical reaction) is assumed, the interface would always clog, if very fine meshes (micrometre) were employed, albeit that the clogged zone would be very thin. Such a thin layer of precipitated material is unlikely to be continuous and thus also unlikely to significantly affect the functionality of the EGTS. Nonetheless, further experimental evidence as well as model calculations may be required to categorically rule out clogging in such situations.

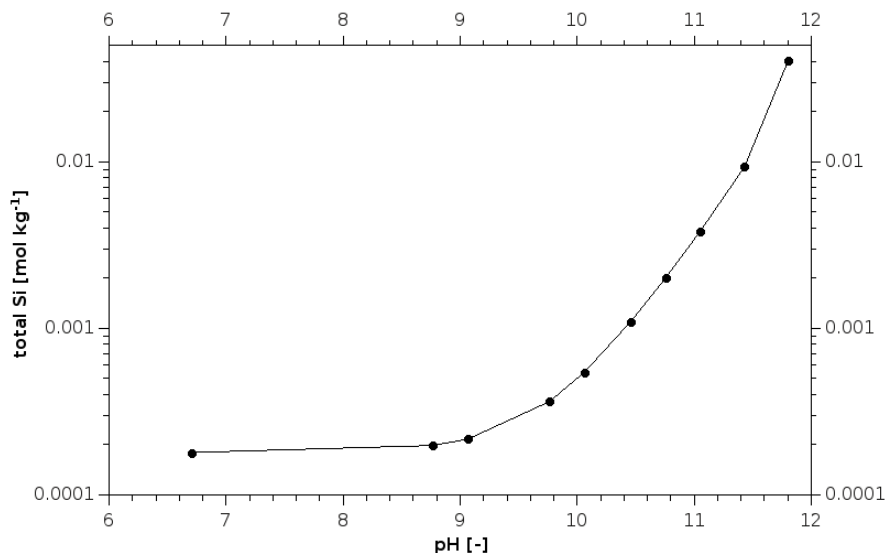


Fig. 4-11: Solubility of SiO_2 (quartz), as indicated by the concentration of total Si in solution, as a function of pH, calculated for a simplified system consisting of 5 200 g quartz, 1000 g water and 1 g NaCl.

pH was changed by adding small amounts of NaOH.

4.3 Main findings of the sensitivity analyses

The 1-D calculations show that the choice of aggregate in concrete might strongly influence the evolution of the EGTS system (Fig. 4-12). A concrete aggregate in form of quartz¹¹ sand will be in thermodynamic disequilibrium with the initial cement minerals. The equilibration of the cement phases with quartz aggregates by ASR is kinetically controlled. These reactions are completed in the models after a few thousand years. After ASR is completed in Cases 1 and 2, concrete is equilibrated with quartz and the pH drops to values close to 10. In addition, the pH in the transition layer and in concrete will equilibrate and differences in the solubility of SiO_2

¹¹ Quartz acts as placeholder also for other forms of reactive SiO_2 .

will be levelled out. At this stage, the geochemical difference between concrete and materials in the transition layer will be small and the long term evolution of the system is then governed by the transport of solutes from the sand/bentonite into the concrete.

The long term evolution of the example EGTS case analysed in Chapter 3 was characterized by dissolution/precipitation fronts that slowly migrated into sand/bentonite and into the concrete. These reactions are driven by the strong geochemical differences between sand/bentonite and (non-degraded) concrete. Model cases in this section show much less pronounced effects, as the geochemical gradients between sand/bentonite and concrete are lowered due to ASR in concrete. Replacement of montmorillonite by zeolites in sand/bentonite is only visible for early times (< 1000 years), i.e. when pH is still high. As soon as pH is lowered due to ASR the transformations is reverted and montmorillonite is re-precipitated. Development of long term dissolution fronts affecting the main constituents of sand/bentonite or concrete are not observed in Cases 1 and 2.

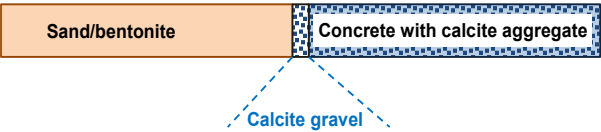
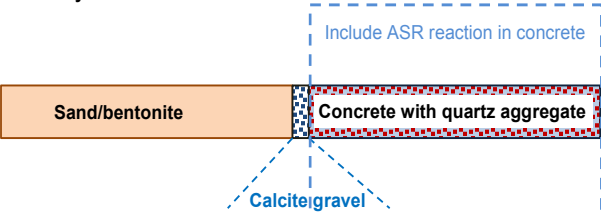
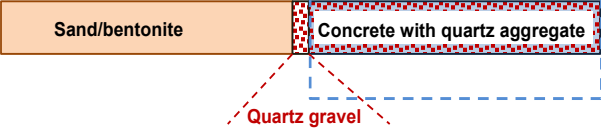
Calculation case	Main observations
<p>Example EGTS case analysed in Ch. 3:</p> 	<p>No porosity blocking at interfaces. Montmorillonite alteration front migrates a short distance into sand/bentonite, typically a few metres in 100000 years. Alteration fronts in the concrete progress in a similar way.</p>
<p>Cases analysed in this section:</p> <p>1:</p>  <p>2:</p> 	<p>No porosity blocking at interfaces. "Minor" montmorillonite alteration for times < 1000 years.</p> <p>No porosity blocking at interfaces. "Minor" montmorillonite alteration for times < 1000 years. Pore clogging at concrete/gravel interface cannot be excluded (uncertainty associated with discretisation).</p>
<p>Case analysed Appendix C, Section C.1:</p> 	<p>Strong porosity reduction (clogging) at interface between concrete and transition layer after ~ 300 years independent of length of quartz gravel compartment (uncertainty in clogging time associated with discretisation)</p>

Fig. 4-12: Overview of the calculation cases analysed in this section and comparison of main observations with other model variants.

Strong reduction of porosity at the interface between the concrete and the transition layer was not observed in Cases 1 and 2, where the ASR occurs in the bulk of the concrete due to the interplay between ASR and distributed precipitation of C-S-H in the transition layer (Figs. 4-7 and 4-10). Especially for Case 2, quartz gravel as transition layer material, accumulation of C-S-H in a very fine layer near transition layer/concrete interface at early simulation times cannot be ruled out by modelling studies (compare discussions in Section 4.2 and Appendix D). However for real media with very big pores (e.g. media composed of gravel or stones) it seems questionable if precipitation zones which are much smaller than an average pore size can completely clog the pore space and reduce gas and liquid transport significantly.

As illustrated by further model calculations in Appendix C, ASR causing concrete degradation is in the investigated case probably not influenced by the saturation state, as residual saturation (0.3) in the concrete is assumed to provide enough water to drive the reaction and the availability of water is therefore not a limiting factor. Even under saturated conditions, ASR is a kinetically controlled reaction rather than a reaction driven by macroscopic transport.

5 Conclusions

The engineered gas transport system (EGTS) is an example of a measure to limit gas pressures in a L/ILW repository and in the emplacement rooms for long-lived intermediate level waste in a high-level waste repository, allowing the release of gas while limiting the advective transport of dissolved radionuclides through the repository access tunnel system, as well as ensuring retention of many safety-relevant radionuclides by sorption.

This report has assessed the long-term evolution of the EGTS with a view to determining whether these design functions can be provided over the required 100 000 year time frame. The focus is on mineralogical evolution and the potential for pore clogging. It is shown by qualitative reasoning and quantitative illustrative analyses that, for an appropriately chosen EGTS design, such clogging is not expected to occur, even if the system is assumed to be fully saturated at all times. Furthermore, in the parts of the EGTS that remain mostly unsaturated, transport in the liquid phase will be very small and this restricts further mineral reactions that cause porosity changes.

The most favourable design options are those that minimise chemical gradients across the transition layer, through the choice of transition layer material and length. Materials that are in direct contact with concrete materials should not be in thermodynamic disequilibrium in order to avoid any detrimental porosity changes associated with the alkali-silica reaction or with carbonation driven by diffusion across the material interface. In particular, the choice of limestone (with calcite as the key mineral) as a filling material for the transition layer is an attractive option, since bentonite, cement and Opalinus Clay all contain this mineral, and are in thermodynamic equilibrium with it. By contrast, a fill material that dissolves easily in contact with a high pH solution (e.g. quartz or other more reactive variants of SiO_2) might foster clogging near interfaces.

Montmorillonite dissolution is predicted to occur in the sand/bentonite. However, the migration of the montmorillonite dissolution front is limited to just a few metres over 100 000 years and thus only a small part of the access tunnel system (backfilled with sand/bentonite) is affected, which would have no significant detrimental effect on overall radionuclide retention properties of the repository barrier system.

Sensitivity analyses show that precipitation of C-S-H minerals at the interface between the transition layer and concrete can be suppressed by the use of quartz aggregate in the concrete which leads to the concrete evolving internally by the alkali-silica reaction. The reaction consumes Si and Ca in porewater before it is transported towards the interface. Large amounts of C-S-H precipitation occur, but the precipitates are distributed fairly broadly throughout the concrete, and there are no indications that these could lead to pore clogging. The analyses also show that progress of dissolution fronts in the concrete and in the sand/bentonite depends on the length of the transition layer within the modelled time period, but porosity changes remain small across the range of transition layer lengths considered.

The models discussed in this report are based on the implicit assumption that EGTS materials are surrounded by an Opalinus Clay host rock. Concrete, transition layer and sand/bentonite materials are set up and equilibrated with Opalinus Clay porewater. Other potential host rocks that are under consideration for the L/ILW repository in Switzerland show very similar porewater compositions and model results in Kosakowski & Berner (2013) demonstrate that the effect of geochemical gradients between concrete and clay materials are very similar for these host rocks. Therefore, the model results for the EGTS presented in this report are not expected to change noticeably if slightly different host rock porewaters were to be used, and the conclusions of this report would remain valid.

Overall, qualitative reasoning and quantitative illustrative analyses indicate that, for an appropriately chosen EGTS design, chemical interactions will not lead to a significant reduction in porosity and to a loss of gas permeability, and the EGTS should function as required over a 100 000 year time frame.

6 References

- Bear, J., Bachmat, Y. (1990): Introduction to Modeling of Transport Phenomena in Porous Media. Kluwer Academic Publishers, Dordrecht.
- Benbow, S., Robinson, P., Savage, D. (2002): pH Buffering Capacity in Backfill. SKI Report 02:39, SKI, Stockholm, Sweden.
- Benbow, S., Watson, S., Savage, D., Robinson, P. (2004): Vault-Scale Modelling of pH Buffering Capacity in Crushed Granite Backfills. SKI Report 2004:17, SKI, Stockholm, Sweden.
- Berner, U. (1992): Evolution of pore water chemistry during degradation of cement in a radioactive waste repository environment. *Waste Manag.* 12, 201-219.
- Berner, U. (2011): Setting up bentonite pore water compositions. PSI Internal Report AN-44-10-04 Rev.1. Paul Scherrer Institut, Villigen, Switzerland.
- Berner, U., Kulik, D.A., Kosakowski, G. (2013): Geochemical impact of a low-pH cement liner on the near field of a repository for spent fuel and high-level radioactive waste. *Phys. Chem. Earth, Parts A/B/C* 64, 46-56.
- Bildstein, O., Cochapin, B., Trotignon, L., Steefel, C.I. (2007): Porosity reduction at material interface as a result of water-rock interactions in the context of deep geological waste disposal. *In: Wang, Y., Bullen, T.D. (Eds.), Water Rock Interaction, Proceedings of the 12th International Symposium on Water-Rock Interaction, Kunming, China, 31 July – 5 August 2007.* Taylor & Francis, pp. 571-575.
- De Windt, L. (2004): Coupled modeling of cement/claystone interactions and radionuclide migration. *J. Contam. Hydrol.* 68, 165-182.
- Gaboreau, S., Lerouge, C., Dewonck, S., Linard, Y., Bourbon, X., Fialips, C.I., Mazurier, a., Pret, D., Borschneck, D., Montouillout, V., Gaucher, E.C., Claret, F. (2012): In-situ interaction of cement paste and shotcrete with claystones in a deep disposal context. *Am. J. Sci.* 312, 314-356.
- Gaucher, E.C., Blanc, P. (2006): Cement/clay interactions – a review: experiments, natural analogues, and modeling. *Waste Manag.* 26, 776-788.
- Glasser, F.P., Marchand, J., Samson, E. (2008): Durability of concrete – Degradation phenomena involving detrimental chemical reactions. *Cem. Concr. Res.* 38, 226-246.
- Gray, W.G., Miller, C.T., Schrefler, B.A. (2013): Averaging Theory for Description of Environmental Problems: What Have We Learned? *Adv. Water Resour.* 51, 123-138.
- Hayek, M., Kosakowski, G., Churakov, S. (2011): Exact analytical solutions for a diffusion problem coupled with a precipitation-dissolution reaction and feedback of porosity change. *Water Resour. Res.* 47, W07545.
- Hayek, M., Kosakowski, G., Jakob, A., Churakov, S.V. (2012): A class of analytical solutions for multidimensional multispecies diffusive transport coupled with precipitation-dissolution reactions and porosity changes. *Water Resour. Res.* 48, W03525.

- Hou, X., Strouble, L.J., Kirkpatrick, R. (2004): Formation of ASR gel and the roles of C-S-H and portlandite. *Cem. Concr. Res.* 34, 1683-1696.
- Idiart, A.E. (2009): Coupled analysis of degradation processes in concrete specimens at the meso-level. *Geotech. Eng. Polytechnical University of Catalunya, Barcelona.*
- Idiart, A.E., López, C.M., Carol, I. (2011): Chemo-mechanical analysis of concrete cracking and degradation due to external sulfate attack: A meso-scale model. *Cem. Concr. Compos.* 33, 411-423.
- KEG (2003): Kernenergiegesetz vom 21. März 2003 (KEG) [Nuclear Energy Act]. Systematische Sammlung des Bundesrechts SR 732.1. Switzerland.
- Kolditz, O., Bauer, S., Bilke, L., Böttcher, N., Delfs, J.O., Fischer, T., Görke, U.J., Kalbacher, T., Kosakowski, G., McDermott, C.I., Park, C.H., Radu, F., Rink, K., Shao, H., Shao, H.B., Sun, F., Sun, Y.Y., Singh, A.K., Taron, J., Walther, M., Wang, W., Watanabe, N., Wu, Y., Xie, M., Xu, W., Zehner, B. (2012a): OpenGeoSys: an open-source initiative for numerical simulation of thermo-hydro-mechanical/chemical (THM/C) processes in porous media. *Environ. Earth Sci.* 67, 589-599.
- Kolditz, O., Görke, U.-J., Shao, H., Wang, W. (Eds.) (2012b): *Thermo-Hydro-Mechanical-Chemical Processes in Porous Media.* Springer Berlin Heidelberg, Berlin, Heidelberg.
- Kosakowski, G. (2010): Scoping reactive transport calculations on the geochemical evolution of interfaces between concrete, Opalinus Clay and tunnel backfill materials. PSI Internal Report AN-44-10-03. Paul Scherrer Institut, Villigen, Switzerland.
- Kosakowski, G. (2011): A new OpenGeoSysGEMS reactive transport benchmark for kinetically controlled porosity change PSI Internal Report AN-44-11-20. Paul Scherrer Institut, Villigen, Switzerland.
- Kosakowski, G., Berner, U. (2011): Base data sets and concepts for reactive transport calculations PSI Internal Report AN-44-11-01-Rev1. Paul Scherrer Institut, Villigen, Switzerland.
- Kosakowski, G., Berner, U. (2013): The evolution of clay rock/cement interfaces in a cementitious repository for low- and intermediate level radioactive waste. *Phys. Chem. Earth, Parts A/B/C* 64, 65–86.
- Kosakowski, G., Watanabe, N. (2013): OpenGeoSys-Gem: A numerical tool for calculating geochemical and porosity changes in saturated and partially saturated media. *Phys. Chem. Earth, Parts A/B/C.*
- Kosakowski, G., Berner, U., Wieland, E., Glaus, M.A., Degueldre, C. (2014): Geochemical evolution of the L/ILW near-field. Nagra Technical Report 14-11, Switzerland.
- Kosakowski, G., Blum, P., Kulik, D.A., Pflingsten, W. (2009): Evolution of a generic clay/cement interface: First reactive transport calculations utilizing a Gibbs energy minimization based approach for geochemical calculations. *J. Environ. Sci. Sustain. Soc.* 3, 41-49.

- Kulik, D.A., Wagner, T., Dmytrieva, S.V., Kosakowski, G., Hingerl, F.F., Chudnenko, K.V., Berner, U.R. (2013): GEM-Selektor geochemical modeling package: revised algorithm and GEMS3K numerical kernel for coupled simulation codes. *Comput. Geosci.* 17, 1-24.
- Lindgård, J., Andiç-Çakır, Ö., Fernandes, I., Rønning, T.F., Thomas, M.D.A. (2012): Alkali-silica reactions (ASR): Literature review on parameters influencing laboratory performance testing. *Cem. Concr. Res.* 42, 223-243.
- Lothenbach, B., Wieland, E. (2006): A thermodynamic approach to the hydration of sulphate-resisting Portland cement. *Waste Manag.* 26, 706-19.
- Marty, N.C.M., Tournassat, C., Burnol, A., Giffaut, E., Gaucher, E.C. (2009): Influence of reaction kinetics and mesh refinement on the numerical modelling of concrete/clay interactions. *J. Hydrol.* 364, 58-72.
- Martys, N.S. (1999): Diffusion in partially-saturated porous materials. *Mater. Struct.* 32, 555-562.
- Mualem, Y. (1976): A new model for predicting the hydraulic conductivity of unsaturated porous media. *Water Resour. Res.* 12, 513-522.
- Multon, S., Sellier, A., Cyr, M. (2009a): Chemo-mechanical modeling for prediction of alkali silica reaction (ASR) expansion. *Cem. Concr. Res.* 39, 490-500.
- Multon, S., Sellier, A., Cyr, M. (2009b): Cement and Concrete Research Chemo – mechanical modeling for prediction of alkali silica reaction (ASR) expansion. *Cem. Concr. Res.* 39, 490-500.
- Nagra (2008a): Entsorgungsprogramm 2008 der Entsorgungspflichtigen. Nagra Technical Report NTB 08-01. Nagra, Wettingen, Switzerland.
- Nagra (2008b): Vorschlag geologischer Standortgebiete für das SMA- und das HAA-Lager. Darlegung der Anforderungen, des Vorgehens und der Ergebnisse. Nagra Technical Report 08-03. Nagra, Wettingen, Switzerland.
- Nagra (2008c): Effects of post-disposal gas generation in a repository for low- and intermediate-level waste sited in the Opalinus Clay of Northern Switzerland. Nagra Technical Report NTB 08-07. Nagra, Wettingen, Switzerland.
- Nagra (2008d): Vorschlag geologischer Standortgebiete für das SMA- und das HAA-Lager. Begründung der Abfallzuteilung, der Barrierensysteme und der Anforderung an die Geologie: Bericht zur Sicherheit und Machbarkeit. Nagra Technical Report NTB 08-05. Nagra, Wettingen, Switzerland.
- Palandri, J.L., Kharaka, Y.K. (2004): A compilation of rate parameters of water-mineral interaction kinetics for application to geochemical modeling. Open File Report 2004-1068. U.S. Geological Survey, Menlo Park, California.
- Papafotiou, A., Senger, R. (2014): Sensitivity analyses of gas release from a L/ILW repository in the Opalinus Clay in the candidate siting regions of Northern Switzerland. Nagra Working Report NAB 13-92. Nagra, Wettingen, Switzerland.

- Peterson, K., Gress, D., Van Dam, T., Sutter, L. (2006): Crystallized alkali-silica gel in concrete from the late 1890s. *Cem. Concr. Res.* 36, 1523-1532.
- Revil, A., Jougnot, D. (2008): Diffusion of ions in unsaturated porous materials. *J. Colloid Interface Sci.* 319, 226-35.
- Savage, D. (2009): Forge (D3.1-R): A review of experimental evidence for the development and properties of cement-bentonite interfaces with implications for gas transport. Nagra Working Report NAB 09-30. Nagra, Wettingen, Switzerland.
- Savage, D., Walker, C., Benbow, S. (2010): An analysis of potential changes to barrier components due to interaction with a concrete liner in a repository for SF/HLW in Opalinus Clay. Nagra Working Report NAB 10-17. Nagra, Wettingen, Switzerland.
- Savoie, S., Page, J., Puente, C., Imbert, C., Coelho, D. (2010): New experimental approach for studying diffusion through an intact and unsaturated medium: a case study with Callovo-Oxfordian argillite. *Environ. Sci. Technol.* 44, 3698-704.
- Senger, R.K., Ewing, J. (2009): Gas-L/ILW: Gas pressure buildup and transport in a deep geologic L/ILW repository in Opalinus Clay using large-scale and local-scale models. Nagra Working Report NAB 09-17. Nagra, Wettingen, Switzerland.
- Shao, H., Dmytrieva, S. V, Kolditz, O., Kulik, D.A., Pflingsten, W., Kosakowski, G. (2009): Modeling reactive transport in non-ideal aqueous – solid solution system. *Appl. Geochemistry* 24, 1287-1300.
- Shao, H., Kosakowski, G., Berner, U., Kulik, D.A., Mäder, U., Kolditz, O. (2013): Reactive transport modeling of the clogging process at Maqarin natural analogue site. *Phys. Chem. Earth, Parts A/B/C* 64, 21-31.
- Smellie, J.A.T. (1998): MAQARIN natural analogue study: Phase III. SKB Technical Report TR-98-04, Volume II. SKB, Stockholm, Sweden.
- Steeffel, C., Lichtner, P. (1998): Multicomponent reactive transport in discrete fractures – II: Infiltration of hyperalkaline groundwater at Maqarin, Jordan, a natural analogue site. *J. Hydrol.* 209, 200-224.
- Tartakovsky, A.M., Redden, G., Lichtner, P.C., Scheibe, T.D., Meakin, P. (2008): Mixing-induced precipitation: Experimental study and multiscale numerical analysis. *Water Resour. Res.* 44, 1-19.
- Taylor, H.F.W. (1997): *Cement Chemistry*, 2nd ed. Edition Thomas Telford, London, UK.
- Traber, D., Mäder, U. (2006): Reactive transport modelling of the diffusive interaction between Opalinus Clay and concrete. Nagra Working Report NAB 05-06. Nagra, Wettingen, Switzerland.
- Tremosa, J., Arcos, D., Matray, J.M., Bensenouci, F., Gaucher, E.C., Tournassat, C., Hadi, J. (2012): Geochemical characterization and modelling of the Toarcian/Domerian porewater at the Tournemire underground research laboratory. *Appl. Geochemistry* 27(7), 1417-1431.

- Trotignon, L., Peycelon, H., Bourbon, X. (2006): Comparison of performance of concrete barriers in a clayey geological medium. *Phys. Chem. Earth, Parts A/B/C* 31, 610-617.
- Trotignon, L., Thouvenot, P., Munier, I., Cochapin, B. (2011): Numerical Simulation of Atmospheric Carbonation of Concrete Components in a Deep Geological Radwaste Disposal Site During Operating Period. *Nucl. Technol.* 174, 424-437.
- Trotignon, L., Devallois, V., Peycelon, H., Tiffreau, C., Bourbon, X. (2007): Predicting the long term durability of concrete engineered barriers in a geological repository for radioactive waste. *Phys. Chem. Earth, Parts A/B/C* 32, 259-274.
- Trotignon, L., Didot, A., Bildstein, O., Lagneau, V., Margerit, Y. (2005): Design of a 2-D cementation experiment in porous medium using numerical simulation. *Oil & Gas Sci. Technol.* 60, 307-318.
- Van Genuchten, M.T. (1980): A Closed-form Equation for Predicting the Hydraulic Conductivity of Unsaturated Soils. *Soil Sci. Soc. Am. J.* 44, 892-898.
- Wang, W., Kosakowski, G., Kolditz, O. (2009): A parallel finite element scheme for thermohydro-mechanical (THM) coupled problems in porous media. *Comput. Geosci.* 35, 1631-1641.
- Wang, W., Rutqvist, J., Görke, U.-J., Birkholzer, J.T., Kolditz, O. (2010): Non-isothermal flow in low permeable porous media: a comparison of Richards' and two-phase flow approaches. *Environ. Earth Sci.* 62, 1197-1207.
- Wang, W., Zehner, B., Böttcher, N., Görke, U.J., Kolditz, O. (2013): Parallel numerical modeling of two-phase flow process in porous medium. *Comput. Geosci.* *submitted*.
- Winter, N.B. (2009): *Understanding Cement: An introduction to cement production, cement hydration and deleterious processes in concrete.* WHD Microanalysis Consultants, Woodbridge, UK.
- Xu, P., Yu, B. (2008): Developing a new form of permeability and Kozeny – Carman constant for homogeneous porous media by means of fractal geometry. *Adv. Water Resour.* 31, 74-81.

Appendix A: Details of Numerical Models

A.1 Governing equations for flow and transport

Several different equations for solving single- and multi-phase flow problems are implemented in OpenGeoSys (Kolditz et al. 2012a). For the description of single phase liquid flow in partially saturated porous media the Richards flow equation is implemented in OpenGeoSys to (Wang et al. 2010):

$$\phi \rho_f \frac{\partial S}{\partial p_c} \frac{\partial p_c}{\partial t} + \nabla \cdot \left(\rho_f \frac{k_{rel} \mathbf{k}}{\mu_f} (\nabla p_f - \rho_f \mathbf{g}) \right) = Q_f \quad (\text{A-1})$$

With porosity ϕ [-], liquid density ρ_f [kg/m³], saturation S [-], capillary pressure $p_c = -p_f$, liquid pressure p_f [Pa], time t [s], gravitational acceleration vector \mathbf{g} [m s⁻²], relative permeability k_{rel} [-], intrinsic permeability vector \mathbf{k} [m²], liquid viscosity μ_f [Pa s], and source term Q_f [kg/s].

Different relations between capillary pressure and saturation are implemented in OpenGeoSys. We use the following formulation after Mualem (1976) and Van Genuchten (1980):

$$p_c = \frac{\rho_f \mathbf{g}}{\alpha} \left(S_e^{-1/m} - 1 \right)^{(1-m)} \quad (\text{A-2})$$

with $m = 1 - (1/n)$ where n is a dimensionless pore size distribution index and α [1/m] the van Genuchten parameter, which is related to the gas entry pressure. The effective saturation S_e is:

$$S_e = \frac{S - S_r}{S_{max} - S_r}, \quad (\text{A-3})$$

where S_{max} and S_r are the maximum and residual saturation, respectively.

The relative permeability k_{rel} for the liquid phase is related to the effective saturation S_e by:

$$k_{rel} = S_e^{0.5} \cdot \left[1 - \left(1 - S_e^m \right)^m \right]^2. \quad (\text{A-4})$$

The capillary pressure–saturation and the permeability–saturation relations are empirical relations that depend on the pore size distribution and the shape of the pores in a specific medium. These relations are normally determined experimentally, or have to be obtained by upscaling procedures (see e.g. Gray et al. 2013; Tremosa et al. 2012).

In the coupled code, the transport of dissolved chemical species is described by the commonly used advection-dispersion (-diffusion) equation (ADE) (Bear & Bachmat 1990) which is supplemented by source/sink terms originating from chemical reactions:

$$\begin{aligned}\frac{\partial SC_i}{\partial t} &= \nabla(S\mathbf{v}C_i) + \nabla(\mathbf{S}\mathbf{D}_i\nabla C_i) + Q_i \\ \frac{\partial SC_i}{\partial t} &= \Gamma_i(C_1, \dots, C_m)\end{aligned}\quad (\text{A-5})$$

C_i [mol m⁻³] stands for the molar concentration of species i , \mathbf{v} [m/s] for the pore velocity in the liquid phase, \mathbf{D}_i [m²/s] for the dispersion tensor of species i , Q_i [mol/m/s] for a source/sink term and $\Gamma_i(C_1, \dots, C_m)$ [mol m/s] is a source/sink term for species i due to chemical reactions with m other species. The Scheidegger dispersion tensor is implemented in two dimensions as:

$$\mathbf{D}_{kl} = \alpha_T |\mathbf{v}| \delta_{kl} + (\alpha_L - \alpha_T) \frac{\mathbf{v}_k \mathbf{v}_l}{|\mathbf{v}|} + D_e \quad (\text{A-6})$$

where α_L [m] and α_T [m] are the longitudinal and transversal dispersion length, respectively. δ_{kl} [-] is the Kronecker symbol, $v_{k,l}$ [m/s] is the liquid pore velocity in direction k,l and D_e [m²/s] is the effective diffusion coefficient. In our implementation the effective diffusion coefficient is calculated based on an Archie relation with exponent b and a pore diffusion coefficient D_p [m²/s]:

$$D_e = (\phi \cdot S_e)^b \cdot D_p \quad (\text{A-7})$$

A.2 Coupling to the chemical system and evaluation of porosity changes

The chemical system is solved with the numerical kernel GEMS3K of the GEM-Selektor package (Kulik et al. 2013). The overall coupling employs the sequential non-iterative coupling scheme as described in Shao et al. (2009). After solving the flow equation (1) and several transport equations (5), GEM-Selektor calculates the thermodynamic equilibrium of the system at each FE node taking into account the changed solute concentrations. In contrast to law of mass action (LMA) based chemical solvers, GEMS3K does not work with (solid and solute) concentrations. GEMS3K uses a Gibbs Energy Minimisation (GEM) algorithm and requires as input the absolute amount of all independent components (base species). From this it calculates the complete liquid/gas/solid phase composition. Liquid saturation and solute concentration changes are therefore first transformed into appropriate changes of the independent components. After the new solution is provided by GEMS3K, the new liquid phase composition in terms of solute concentrations is passed to the OpenGeoSys transport solver. Eventual changes of porosity due to precipitation/dissolution of mineral phases are calculated and the porosity in the OpenGeoSys part is updated. In addition, changes in the volume of the liquid phase are back-coupled to the flow equation for the next time step via source-sink terms.

Coupling between OpenGeoSys and GEMS3K is realised by a central coupling loop for each calculated model domain. These loops are parallelised using a multi-threading technique. At least one and up to several dozens of worker threads are spawned for each domain, each one containing its own GEMS3K instance to solve geochemical systems in parallel. Synchronisation

between the threads is carried out using barrier commands. The total number of threads should match the number of available computing nodes. Test calculations on different hardware show that for certain types of applications tremendous speedups are possible compared to the serial version.

A.3 Material and thermodynamic setup and initial porewater compositions

The thermodynamic setup of the system, the composition of the materials and the resulting initial porewater compositions are summarised in Kosakowski and Berner (2011) and repeated in Tab. A-1 and A-2, respectively. In addition, Appendix D provides the base thermodynamic dataset for the 1-D and 2-D models, respectively.

Tab. A-1: Material composition from Kosakowski & Berner (2011) in terms of mass fractions for 1-D calculations.

Mass fraction	Sand/bentonite 80/20	Transition layer		Concrete	
		(quartz)	(calcite)	(quartz aggregate)	(calcite aggregate)
liquid	1.06E-01	1.41E-01	1.41E-01	8.93E-02	8.78E-02
gas					
quartz ¹	7.33E-01	8.57E-01	1.89E-04	7.31E-01	2.36E-03
C-S-H ²				9.42E-02	9.26E-02
portlandite				4.50E-02	4.42E-02
monocarbonate ²				1.99E-02	1.95E-02
ettringite ²				1.59E-02	1.56E-02
hydrotalcite ²				3.39E-03	3.34E-03
calcite	1.19E-03	2.83E-07	8.57E-01	1.50E-03	7.34E-01
strontianite				3.12E-04	3.06E-04
hydro-magnetite	3.76E-04	8.44E-05	8.44E-05	3.70E-05	3.64E-05
barite	8.49E-04	1.02E-07	1.01E-07	4.14E-06	4.07E-06
siderite	1.25E-03	1.08E-04	1.08E-04		
pyrite	5.05E-04	9.38E-05	9.37E-05		
gypsum	1.13E-04				
montmorillonite	1.58E-01	1.89E-03	1.89E-03		
dolomite		6.65E-06	7.07E-06		
Further material properties					
porosity	0.23	0.3	0.3	0.2	0.2

¹ The quartz phase includes some small amount of an inert material that represents minerals currently not considered in our setup (e.g. feldspars).

² These mineral phases are represented by solid solutions in the setup.

Tab. A-2: Initial porewater composition for sand/bentonite, sand/gravel and concrete (Kosakowski & Berner 2011).

Dissolved component [mol/m ³]	Sand/bentonite 80/20	Transition layer		Concrete	
		(quartz)	(calcite)	(quartz aggregate)	(calcite aggregate)
Al	2.27E-05	2.09E-05	2.09E-05	3.26E-03	3.26E-03
Ba	8.67E-05	1.27E-04	1.27E-04	7.67E-05	7.67E-05
C	1.36E+01	7.82E-01	7.82E-01	1.05E-02	1.05E-02
Ca	1.62E+02	1.15E+01	1.15E+01	1.16E+01	1.16E+01
Cl	1.62E+02	1.59E+02	1.59E+02	2.42E-01	2.42E-01
Fe	5.39E-02	4.70E-02	4.70E-02	4.98E-06	4.98E-06
H	8.30E-01	7.48E-01	7.48E-01	8.05E-01	8.05E-01
K	1.35E+00	2.37E+00	2.37E+00	2.19E-02	2.19E-02
Mg	6.85E+00	8.85E+00	8.85E+00	1.71E-02	1.71E-02
Na	2.38E+02	1.66E+02	1.66E+02	3.36E+01	3.36E+01
O	2.40E+02	1.02E+02	1.02E+02	1.26E+02	1.26E+02
S	5.92E+01	2.47E+01	2.47E+01	2.80E+01	2.80E+01
Si	1.81E-01	1.81E-01	1.81E-01	7.49E-01	7.49E-01
Sr	9.28E-02	2.06E-01	2.06E-01	1.01E-01	1.01E-01
Further porewater properties					
pH	7.73	7.72	7.72	13.1	13.1
pe	-3.34	-3.38	-3.38	-8.98	-8.98
P(CO ₂)	-3.17	-3.2	-3.2	-13.13	-13.13
Ionic strength	0.3	0.23	0.23	0.17	0.17

Tab. A-1 gives the material composition in terms of mass fractions for the liquid-saturated material. As described in the main text, two variants of the transition layer fill were used in the calculations (quartz and calcite) and two variants of the concrete aggregate (again, quartz and calcite). The amounts for both materials were calculated such that the volume fractions of gravel and aggregates remain the same. Mass fractions in material composition differ due to the different mineral densities of quartz and calcite.

The mineral composition and the porewater chemistry of a **CEM I 52.5 N HTS hydrated cement** described by (Lothenbach & Wieland 2006) are used as a starting point for the concrete compartment. The setup is based on the most recent CEMDATA07 thermodynamic database, which includes several ideal solid solutions for hydrated cement minerals consistent with the Nagra/PSI thermodynamic databases 01/1 and 12/07. The concrete setup is described in detail in (Kosakowski & Berner 2013). The original concrete setup includes an inert aggregate, which was replaced by reactive quartz and calcite aggregates. Note that quartz is not in thermodynamic equilibrium with cement phases in the concrete setup. Quartz is therefore treated as an inert phase during equilibration of initial compositions.

For the sand/bentonite setup, 1173.18 g of pre-saturated bentonite from Berner (2011) is used which corresponds to 1000.6 g of dry bentonite. The bentonite is mixed with 4000 g of quartz. After adding 610 g of Opalinus Clay porewater the (total) volumetric water content of the mixture is 0.3. Details of the water balance and cation exchange capacity for this setup are given in Tab. A-3. The porosity (volumetric amount of free water) is then ~ 0.23 as some of the water is bound as interlayer and surface water to the montmorillonite phase (Berner 2011).

Tab. A-3: Water balance, cation exchange capacity (CEC) and porosity of sand/bentonite mixture (Kosakowski & Berner 2011).

	Water phase	Interlayer water	Surface water	Sum
Mole	33.39	9.61		
Mass (gram)	6.02E+02	1.73E+02	8.04E-01	7.75E+02
Volume fraction (phase)	2.29E-01	6.55E-02	2.96E-04	2.95E-01
CEC (meq/kg dry rock)	1.51E+02			
Water content	0.295			
Porosity	0.229			

For the transition layer compartment containing quartz, 848 g of quartz and 60.3 g of inert material are mixed with 149 g of Opalinus Clay porewater. The inert material represents minerals phases that are assumed not to be reactive and is used to scale the porosity to the desired value. In order to mimic impurities in the material, 2 g of montmorillonite and 0.1 g of siderite, hydro-magnetite and pyrite are added. After equilibration the porewater is very similar to the porewater of the sand/bentonite mixture (Tab. A-2). In the case of the transition layer containing calcite, the quartz was replaced by 908 g of calcite in order to mimic a limestone. As for concrete, replacement of quartz by calcite does not change the porewater chemistry.

The dataset for the 2-D calculations extends the dataset for the 1-D model by inclusion of more zeolite phases and an illite solid-solution to mimic cation exchange (Shao et al. 2013). The initial materials (concrete, sand/bentonite and sand/gravel) do not contain the additional minerals and therefore their composition and equilibrated porewater compositions are identical for both datasets.

A.4 Implementation of kinetic control

Implementation of kinetic equations in GEM-Selektor is under development, but it is already possible to pass meta-stability constraints for each species to GEMS3K. The kinetic rate equation is then solved in the OpenGeoSys part of the coupled code and used to constrain the amount of mineral phases for the next time step. A benchmark case with clogging process has been simulated by OpenGeoSys and verified against analytical solution (Hayek et al. 2012, 2011).

An overview on the problems and uncertainties related to precipitation data is given by Palandri & Kharaka (2004) (see pages 5 and 6 of that report). Their approach assumes that both dissolution and precipitation (forward and backward rates) proceed by a single reversible mechanism. In the literature, kinetic rate laws that describe dissolution and precipitation of minerals are often given in a form similar to:

$$\frac{dm}{dt} = SA * k * (a_{H^+})^n * (1 - \Omega^p)^q, \quad (\text{A-8})$$

where dm/dt [mol/s] is the reaction rate in terms of change of mole amount dm per time dt . SA is the mineral reactive surface area [m^2], k is the rate constant [$\text{mol}/m^2/s$], a_{H^+} is the activity of H^+ ions [-], and n, p, q , are constants [-].

Ω is the mineral saturation index [-]:

$$\Omega = \frac{Q}{K}, \quad (\text{A-9})$$

where Q stands for the activity quotient and K is the equilibrium constant for the reaction of interest. Ω is dimensionless and has a value of 1 for equilibrium, less than 1 if the reactants are undersaturated (dissolution of products) and more than 1 if the reactants are oversaturated (precipitation of products).

Palandri & Kharaka (2004) map the majority of their data onto equation 3, in which they differentiate between reactions in pure H_2O (neutral pH) and those catalysed by H^+ (acid) and OH^- (base):

$$\frac{dm}{dt} = -SA \left[\begin{array}{l} k_{acid}^{298.15K} \exp\left(\frac{-E_{acid}}{R} \left(\frac{1}{T} - \frac{1}{298.15K}\right)\right) a_{H^+}^{n_1} (1 - \Omega^{p_1})^{q_1} \\ + k_{neutral}^{298.15K} \exp\left(\frac{-E_{neutral}}{R} \left(\frac{1}{T} - \frac{1}{298.15K}\right)\right) (1 - \Omega^{p_2})^{q_2} \\ + k_{base}^{298.15K} \exp\left(\frac{-E_{base}}{R} \left(\frac{1}{T} - \frac{1}{298.15K}\right)\right) a_{H^+}^{n_3} (1 - \Omega^{p_3})^{q_3} \end{array} \right]. \quad (\text{A-10})$$

T is the absolute temperature [K], and R the molar gas constant ($R = 8.31451070 \text{ J/K/mol}$). E_{acid} , $E_{neutral}$ and E_{base} are (mineral specific) activation energies [J/mol].

It should be noted that the third term of Equation A-10 does not include the activity of OH^- ions, but instead is based on H^+ activity with a negative value for the order of the reaction rate.

For some minerals the reaction rate is not only described in terms of the activity of H^+ , also other mechanisms may contribute. For such cases the activity of H^+ is replaced by the product of reaction activities where the n^i represent the reaction order with respect to species i :

$$\prod a_i^{n^i} . \quad (A-11)$$

Inserting Equation A-10 into Equation A-11, the rates can be calculated in a quite general way:

$$\frac{dm}{dt} = -SA \left[\begin{aligned} & k_{acid}^{298.15K} \exp\left(\frac{-E_{acid}}{R} \left(\frac{1}{T} - \frac{1}{298.15K}\right)\right) \prod a_i^{n^i_1} (1-Q^{p_1})^{q_1} \\ & + k_{neutral}^{298.15K} \exp\left(\frac{-E_{neutral}}{R} \left(\frac{1}{T} - \frac{1}{298.15K}\right)\right) \prod a_i^{n^i_2} (1-Q^{p_2})^{q_2} \\ & + k_{base}^{298.15K} \exp\left(\frac{-E_{base}}{R} \left(\frac{1}{T} - \frac{1}{298.15K}\right)\right) \prod a_i^{n^i_3} (1-Q^{p_3})^{q_3} \end{aligned} \right] . \quad (A-12)$$

The above equation was implemented in OpenGeoSys-GEM and corresponding constraints on the masses of dependent components are passed to the GEMS3K kernel. In contrast to Equation A-10, the second term in Equation A-12 is multiplied with the product of reaction activities. Setting the reaction order to 0 ("zero") allows to remove the dependency on reaction activities from single terms.

Equation A-12 is a very general implementation of a rate law. By setting appropriate parameter values, it is easily possible to mimic other (simpler) rate laws.

In this study only a very simple model for the calculation of the reactive surface area SA for a mineral i is used:

$$SA = V_i a_i \quad (A-13)$$

Where V_i is the volume of the mineral [m^3] and a_i is the relative surface area per volume [m^2/m^3].

Kinetic parameters used in the 1-D calculations are given in Appendix B.

Appendix B: Additional Parameter Values

B.1 Flow and transport parameters

The governing equations for flow and transport in a partially saturated porous medium are presented in Section A.1. The system analysed in the 1-D calculations is assumed to be fully saturated (saturation of unity throughout the model domain). The same pore diffusion coefficient of 1.5×10^{-9} m/s is assumed for all migrating species (Berner et al. 2013; Kosakowski & Berner 2013). The effective diffusion coefficient is calculated according to Eq. A-7 of Appendix A.1, using an exponent $b = 2$. Only diffusive transport is considered in this and other 1-D calculations, so that the definition of permeabilities or other hydraulic parameters/boundary conditions is unnecessary.

For the 2-D calculations, parameter values are taken from the TOUGH-2 calculations carried out by Senger & Ewing (2009). OpenGeoSys and TOUGH 2 can both solve multi-phase flow and transport problems with a coupling between a gas and a liquid phase. In both codes, the same flow laws are implemented for liquid flow in partially saturated media (Tab. B-1), but the formulation is different and requires a conversion of the material parameters (Tab. B-2). The OpenGeoSys-GEM version includes only a coupling to the Richards-flow solver, which solves liquid flow in partially saturated media without considering a gas phase. In this solver, the liquid saturation and the liquid movement is controlled by the initial and boundary conditions for the capillary pressure.

Tab. B-1: Comparison of two-phase flow Van Genuchten input parameters (liquid phase only) for OpenGeoSys and TOUGH 2.

For nomenclature see Kolditz et al. (2012a) for OpenGeosys and Nagra (2008c) for TOUGH 2.

OpenGeoSys according to Kolditz et al. (2012a)	TOUGH 2 according to Nagra (2008c) page 46 and Senger & Ewing (2009) page 13
$m = 1-1/n$	n
Capillary pressure	
$* p_c = \frac{P_w g}{\alpha} (S_e^{-1/m} - 1)^{(1-m)}$	$p_c = P_g - p_w = \frac{1}{\alpha} (S_e^{n/(1-n)} - 1)^{(1/n)}$
Permeability-Saturation	
$k_{rel} = S_e^{0.5} \cdot \left[1 - \left(1 - S_e^m \right)^m \right]^2$	$** k_{r,l} = S_e^{0.5} \cdot \left[1 - \left(1 - S_e^{1-n} \right)^{\frac{n-1}{n}} \right]^2$
$S_e = \frac{S - S_r}{S_{max} - S_r}$	$S_e = \frac{S_w - S_{wr}}{1 - S_{gr} - S_{wr}}$

* Here equation 6.3 in Kolditz et al. (2012a) contains a mistake in the exponent of S_e

** Here Senger & Ewing (2009) contains a mistake in the exponent of S_e

Tab. B-2: Conversion of TOUGH 2 input parameters (Senger & Ewing 2009) to OpenGeoSys.

OpenGeoSys	This study	TOUGH 2 (Senger & Ewing 2009; Table 3-1)	
Opalinus Clay		Opalinus Clay	
$\alpha = p^l g / P_0$	5.45×10^{-4}	P_0	1.8×10^7
$m = 1-1/n$	0.4012	n	1.67
S_{res}	0.5	S_{lr}	0.5
$S_{max} = 1-S_{gr}$	0.997	S_{gr}	0.003
Concrete		Mortar1 / Mortar 2	
$\alpha = p^l g / P_0$	2.45	P_0	4.0×10^3
$m = 1-1/n$	0.6	n	2.5
S_{res}	0.3	S_{lr}	0.3
$S_{max} = 1-S_{gr}$	1.0	S_{gr}	0.0
Bentonite/Sand		Tunnel	
$\alpha = p^l g / P_0$	2.45	P_0	4.0×10^3
$m = 1-1/n$	0.6000	n	2.5
S_{res}	0.3	S_{lr}	0.3
$S_{max} = 1-S_{gr}$	1.0000	S_{gr}	0.000
Typical coarse Sand		(not in Table)	
$\alpha = p^l g / P_0$	2.45 (30.0) *	P_0	---
$m = 1-1/n$	0.6667	N	3.0
S_{res}	0.001	S_{lr}	0.001
$S_{max} = 1-S_{gr}$	1.0	S_{gr}	0.0

* The value was set to 2.45, as much higher values gave numerical problems.

Permeabilities for liquid flow depend on the saturation state of the medium. The simulations employ the same relations and the material parameters as were used in Senger & Ewing (2009) except for the transition layer (see Tabs. B-1, B-2 and B-3). In addition permeabilities will change, if porosities change. There exist many semi-empirical formulations that link porosities n and specific surface areas of the solid phase to the permeability K based on the classic Kozeny-Carman relation (see e.g. Xu and Yu 2008). Using the Kozeny-Carman relation in its simplest form and ignore the unknown change of surface area with porosity, a change in permeability can be described with:

$$K = K_0 (\phi / \phi_0)^3 \quad (\text{B-1})$$

K_0 and ϕ_0 are the initial permeability and the initial porosity, respectively.

For diffusive transport the diffusion coefficient is often linked to the porosity via Archie's relationship. For the simulations the following form was used:

$$D_e = D_p (S \cdot \phi)^n \quad (\text{B-2})$$

D_p is the pore diffusion coefficient which was set to 1.5×10^{-9} m²/s, S the saturation and n the porosity. One should note that the exponent is set to a value of 1, which is a good value for unconsolidated porous media (like gravel) and the very porous concrete backfill, but will overestimate diffusion coefficients in the sand/bentonite compartment.

Tab. B-3: Transport parameters for the 2-D calculations.

Parameter	Sand (quartz) / bentonite 80/20	Transition layer	Concrete
Porosity ϕ	0.23	0.3	0.2
Permeability k	$1.0 \cdot 10^{-16}$	$1.0 \cdot 10^{-12}$	$1.0 \cdot 10^{-12}$
α	2.45	2.45	2.45
m	0.6	0.6667	0.6
S_r	0.3	0.001	0.3
S_{max}	1.0	1.0	1.0

B.2 Kinetic parameters for 1-D calculations

Tab. B-4: Kinetic parameters used in 1-D calculations. Mineral phases not listed were not kinetically controlled.

Mineral phase	k_{acid}	$k_{neutral}$	k_{base}	q_1	p_1	q_2	p_2	q_3	p_3	*	n_1	n_2	n_3	a_i
Kaolinite ¹	-11.31	-13.18	-17.05	1.0	1.0	1.0	1.0	1.0	1.0	H ⁺	0.777	0.0	-0.472	3.0×10 ⁶
Sand/Quartz ²	0.0	-13.99	-16.29	0.0	1.0	1.0	1.0	1.0	1.0	H ⁺	0.0	0.0	-0.5	2143.0
Gravel/Quartz ²	0.0	-13.99	-16.29	0.0	1.0	0.0	1.0	1.0	1.0	H ⁺	0.0	0.0	-0.5	120.0
Gibbsite ¹	-7.65	-11.50	-16.65	1.0	1.0	1.0	1.0	1.0	1.0	H ⁺	0.992	0.0	-0.784	1.0×10 ²
Montmorillonite ¹	-10.98	-12.78	-16.52	1.0	1.0	1.0	1.0	1.0	1.0	H ⁺	0.340	0.0	-0.400	3.0×10 ⁶
Kaolinite ¹	-10.98	-12.78	-16.52	1.0	1.0	1.0	1.0	1.0	1.0	H ⁺	0.340	0.0	-0.400	3.0×10 ⁶
Illite ¹	-10.98	-12.78	-16.52	1.0	1.0	1.0	1.0	1.0	1.0	H ⁺	0.340	0.0	-0.400	3.0×10 ⁶
Phillipsite ³	0.0	-10.00	0.0	0.0	1.0	1.0	1.0	0.0	1.0	H ⁺	0.0	0.0	0.0	1.0×10 ²
Pyrite ³	0.0	-4.55	0.0	0.0	1.0	1.0	1.0	0.0	1.0	O ₂ @	0.0	0.5	0.0	1.0×10 ²
Calcite ³	0.0	-5.81	0.0	0.0	1.0	1.0	1.0	0.0	1.0	H ⁺	0.0	0.0	0.0	6.0×10 ³
Dolomite(ord) ³	0.0	-8.6	0.0	0.0	1.0	1.0	1.0	0.0	1.0	H ⁺	0.0	0.0	0.0	1.0×10 ³

* Species for which activity products in Equation A-12 are included.

¹ According to Palandri & Kharaka (2004); a_i taken from Traber & Mäder (2006).

² According to quartz from Palandri & Kharaka (2004); a_i corresponds to spherical particles of 0.0028 m diameter for sand and 0.05 m for gravel.

³ According to Traber & Mäder (2006).

B.3 Kinetic parameters for 2-D calculations

Tab. B-5: Kinetic parameters used in 2-D calculations. Mineral phases not listed were not kinetically controlled.

Mineral phase	k_{acid}	$k_{neutral}$	k_{base}	q_1	p_1	q_2	p_2	q_3	p_3	*	n_1	n_2	n_3	a_i
Kaolinite ¹	-11.31	-13.18	-17.05	1.0	1.0	1.0	1.0	1.0	1.0	H ⁺	0.777	0.0	-0.472	3.0×10 ⁶
Sand/quartz ²	0.0	-13.99	-16.29	0.0	1.0	1.0	1.0	1.0	1.0	H ⁺	0.0	0.0	-0.5	2143.
Gravel/quartz ²	0.0	-13.99	-16.29	0.0	1.0	0.0	1.0	1.0	1.0	H ⁺	0.0	0.0	-0.5	120.0
Gibbsite ¹	-7.65	-11.50	-16.65	1.0	1.0	1.0	1.0	1.0	1.0	H ⁺	0.992	0.0	-0.784	1.0×10 ²
Montmorillonite ¹	-10.98	-12.78	-16.52	1.0	1.0	1.0	1.0	1.0	1.0	H ⁺	0.340	0.0	-0.400	3.0×10 ⁶
Illite ¹	-10.98	-12.78	-16.52	1.0	1.0	1.0	1.0	1.0	1.0	H ⁺	0.340	0.0	-0.400	3.0×10 ⁶
Phillipsite ³	0.0	-10.00	0.0	0.0	1.0	1.0	1.0	0.0	1.0	H ⁺	0.0	0.0	0.0	1.0×10 ²
Analcime ³	0.0	-10.00	0.0	0.0	1.0	1.0	1.0	0.0	1.0	H ⁺	0.0	0.0	0.0	1.0×10 ²
Mordenite ³	0.0	-10.00	0.0	0.0	1.0	1.0	1.0	0.0	1.0	H ⁺	0.0	0.0	0.0	1.0×10 ²
Laumontite ³	0.0	-10.00	0.0	0.0	1.0	1.0	1.0	0.0	1.0	H ⁺	0.0	0.0	0.0	1.0×10 ²

* Species for which activity products in Equation A-12 are included.

¹ According to Palandri & Kharaka (2004); a_i taken from Traber and Mäder (2006).

² According to quartz from Palandri & Kharaka (2004); a_i corresponds to spherical particles of 0.0028 m diameter for sand and 0.05 m for gravel.

³ According to Traber & Mäder (2006).

Appendix C: Additional Calculation Cases

C.1 1-D modelling of the case with a hypothetical inert concrete aggregate

In this section, we consider a simplified case for diffusive transport in a fully liquid saturated EGTS in which quartz sand is used to fill the transition layer. In addition, for this simplified case, the same cement model as in Kosakowski & Berner (2013) was used. One feature of this cement model is the representation of concrete aggregate as inert (non-reactive) material.

Dissolution/precipitation of the quartz sand is assumed to be kinetically controlled with the pH-dependent law from Palandri & Kharaka (2004) and a specific reactive surface area of 10 000 m²/m³ for a typical sand with effective diameter of 0.6 mm (Tab. C-1). Equilibrium chemistry is assumed for all other mineral reactions.

Tab. C-1: Kinetic parameters as used in the 1-D diffusive calculations that explore the influence of transition layer length.

Mineral phases not listed were not kinetically controlled. According to Palandri & Kharaka (2004): a_i arbitrary value corresponds to spherical particles of 0.6 mm diameter ("Mittelsand – Feinsand").

Mineral phase	k_{acid}	$k_{neutral}$	k_{base}	q_1	p_1	q_2	p_2	q_3	p_3	*	n_1	n_2	n_3	a_i
Sand	0.0	-13.99	-16.29	0.0	1.0	0.0	1.0	1.0	1.0	H ⁺	0.0	0.0	-0.5	1.0·10 ⁴

* Species for which activity products in Equation A-12 are included.

Fig. C-1 shows the calculated mineralogical profile across the EGTS transition layer and the adjoining regions for the case where calcite aggregate in the concrete is replaced by a hypothetical inert material and, in addition, the calcite gravel in the transition layer is replaced by quartz gravel. The transition layer is 5 m long in this case, although similar behaviour at the interfaces was observed for 1 m, 5 m, 10 m and 20 m long transition layers. The figure illustrates that a decrease in porosity at the interface between the concrete and the transition layer causes pore clogging at 300 years. Further evolution of mineralogy and porosity is considerably slower at later times, since mass flux over the interface is reduced by orders of magnitude. The actual clogging time depends on the model discretisation at the material interface (see Appendix D.1), finer discretisation results in earlier clogging, coarser discretisation causes later clogging.

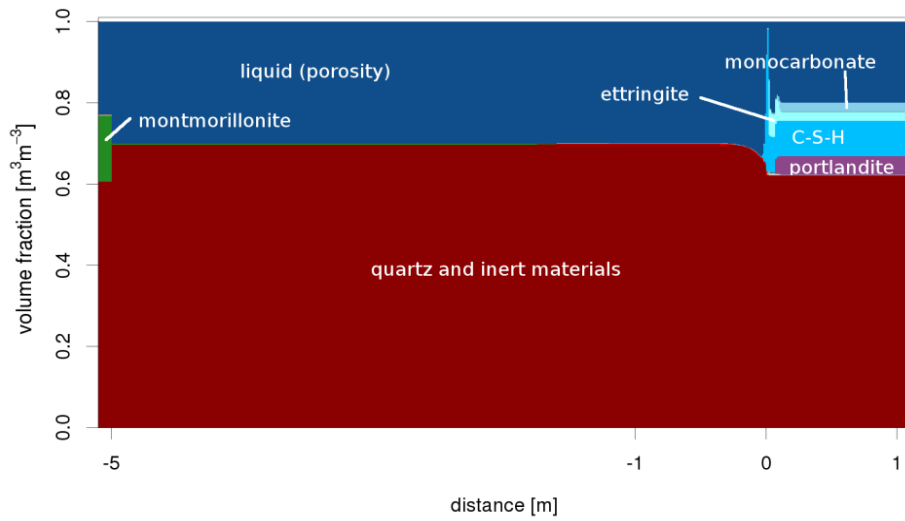


Fig. C-1: Mineralogical profile at 300 years within a 5 m long transition layer composed of quartz gravel and the adjoining regions in a case where calcite aggregate in the concrete is replaced by an inert material.

C.2 2-D modelling of the case with quartz-filled transition layer and quartz aggregate

In this section, we consider again the case analysed in Chapter 4 where the transition layer is composed of quartz gravel and the concrete aggregate also consists of quartz sand and analyse it using the 2-D model (1-D results are shown in Figs. 4-3 and 4-4). The initial mineralogy profile along the bottom of the model is shown in Fig. C-2. The exact initial mineral and porewater compositions of the materials are the same as for the corresponding 1-D case and given in Tab. A-1. Major minerals present are montmorillonite and quartz sand in the bentonite/sand compartment, quartz gravel in the transition layer, and quartz sand, portlandite, C-S-H, ettringite and monocarbonate in the concrete.

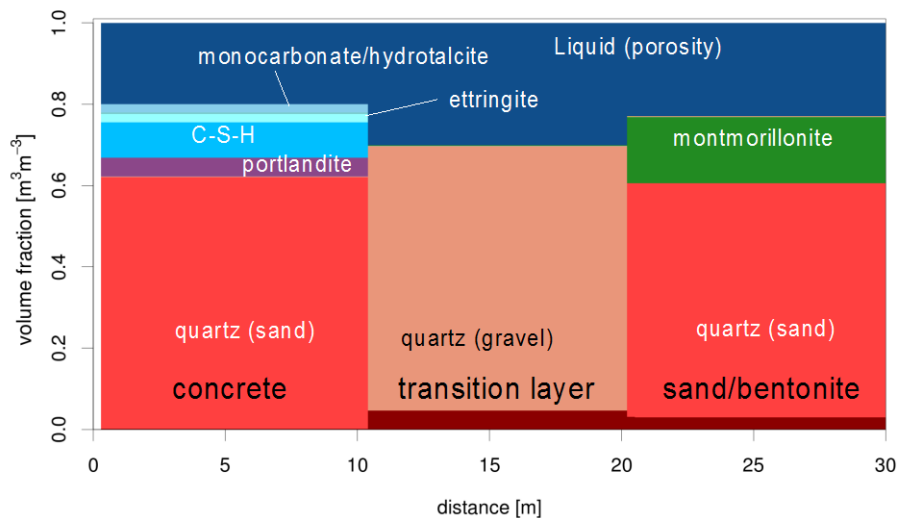


Fig. C-2: Initial mineralogy profile along the bottom of the model.

Other features of the 2-D model set up used for calculations up to 1000 years is essentially the same as that used in Section 3.3. Firstly, the same water inflow from the access tunnel system is considered as in Section 3.3. For longer-term calculation, a coarser finite-element discretisation is used. Afterwards, an increase in the inflow rate by a factor of 10 is considered.

C.2.1 Porewater chemistry and mineralogy after 1000 years

Consider first Cl and Na in the porewater. Initially, the Cl and Na concentrations in concrete are low, but high in the transition layer and in sand/bentonite. Fig. C-3 shows the distributions of dissolved Cl and Na after 1000 years. The thermodynamic setup of the model is such that Cl does not participate in any mineral reaction and may thus be used as a conservative tracer. Porewater with higher Cl concentration flows along the bottom of the system (from right to left in the figure) into the concrete. In addition, diffusive transport is strongest in regions with high (residual) saturation, especially the concrete. There is no decrease of Cl concentration in the transition layer, as diffusive fluxes are much lower there than in the concrete.

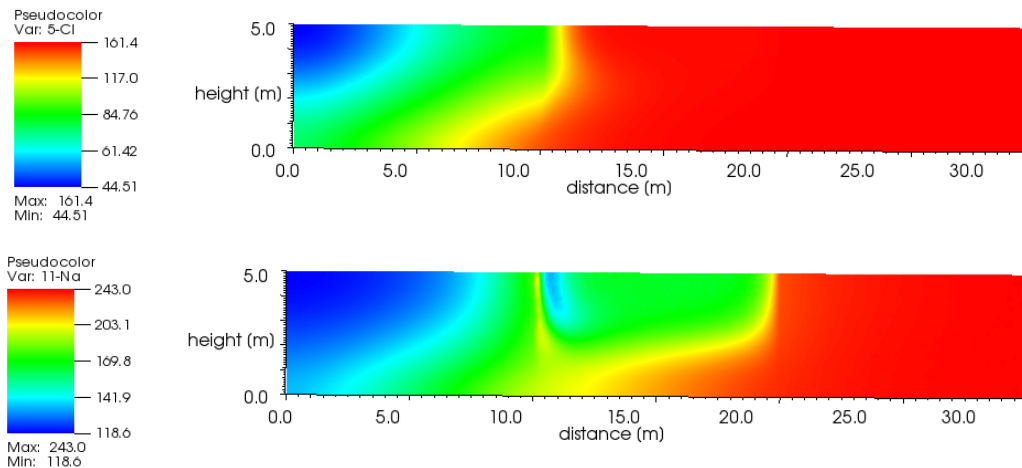


Fig. C-3: Concentrations [mol/m^3] of total dissolved Na (bottom) and Cl (top) in the porewater after 1000 years.

Na is involved in some mineral forming reactions for zeolites and clays and undergoes cation exchange reactions in such minerals. Results in a somewhat different concentration evolution compared with Cl. In the transition layer – at low saturations (upper part) – the Na concentration is strongly reduced due to its incorporation in trace amounts of zeolites or clays. Precipitation of these minerals is strongest near to the interface with concrete and hence Na concentration is lowest. At the bottom of the concrete and at the bottom of the transition layer, advective transport dominates. A sodium front therefore progresses into the concrete. In the concrete itself, a diffusion front into upper parts of the domain is visible.

Fig. C-4 shows the distributions of dissolved C and Ca after 1000 years. The concentration of C in the porewater at this time is mainly governed by the pH dependence of carbonate (calcite) solubility (Fig. 3-6). pH is much higher in the concrete than in the sand/bentonite. Concrete acts as a sink for C caused by carbonation reactions, so C concentrations are low in concrete. The much higher C concentrations in the sand/bentonite and the transition layer are caused by equilibria with minor amounts of carbonates. If these buffers are exhausted, very small changes in mineralogy in areas where the water content is low may cause significant changes in

C concentration. At the interface between the concrete and the transition layer, diffusive exchange causes mineral reactions that result in a strong concentration change. At low saturation (upper part of the figure), the concentration change occurs very close to the interface. At the bottom of the domain, where saturation is close to one, diffusive fluxes are larger and cause a displacement of the concentration jump.

Total Ca concentrations in porewater are, in addition, influenced by portlandite dissolution and compositional changes (C-S-H precipitation) due to reaction with reactive SiO_2 (ASR). In the model, the dissolution of quartz sand and quartz gravel are controlled by relatively slow reaction kinetics. Ca concentrations therefore increase in the concrete compartment. At the interface between concrete and the transition layer, Ca concentrations are high when C is low and vice versa. This is caused by the carbonation of concrete, where Ca is consumed to form carbonate.

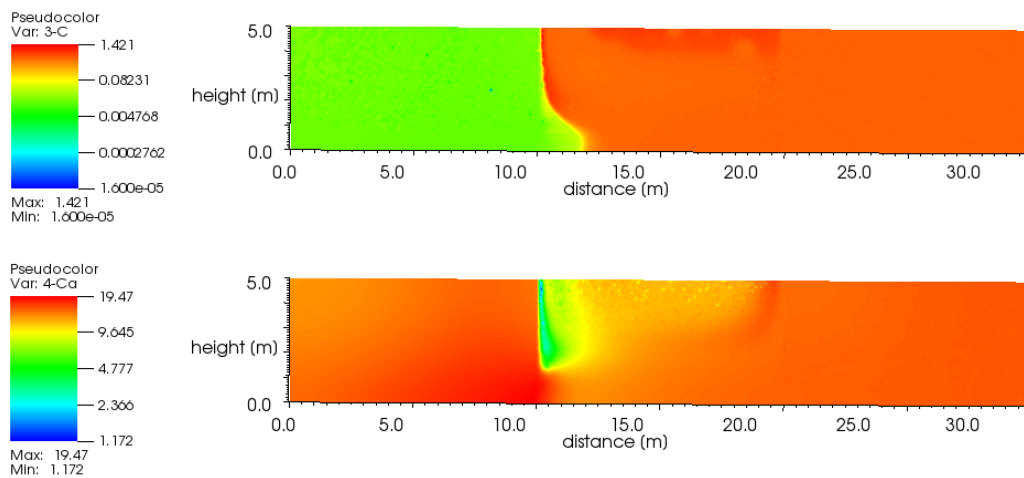


Fig. C-4: Concentrations [mol/m^3] of total dissolved Ca (bottom) and C (top) in the porewater after 1000 years.

Si concentrations after 1000 years are shown in Fig. C-5. Low values are found in areas of neutral pH (see Fig. C-6), namely the sand/bentonite compartment and the transition layer, with higher values present in concrete. The interface between the concrete and the transition layer shows highest Si concentrations due to production of Si rich C-S-H.

pH evolution is shown in Fig. C-6. The pH in concrete is high initially, with near neutral conditions in the transition layer and in the sand/bentonite. With time, two overlapping processes are apparent: diffusion of hydroxide ions (high pH) into the saturated part of the transition layer and a pH drop in the concrete due to the ASR. The pH front moves against the direction of flow into the transition layer, as flow velocities are low and diffusive transport dominates over short distances and concentration gradients are high. In the concrete, the pH is set by equilibria with cement minerals. The ASR causes a degradation of the concrete, by transforming cement minerals successively into C-S-H phases, carbonates, zeolites and finally clay minerals.

Fig. C-7 shows three mineralogical profiles (bottom, middle and top of the domain) after 1000 years of system evolution. Full water saturation is present only for the profile at the bottom of the domain. The sand/bentonite and most of the transition layer show any major mineralogical changes at this time. In concrete, on the other hand, reaction with the quartz aggregate (ASR) causes concrete degradation. The mineralogical evolution at the bottom of the domain is very similar to the case calculated with the 1-D model discussed in Chapter 4 (see Fig. 4-5), although the slightly more refined chemical setup used in the 2-D model, which considers more zeolite minerals than the 1-D model, results in the precipitation of laumontite and mordenite after 1000 years, which replaces the phillipsite found in the 1-D model after the same time. One should note that zeolite precipitation is minimal and the produced quantities are hardly visible in Fig. C-7.

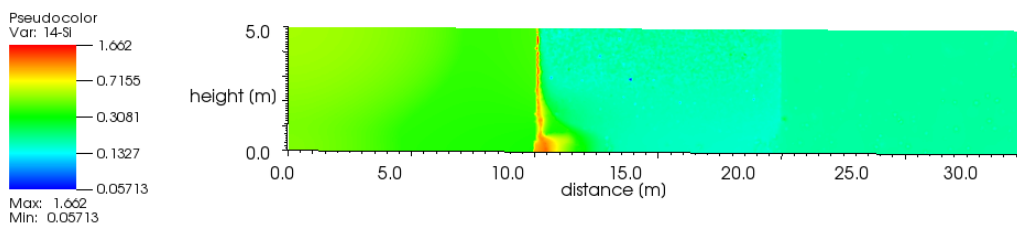


Fig. C-5: Concentrations [mol/m³] of total dissolved Si in the porewater after 1000 years.

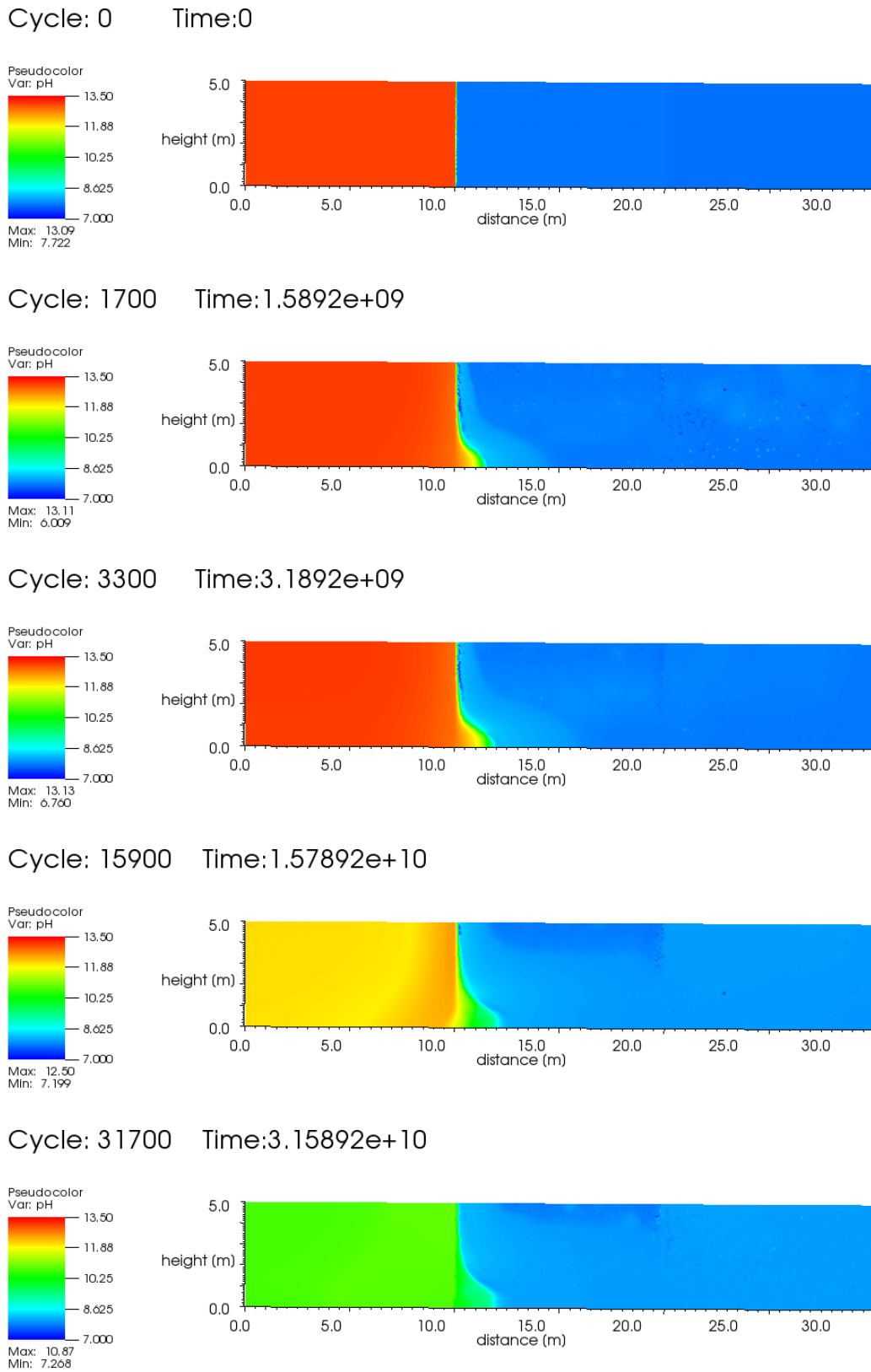


Fig. C-6: Initial pH, and pH evolution at 50 years, 100 years, 500 years and 1000 years (from top to bottom).

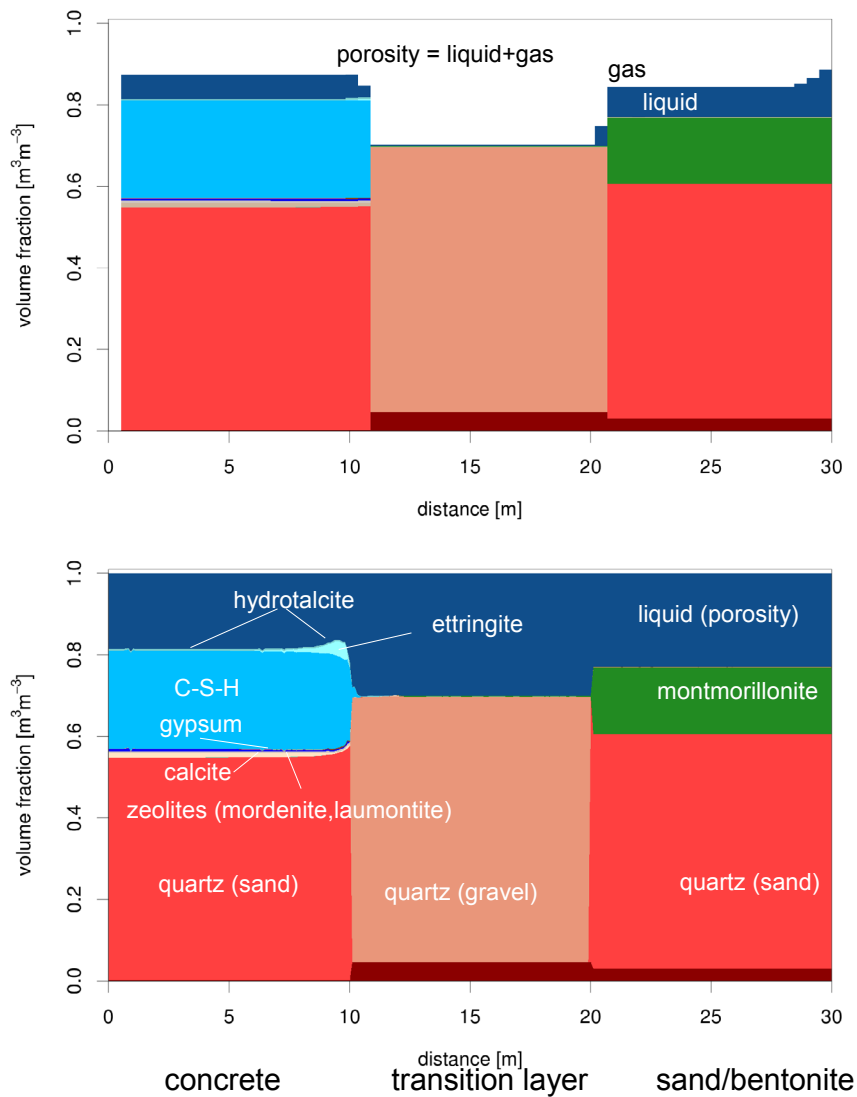


Fig. C-7: Mineralogical profiles after 1000 years (from bottom to top) at the bottom of the model and at the top of the model (height 5 m).

Fig. C-8 shows the porosity distribution at 1000 years. The mineralogical changes cause a porosity change near the interface between the concrete and the transition layer: the dark blue colours show a zone with reduced porosity near the interface. The extension of the zone and the degree of change is highest in the fully saturated zones and decreases with height.

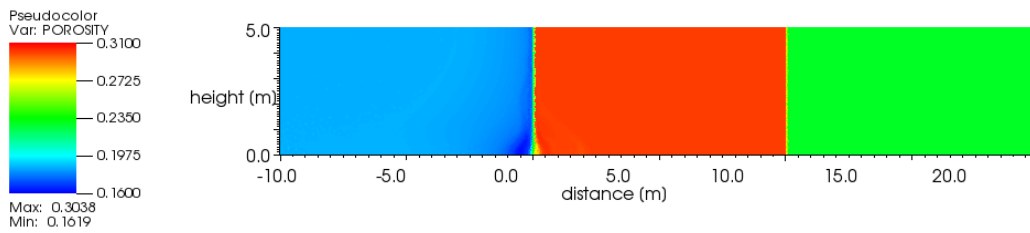


Fig. C-8: Porosity distribution after 1000 years.

The porosity profiles along the bottom, middle and top of the model are shown in Fig. C-9. The porosity profile along the bottom of the model shows no significant porosity changes in the transition layer and the sand/bentonite compartment compared with the initial state. In the concrete, the porosity is homogeneously reduced due to ASR in which some cement minerals are replaced mainly by less-dense C-S-H phases. In addition, redistribution of ettringite towards the interfaces causes an additional porosity decrease. The broad distribution of the porosity decrease at the bottom of the domain indicates that it is not caused by localised precipitation driven by diffusive or advective transport alone. Ettringite formation is not only controlled by the in-diffusion of sulphate, but also by the availability of Al from dissolution of Al-bearing minerals. The kinetically controlled dissolution of a mineral phase(s) in combination with the competitive formation of other Al-bearing mineral phases restricts the formation of ettringite, which allows transport processes to disperse solutes and distribute precipitation over a larger region.

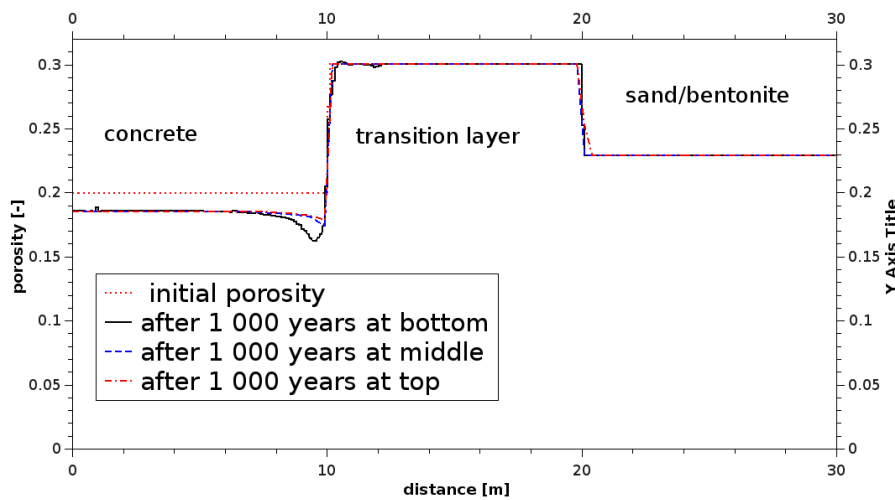


Fig. C-9: Porosity profiles along the bottom (height = 0 m), the middle (height = 2.5 m) and the top (height = 5 m) of the model at 1000 years.

C.2.2 Longer-term evolution

Evaluation of the long term performance up to 100 000 years with the mesh used for calculations in Section C.2.1 exceeds currently available computing resources. The utilized OpenGeoSys-GEM code is parallelized, but speedup of calculations by utilising more CPUs is problem size dependent. Good speedup for solution of flow and transport equations is achieved for about 1000 unknowns (FE nodes) per CPU. For smaller number of unknowns the parallel solvers might need more time. In chemical calculations for each FE node one chemical system has to be equilibrated. Experience shows, that between 10 and 100 chemical systems have to be solved per CPU in order to get a good load balance. For the 2-D model with 20 000 FE nodes typically not more than 200 CPUs (20 for transport and flow equation, rest for GEMS3K threads) can be used before calculation time levels off or increases. In addition, due to the operator splitting approach used for coupling OpenGeoSys and GEMS3K, discretisation dependent limitations on the possible time step size occur. Typically fine meshes need many time steps and coarse meshes fewer.

Due to these limitations to reach long simulation times, we set up a mesh with coarser discretisation. The average node distance was increased from 0.1 m (fine mesh) to 0.5 m (coarse mesh) which decreased the node number to 679 and the elements to 1224. Such a model can be run easily on a work station in 1 – 3 days up to 100 000 years.

The dependence of model results on discretisation is discussed in Appendix D.1. We tested the influence of discretisation for this model setup by comparing results at 1000 years, when the main effects induced by ASR are completed and reaction fronts in concrete to ingress of host rock porewaters develop. A comparison of the mineralogical profiles at 1000 years for models with fine and coarse mesh shows a good qualitative and reasonable quantitative agreement of mineralogical changes (Fig. C-10). Corresponding porosity profiles along the bottom of the model at 1000 years are shown in Fig. C-11. The coarse scale model averages out the consequences of the evolving reaction fronts, but this is not critical, as long as porosity changes (which are back coupled to transport parameters) are not very strong. As soon as reaction fronts move more than 1 – 3 node distances (of the coarse mesh), results between fine mesh and coarse mesh models will be in good agreement.

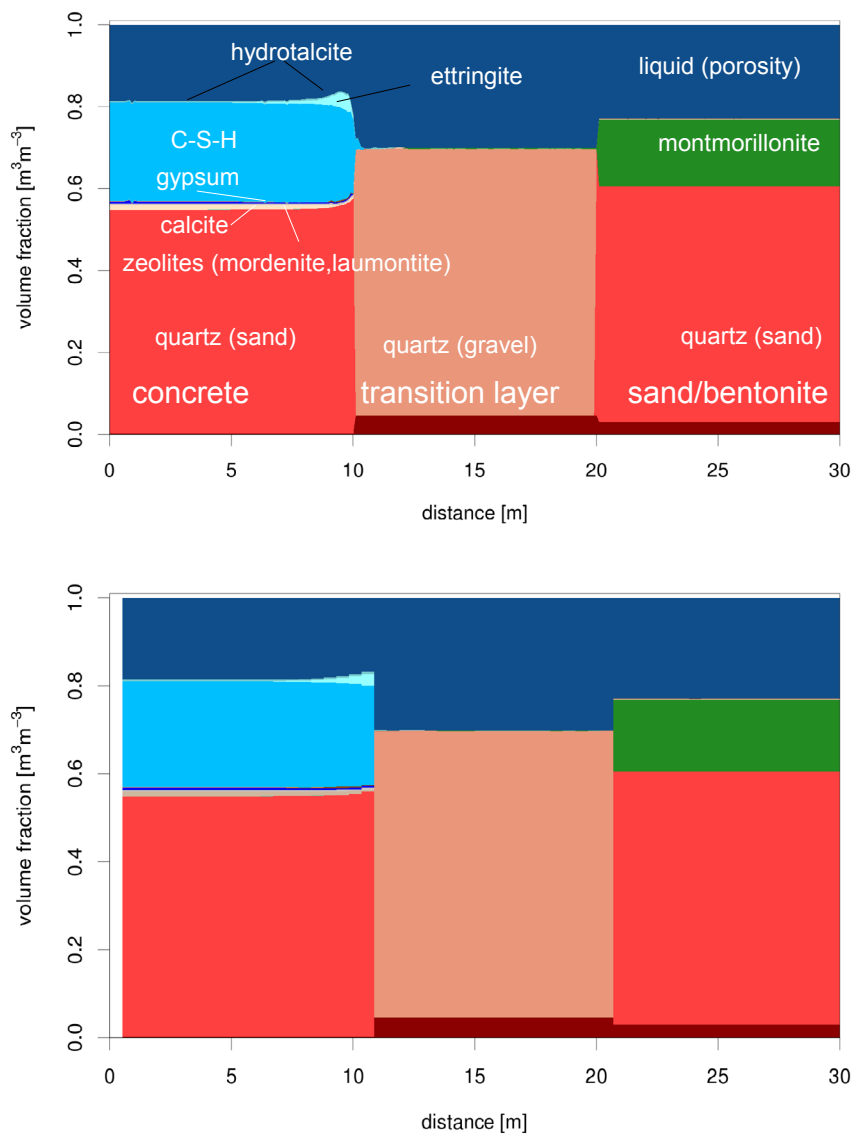


Fig. C-10: Porosity profiles along the bottom (height = 0 m) of the model with fine mesh (top: average node distance 0.1 m) and with coarse mesh (bottom: average node distance 0.5 m) after 1000 years simulation time.

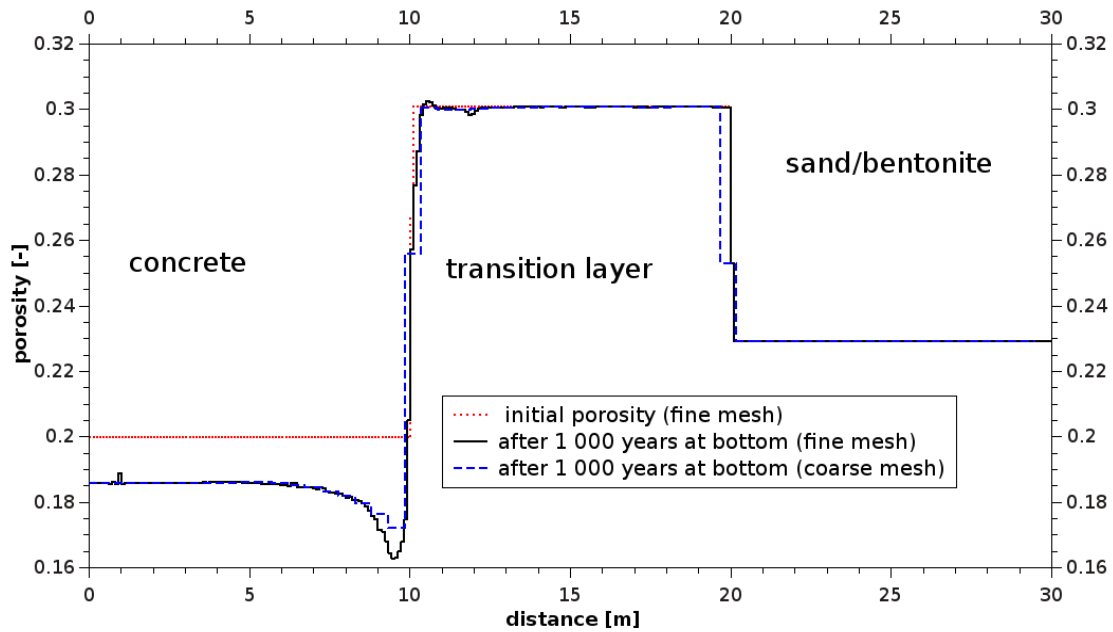


Fig. C-11: Porosity profiles along the bottom (height = 0 m) of the model variants with different discretisation at 1000 years (coarse mesh: average node distance 0.5 m, fine mesh: average node distance 0.1 m).

Fig. C-12 shows mineralogical profiles along the bottom and top of the model domain after 100 000 years (as noted in Section 3.3, a coarser discretisation is used for such longer-term simulations). At the bottom of the model domain, continuing steady-state water flow causes steady leaching of the concrete. Up to a distance of 5 m into the concrete from its interface with the transition layer, C-S-H continues to dissolve and increasing amounts of hydrotalcite are visible. Sulphur-containing cement phases are completely dissolved and a gypsum precipitation front moves into the concrete domain. The gypsum peak is about 3 m from the interface with the transition layer. Towards the interface, the gypsum is replaced by brucite, calcite and SiO_2 . The unsaturated top part of the model domain does not show these mineralogical transformations, as advective transport and diffusive transport in the liquid phase is only minimal. There are also no significant mineralogical changes visible at the interface between the transition layer and the sand/bentonite. There is no geochemical disequilibrium between the materials on either side of this interface and the diffusive transport of cement porewater species towards the sand/bentonite is effectively suppressed by the desaturation of the transition layer and the advective liquid flow in opposite direction at the base of the model.

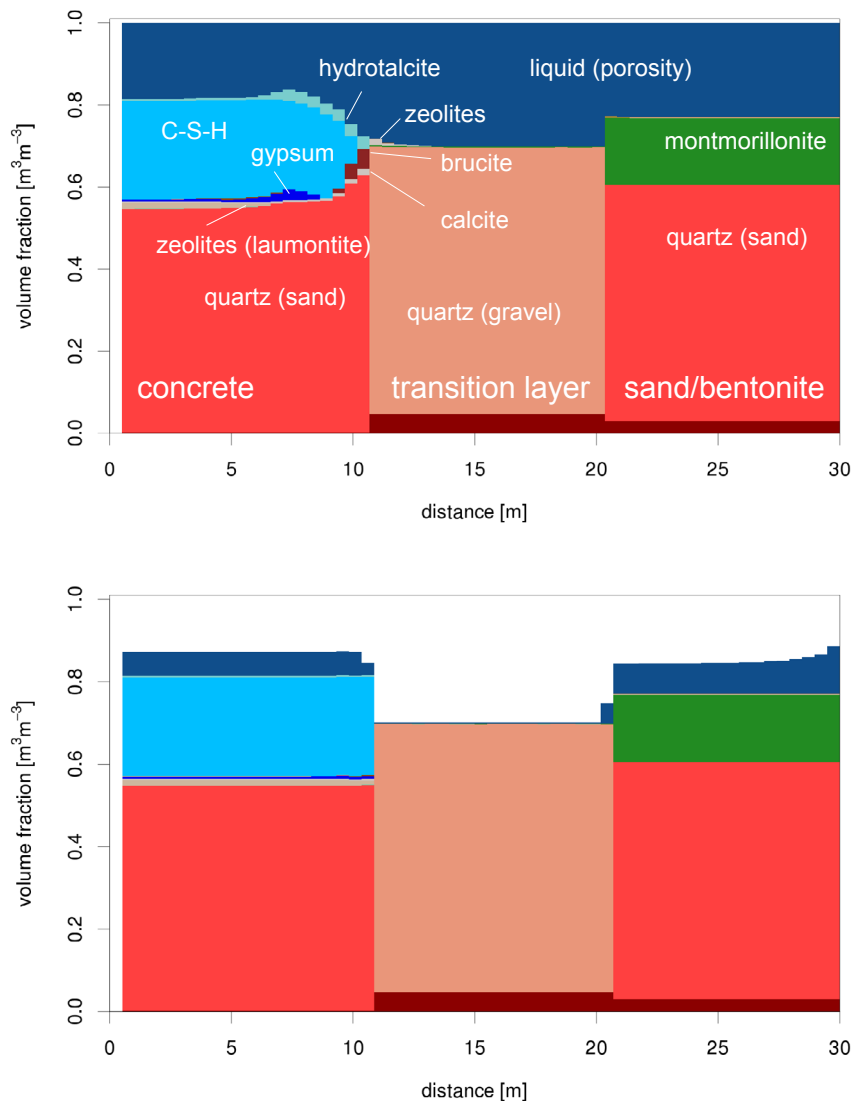


Fig. C-12: Mineralogical profiles along the bottom (top) and the top (bottom) of the model domain after 100 000 years simulation time for the 2-D case with a coarse discretisation.

The mineralogical changes are also reflected in the spatial distribution of porosity in Fig. C-13. A quarter-circular zone with porosity reduction in the bottom part of concrete domain is connected to gypsum precipitation. Gypsum precipitation is not strong enough to reduce porosity significantly. Inside the quarter-circular zone, the porosity increases as gypsum and C-S-H are dissolved by the inflow of sand/bentonite porewater.

The calculated pH after 100 000 years is close to 10.2 in the concrete, close to 7.8 in the sand/bentonite and between 6.7 and 8 in the transition layer (Fig. C-14). In the concrete, pH is buffered by the presence of C-S-H (and hydrotalcite). The lowered pH at individual nodes in the upper part of the gravel domain is a numerical artefact related to the low liquid/rock ratio in combination with relatively small changes in the composition of clay and iron phases. The numerical model needs a connected residual water phase in all domains. In the transition layer, the residual water content is set to an arbitrary non-zero value in order to allow the hydraulic solver to find a solution. For such low water content, the calculation of porewater composition

is highly affected by small inconsistencies in the thermodynamic setup and by numerical artefacts from transport and geochemical solvers. As transport in liquid phase is very small, such inaccuracies in porewater composition will not affect neighbouring regions with higher water contents.

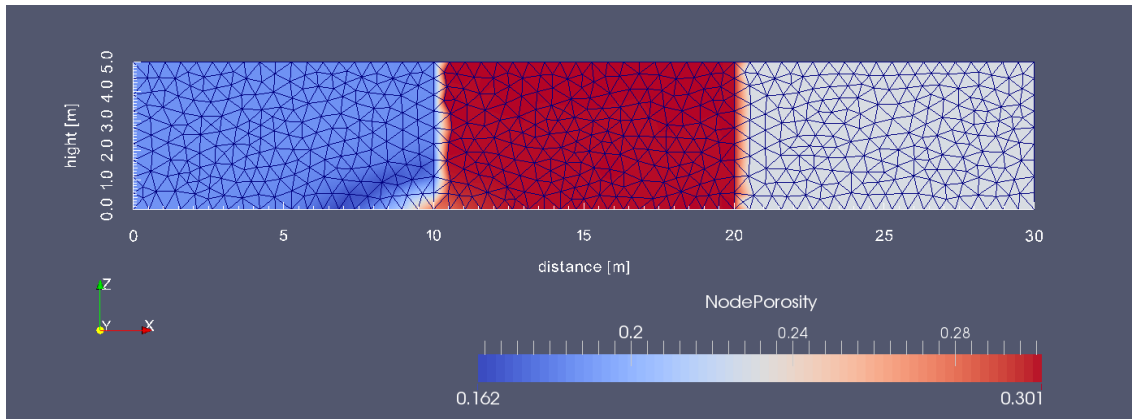


Fig. C-13: Porosity (at FE nodes) after 100 000 years.

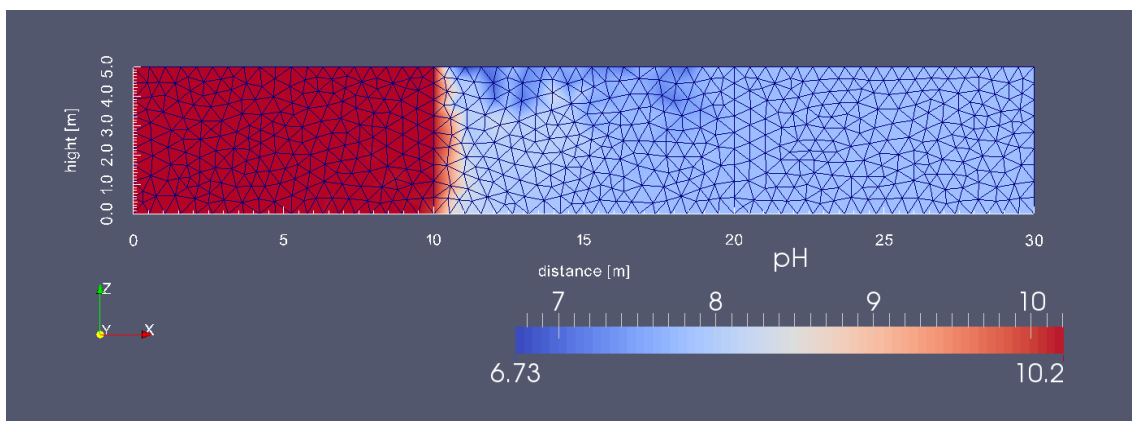


Fig. C-14: pH (at FE nodes) after 100 000 years.

C.2.3 Increased inflow from the access tunnel system

The 2-D model (with the coarse mesh) was also run with a ten-fold increase in the assumed inflow rate from the access tunnel system. The resulting evolution of saturation is similar to that for the lower flow rate. In particular, the saturation states in the transition layer and concrete compartments are the same as for the lower inflow rate and the bentonite-sand compartment is again almost fully saturated.

The mineralogical evolution in the fully saturated bottom part of the model is largely controlled by the advective transport of clay porewater towards the concrete (Fig. C-15). After 100 000 years, the extent of concrete degradation due to ingress of clay porewater is much more pronounced than for the lower inflow rate, as can be seen by comparing this figure with Fig. C-12. At the bottom of the model domain, where liquid fluxes are strongest, C-S-H and

gypsum are completely dissolved up to a distance of 7 m from the concrete/gravel interface. Up to this distance, brucite is precipitated, which is replaced near the interface mainly by calcite, as well as some clay minerals (montmorillonite).

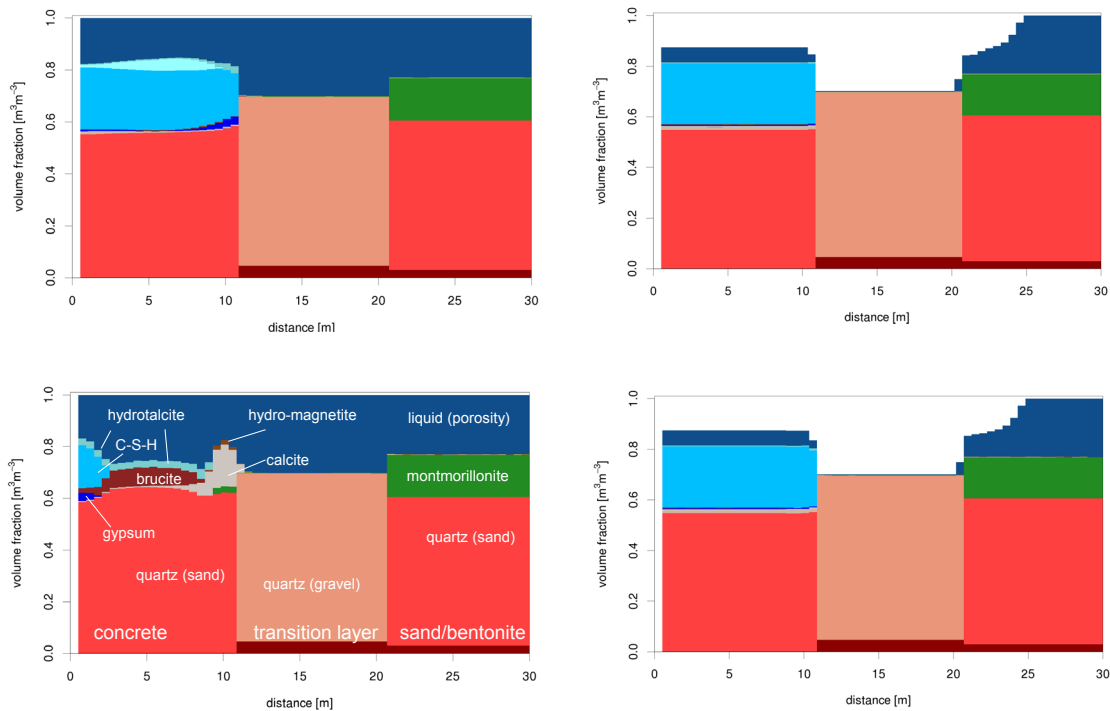


Fig. C-15: Mineralogical profiles after 1000 years (upper row) 100 000 years (lower row) from the 2-D model with a coarse discretisation and ten-fold increase in porewater inflow from the access tunnel system.

Profiles for the bottom of the model are in the left column and at the top of the model in the right column.

Fig. C-16 shows the spatial distribution of brucite, gypsum and calcite. Comparison with the spatial water saturation map, which is in concrete identical to the lower-inflow cases (see Section 3.3.3 and Fig. 3-10), shows that the mineral alteration fronts are driven laterally by the fast advective transport in the fully saturated bottom part of the model domain. In the vertical direction, progress is much less and related to the slow diffusion of solutes towards the partially saturated top of the model. The spatial map of porosity in the lower right of Fig. C-16 follows the precipitation pattern. Zones with low density and high volume minerals (e.g. gypsum, C-S-H) tend to have lower porosity, whereas zones with enhanced dissolution of minerals have increased porosity. At the bottom of the model, near the interface between the concrete and the transition layer, massive calcite and montmorillonite precipitation decreases porosity again.

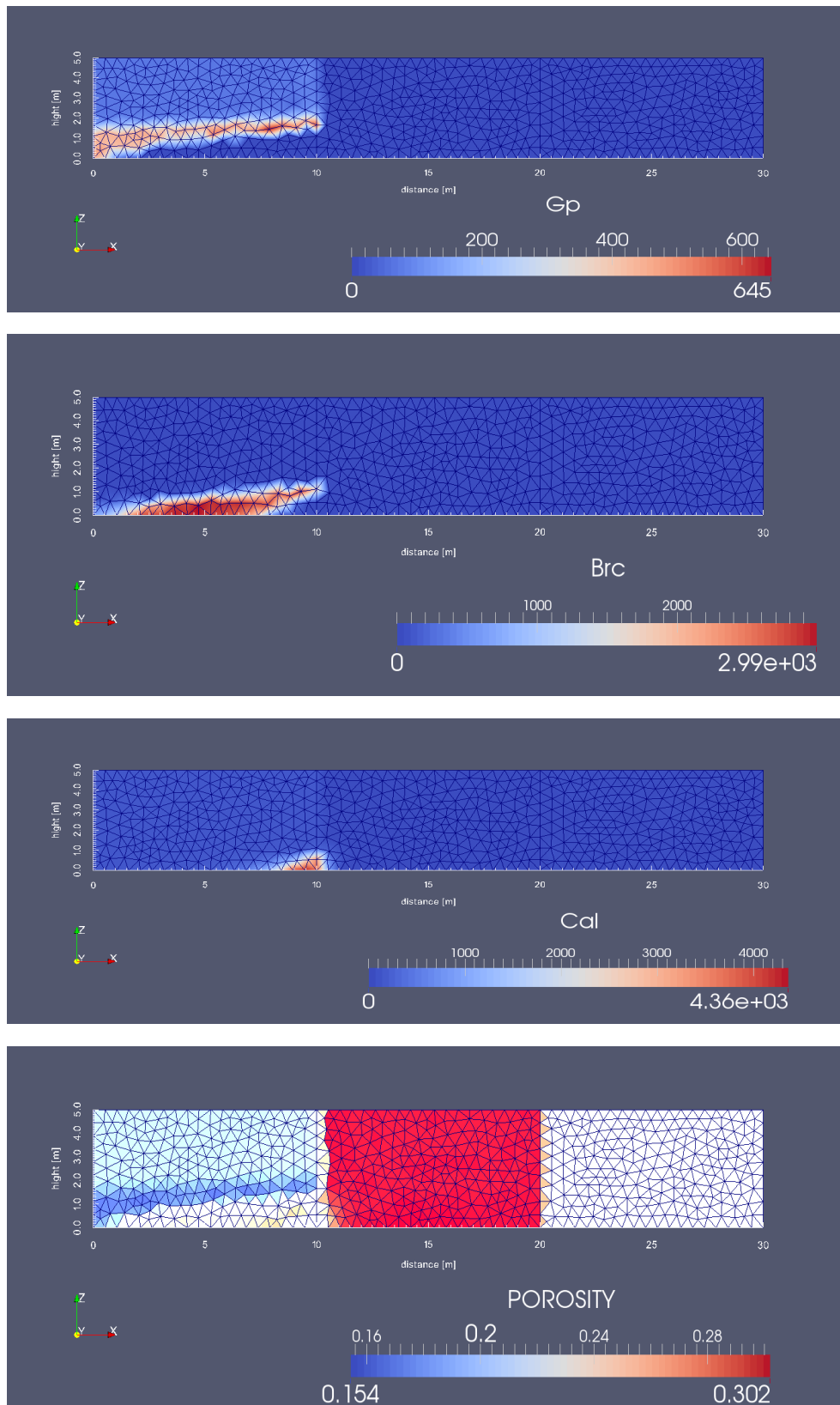


Fig. C-16: Concentration maps [mol/m³] for gypsum , brucite, calcite and map of porosity (from top to bottom) after 100 000 years using the 2-D model with a coarse discretisation.

Finally, Fig. C-17 shows the spatial distribution of pH. As explained in Section C.2.2, pH values in the desaturated part of the transition layer need to be interpreted with care. In the concrete, pH is largely buffered to a value of 10.2 if C-S-H is present. In the bottom part of concrete, pH is lowered to 10 in presence of hydrotalcite. Near the interface, where calcite and montmorillonite are precipitated, the pH drops to a value of 7.8, which is the pH of the inflowing clay water.

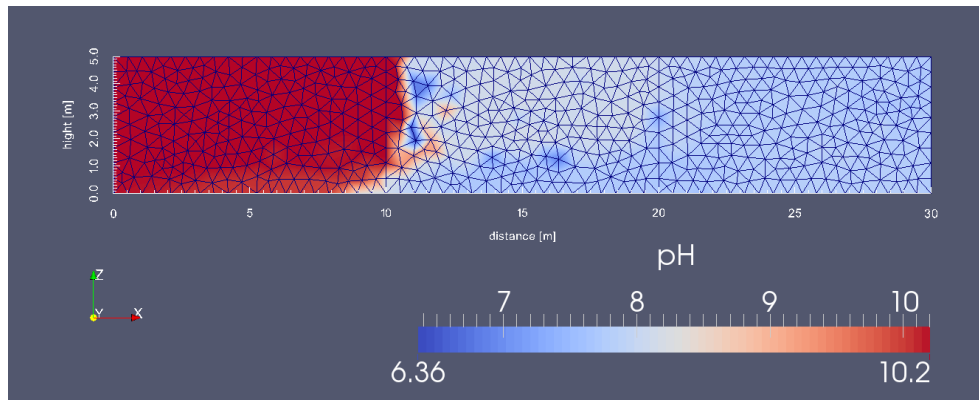


Fig. C-17: pH map after 100 000 years using the 2-D model with a coarse discretisation.

C.2.4 Summary of findings

As in the 2-D model case analysed in the main report (Section 3.3), chemical interactions in the saturated material at the bottom of the modelled system occur essentially as in the 1-D calculations. In particular, calculated mineralogical and porosity changes are similar in both model approaches. However, the 2-D model demonstrates that the extent and magnitude of mineralogical and porosity changes at material interfaces strongly depends on the change of diffusive and advective transport with saturation. Thus, changes towards the top of the modelled system are much more limited than towards the bottom.

In the present calculation case with quartz concrete aggregate, the saturation state does not influence the progress of concrete degradation by the ASR, as the residual liquid saturation of the concrete provides enough liquid to drive the reaction. The driving force for the ASR is a thermodynamic disequilibrium between cement minerals and the quartz aggregate. Only a minor amount of water is required to drive the ASR. The lower limit of saturation or water content that is necessary to drive ASR has to be determined independently.

Appendix D: Model Accuracy and Uncertainties

D.1 Influence of mesh size on porosity evaluation

The numerical mesh used to calculate system evolution has to resolve properly all concentration gradients at all places and at all times. For kinetically controlled calculations, a minimum mesh size exists below which no changes in the calculated system evolution will occur. The coupled code OpenGeoSys-GEM (Kosakowski & Watanabe 2013) was tested for the case of kinetically controlled porosity clogging due to mineral reactions in a diffusive transport regime with help of analytical solutions (Hayek et al. 2011, 2012; Kosakowski 2011). It was found that clogging times were reproduced very well, as long as all concentration gradients in the system at all times were spatially resolved (by the discretisation used). In Hayek et al. (2011, 2012), it is explained that numerical convergence cannot be achieved if equilibrium chemistry dissolution/ precipitation reactions are responsible for porosity clogging. For such a case, the connection between pore space evolution (on sub-grid scale) and porosity, as well as permeability/ diffusivity changes on continuum scale have to be calibrated by experiments or with help of upscaling procedures like in Tartakovsky et al. (2008).

If reactions with fast precipitation/dissolution kinetics are present, the necessary minimal mesh size might be very small (10^{-6} m or less), which leads to systems that cannot be calculated with current computing resources. For calculations that utilise equilibrium chemistry calculations such a minimal mesh size does not exist. Concentrations are set by the equilibria with solid phases and are often independent of transport processes. At clay/concrete interfaces, concentrations at the neighbouring nodes/elements forming the interface are typically very different for many species (as their solid phase assembly is very different), such that concentration gradients and porosity changes depend on the mesh size. Thus, as explained in Hayek et al. (2011, 2012) and Marty et al. (2009), the mesh size (element size of the numerical mesh) can be a critical value that determines porosity changes at geochemical fronts and hence, potentially, clogging times.

As illustrated in Fig. D-1, since concentration values at neighbouring nodes/element are set by chemical equilibrium, concentration gradients linearly depend on the node/element size. Diffusive fluxes between neighbouring nodes are also (linearly) proportional to the node/element size.

In such systems, porosity changes also depend on mesh size. Diffusive fluxes from one node/element to neighbouring nodes/elements are independent of the node/element volumes. They only depend on concentration gradients and effective diffusion coefficients. The diffusive fluxes will imply concentration changes that will be compensated by a geochemical re-equilibration with associated precipitation/dissolution of phases. The absolute amounts (volumes) of minerals that are precipitated or dissolved depend only on the amount of dissolved species that enter the node/element volume in a given time. The change in solid volume is also an absolute value, but the change in porosity is relative to the overall node/element volume. There is a linear dependence of volume changes (for a given dissolution/precipitation rate) on node/element volumes; smaller node/element volumes imply faster porosity changes than larger volumes (for a given diffusive flux into the element).

The combined effect of mesh size dependencies for concentration gradients and porosity changes give a square dependency for e.g. 1-D models of clogging time on node/element size (Marty et al. 2009).

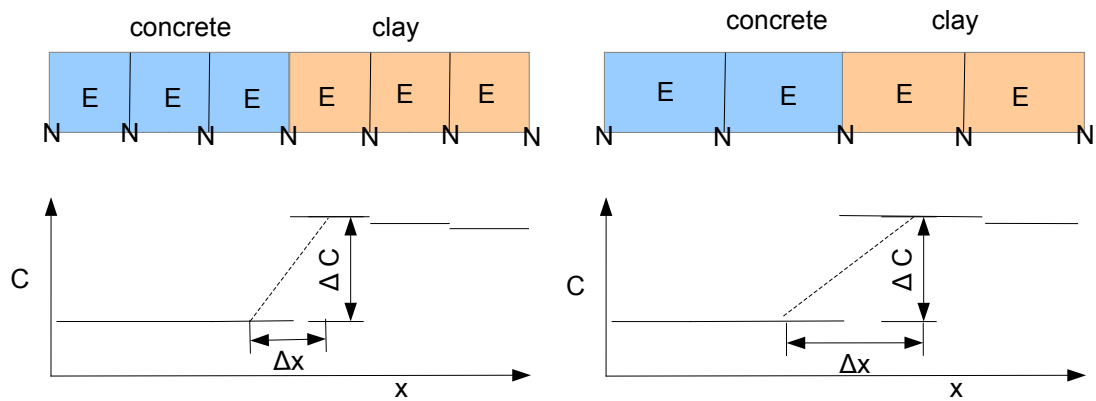


Fig. D-1: For nodes (N) and elements (E) where solute concentrations are fixed by mineral equilibria the concentration gradients between neighbouring nodes and elements may depend on the distance between nodes and element centers.

Changing the distance/size of nodes (elements), as illustrated by the differences in distance/size in the left- and right-hand diagrams, will change concentration gradients (for a quasi-stationary transport regime) and also change the volume which is associated with porosity changes.

For the calculations described in the main chapters of this report, it was found that porosity changes are small and often related to replacement of mineral phases with other minerals. In addition, dissolution fronts for accessory minerals in the transition layer move with different speed than dissolution front of cement minerals. This also implies, that the region where solute fluxes induced by these dissolution fronts meet and cause precipitation, move in time. There is no indication of strongly localised accumulation of specific mineral phases near the material interfaces which would clog the porosity for a refined mesh. In addition, discretisation influences the resolution of steep concentration gradients typically associated with reaction fronts. Typically, spatial progress of fronts is biased for early times associated with small distances that are not properly resolved in coarsely discretised models. In particular, as illustrated in Fig. D-2, it has been found that progress of a montmorillonite dissolution front might be slightly different in the coarsely discretised model, but the general mineralogical evolution does not differ and speed of dissolution fronts stabilises to the same values at both discretisations.

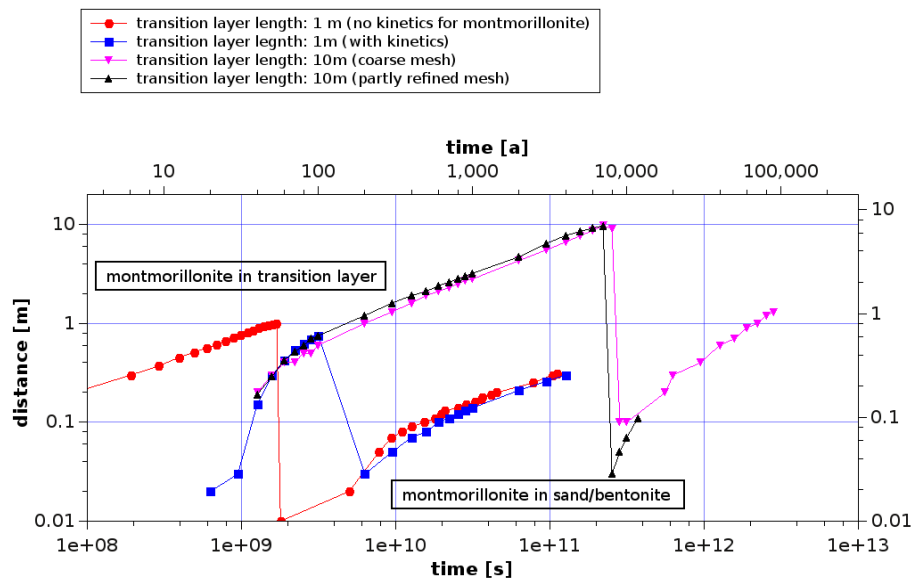


Fig. D-2: Progress of dissolution fronts for Na-montmorillonite with time.

In this figure distance refers to the front progress in each compartment.

For the transition layer the distance is calculated as distance from the concrete/transition layer interface. As soon as the dissolution front reaches the sand/bentonite the distance is calculated from the interface between transition layer and sand/bentonite.

D.2 Equilibrium chemistry vs. kinetic control of precipitation/dissolution

Earlier calculations of the evolution of cement/clay interfaces with OpenGeoSys-GEM, as reported in Berner et al. (2013) and Kosakowski et al. (2009), were based on equilibrium. More recent simulations have moved increasingly towards kinetic control of mineral precipitation/dissolution (Berner et al. 2013; Shao et al. 2013). In this section, we consider whether these two approaches give fundamental different results with respect to the mineralogical evolution, the evolution of pH and the change of porosity in the EGTS.

Comparison of equilibrium chemistry and kinetic control is not a straightforward task. For example, as explained in the previous section, the mesh size can influence the time behaviour of porosity changes and mineral transformations. In the following, the typical mesh size near the interfaces considered is set to 1cm in all cases, which is the same as the value used in Berner et al. (2013) and Kosakowski & Berner (2013), in all cases.

Fig. D-3 shows a comparison of mineralogical profiles of two model variants: a model based principally on equilibrium chemistry (except for quartz dissolution/precipitation in sand and gravel materials) and a model in which all mineral phases are kinetically controlled. In these calculations, the transition layer is filled with quartz gravel and quartz aggregate is used in the concrete (i.e. the system is the same as that in Fig. 4-5). There are no significant differences in the mineralogical evolution aside from differences in the small-scale oscillations discussed further Section D.3.

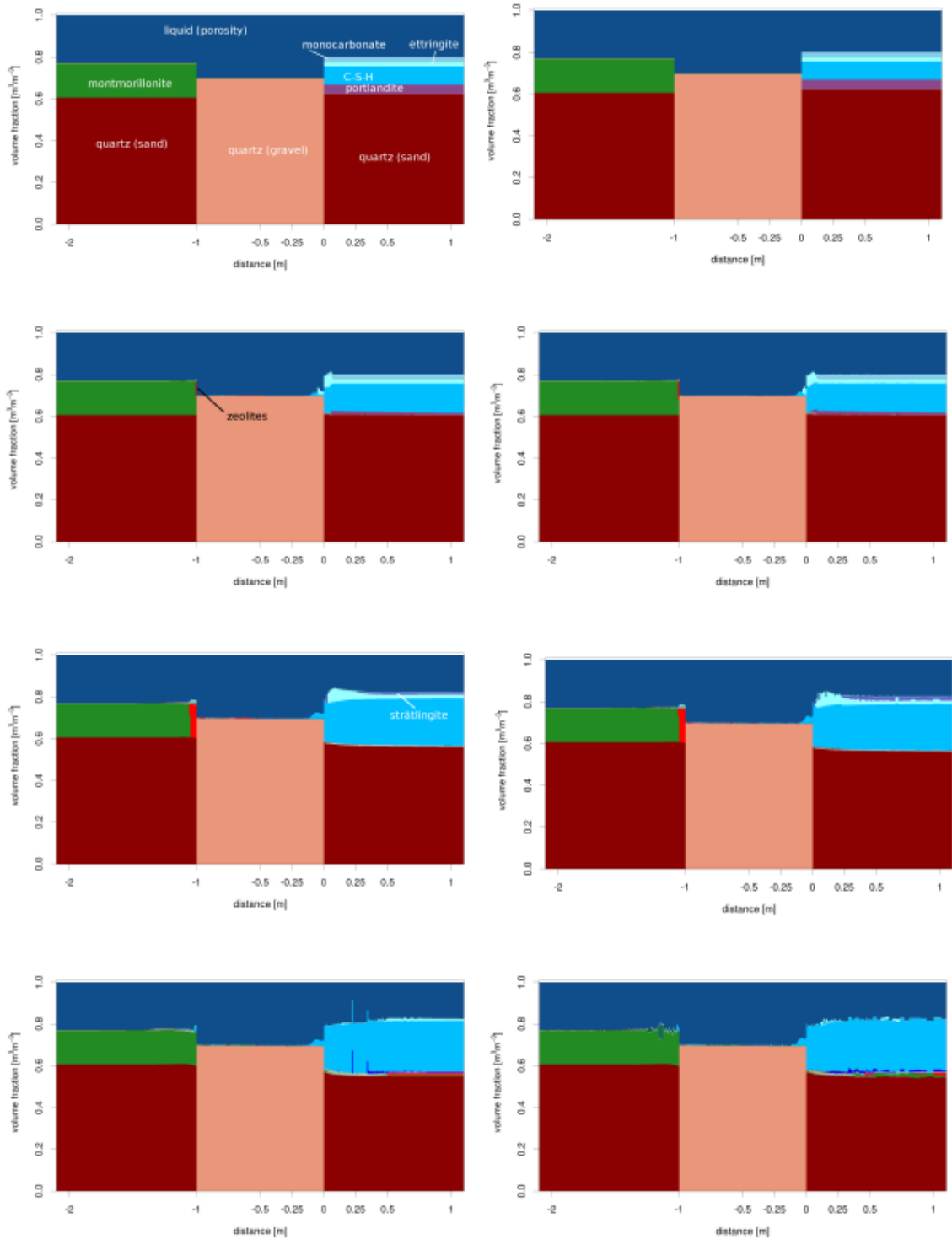


Fig. D-3: Mineralogical profiles at different times (0, 100, 500 and 2000 years) across a 1 m long transition layer composed of quartz gravel and with quartz aggregate in the concrete.

In the left-hand three figures, equilibrium chemistry is assumed except for quartz dissolution/precipitation in sand and gravel materials. The right-hand three figures show the results of a model that uses full kinetic control of all mineral phases.

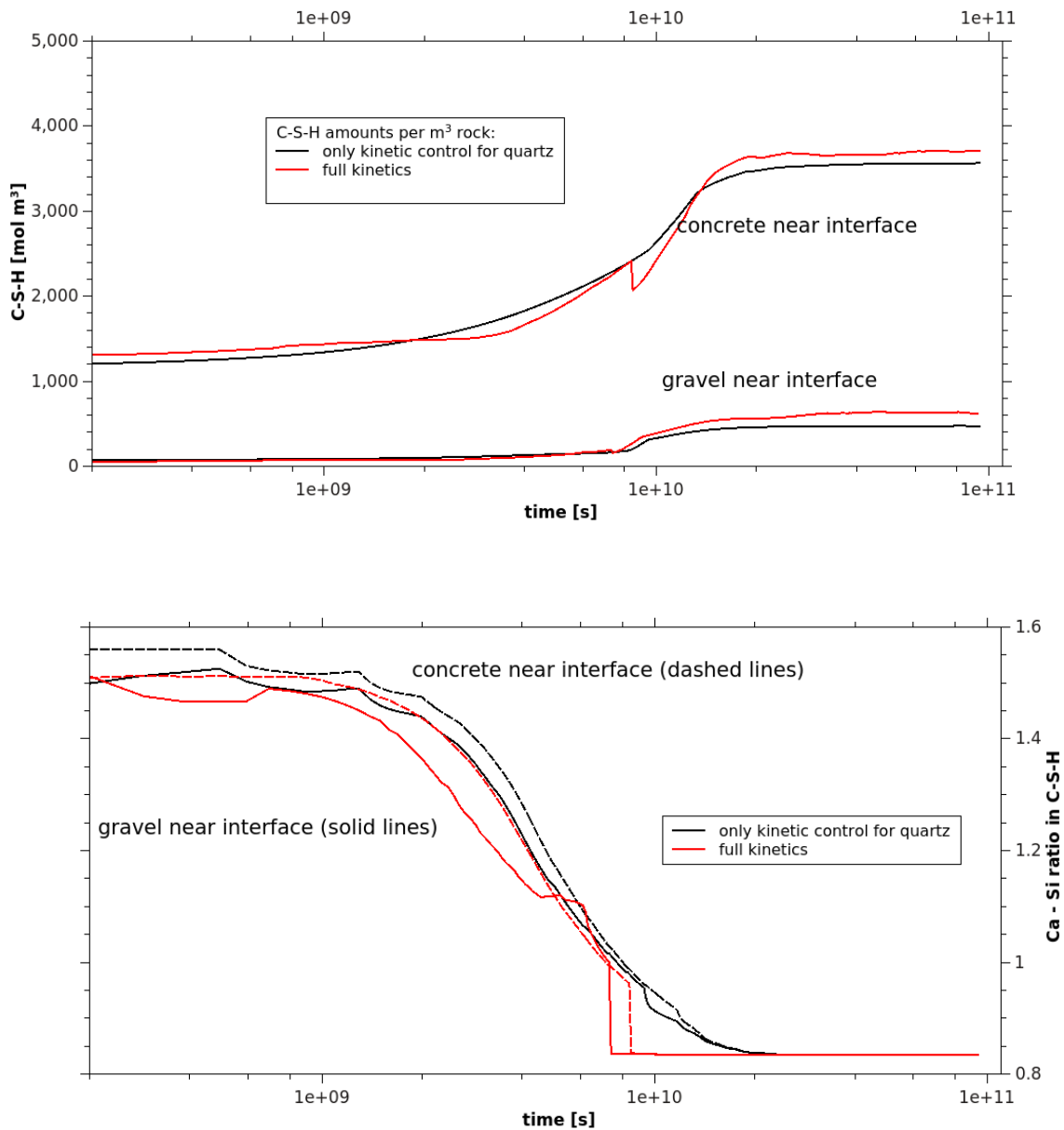


Fig. D-4: Amount of C-S-H (upper figure) and Ca-Si ratio in the C-S-H phase (lower figure) on both sides of the interface between the transition layer (gravel) and the concrete, calculated with a model variant based principally on equilibrium chemistry and with a variant in which all mineral phases are kinetically controlled.

The nearly identical mineralogical evolution in the two model variants is further illustrated in Fig. D-4, which shows the evolution of the total amount of the C-S-H solid solution and the evolution of the Ca-Si ratio in C-S-H within the transition layer and within the concrete on either side of the interface. The only notable difference is that, at late times, the variant with full kinetic control shows the C-S-H phase to be more enriched with Si compared with the other model variant.

Fig. D-5 shows a comparison of porosity evolution between the two model variants at various locations on either side of the model interfaces. Again, similar behaviour is observed for both model variants, although small absolute differences in porosity are visible. Differences between the model variants tend to increase with time. Comparison with Fig. D-4 shows that the oscillations in the kinetically controlled model influence porosity at individual nodes, which explains the increasing difference.

Finally, Fig. D-6 shows that pH evolution near the material interfaces is almost identical in the two model variants. In particular, the pH drop in the concrete is mainly driven by the kinetically controlled ASR reaction, which is identical in both variants. The above mentioned oscillations in pH are clearly visible in the kinetic model variant at long times.

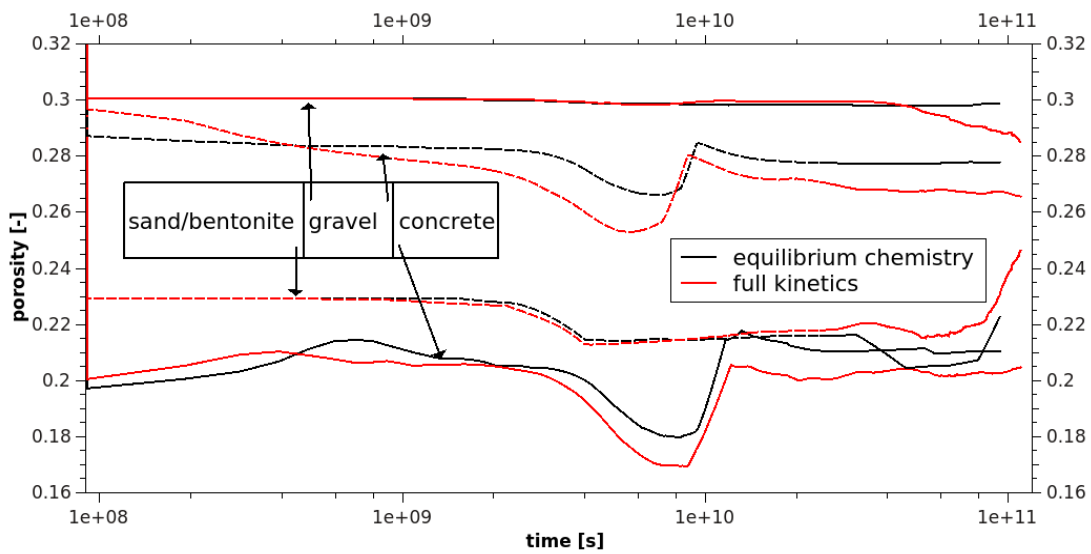


Fig. D-5: Porosity evolution near the material interfaces, calculated with a model variant based principally on equilibrium chemistry and with a variant in which all mineral phases are kinetically controlled.

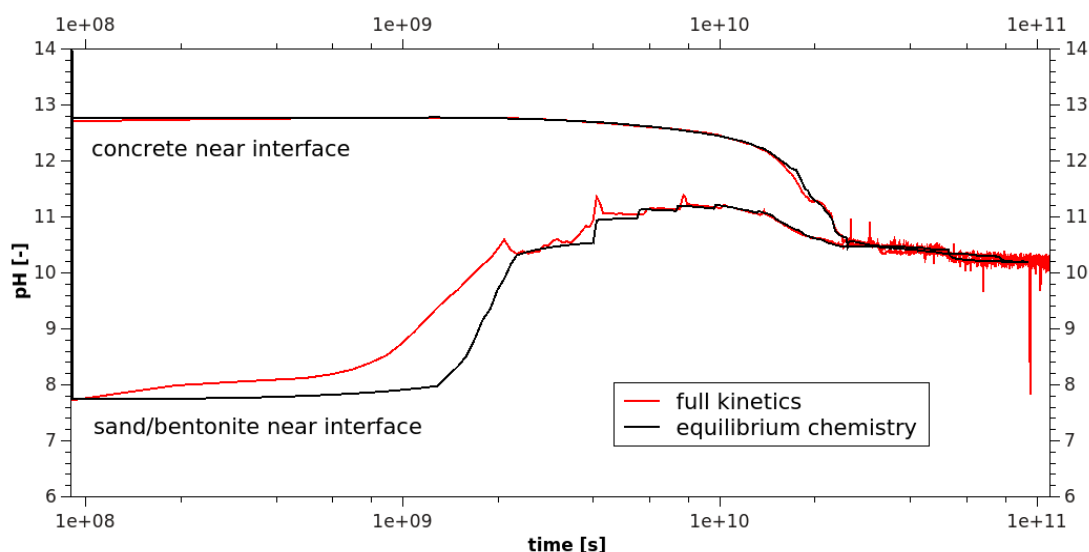


Fig. D-6: pH evolution near the material interfaces, calculated with a model variant based principally on equilibrium chemistry and with a variant in which all mineral.

D.3 Numerical oscillations in the simulations

In several of the mineralogical profiles presented in earlier sections of this report, numerical artefacts in the form of spatial oscillations are visible for certain mineral phases, especially in solid solution phases. From Figs. D-3 and D-6, it seems that the model with full kinetic control is more prone to oscillations in the numerical solution, although the model utilising mainly equilibrium chemistry is also affected. At the time of writing, it has not so far been possible to trace the exact causes for these oscillations. Possible causes include numerical artefacts from finite element (FE) solutions, inconsistencies in the thermodynamic setup, problems in mass balance or convergence of the GEMS solver, or a combination of such factors.

The influence of oscillations arising from the FE algorithm was tested using the newly implemented Flux Correction Transport (FCT) algorithm in OpenGeoSys (Kosakowski & Watanabe 2013). It was found that running models with FCT does not affect majority of the oscillations.

Some oscillations seem to be related to small changes in pH and redox potential. The solid solution model implemented for ettringite is known to be sensitive to GEMS numerical settings and tends to switch easily between different states¹². As the ettringite formulation contains sulphur and iron, which heavily influence redox conditions, small changes in the ettringite phase might give rise to stronger changes in other phases. The (kinetically controlled) montmorillonite solid solution model might behave in a similar manner, as montmorillonite includes an $\text{Fe}^{2+/3+}$ couple in the stoichiometric composition and also includes Fe in the ion exchange. The influence of the ettringite and hydrotalcite solid solutions was tested in one 1-D model scenario (calcite aggregate in the concrete and with a 10 m long layer of calcite gravel) by replacing the solid solution phases with single component phases of ettringite and hydrotalcite (Fig. D-7, right). The mineralogical profile does not show oscillations in the hydrotalcite profile, whereas the simulation with ettringite and hydrotalcite solid solutions (calcite aggregate in the concrete and with a 20 m long layer of calcite gravel) shows oscillations (Fig. D-7, left). In addition it was found that the strength of oscillations also depend on the GEMS numerical settings.

¹² Dmitrii Kulik, personal communication.

The observed oscillations seem not to affect the main features of system evolution calculated by the models. In particular, the porosity evolution (clogging) is not affected, as this is driven by interplay of transport and dissolution fronts. In order to maintain compatibility with earlier calculations related to the geochemical evolution of cement/ clay interfaces, the solid solution formation for ettringite and hydrotalcite was retained for the present calculations. For future calculations, an update of the thermodynamic setup will be considered.

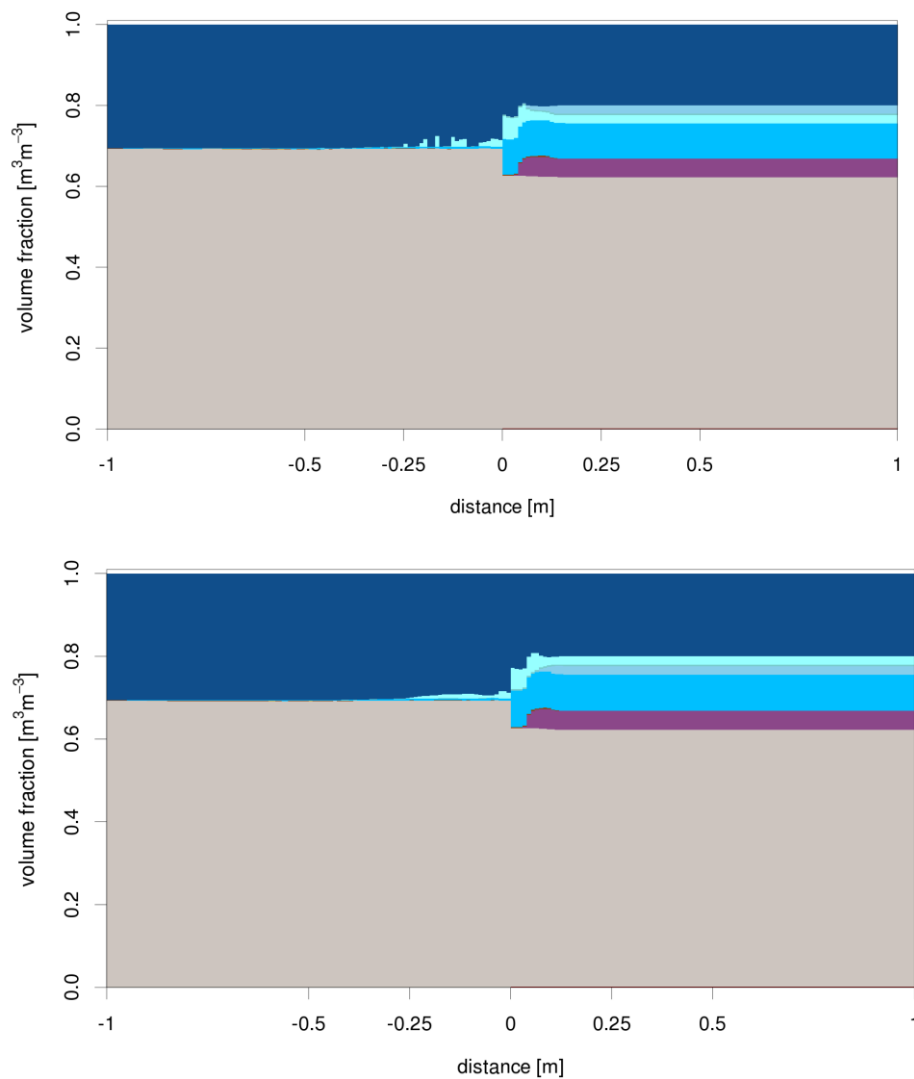


Fig. D-7: Mineralogical profiles after 300 years for a model variant that implements solid solutions for hydrotalcite and ettringite (top) and a variant with single components phases of these minerals (bottom).

D.4 CO₂ migration in the gas phase

The present models are not intended to reproduce two-phase flow phenomena in the EGTS. Rather, the focus is on simulating realistic liquid flow (in the case of the 2-D model) and aqueous-phase transport in partially saturated media. In the 2-D model, the calculated flow field and the corresponding saturation distribution are used to calculate saturation-dependent advective and diffusive transport of solutes. In both models, gases (CO₂, CH₄, H₂, O₂, H₂S) are included in the thermodynamic set-up as a separate gas phase and in the liquid phase as dissolved gases, but the models are set up such that a gas phase does not exist in the initial material setup. All gases only exist in dissolved form in the liquid phase and are transported like other dissolved species. The absence of explicit treatment of gas flow in the models does not allow transport of reactive gaseous species to be calculated.

According to Kosakowski et al. (2014) and Nagra (2008c), the gas phase after repository closure will be mainly composed of H₂ and some CH₄, both are assumed to not react with the EGTS materials. Transport of CO₂ in the gas phase could, however, be a significant additional mechanism which is currently not included in the 1-D or 2-D models. From calculated initial porewater compositions (Tab. A-2), it is clear that there is a substantial difference (about 10 log units) in CO₂ partial pressure between concrete and sand/bentonite. The different partial pressure is caused by mineral equilibria. If a gas phase is present, this could cause a higher CO₂ content in the sand/bentonite, whereas CO₂ would be removed from the gas phase in the concrete compartment due to carbonation reactions. This difference in gaseous CO₂ could cause a diffusive flux of CO₂ in the liquid and gas phases towards the concrete compartment. The transport of dissolved CO₂ in the liquid phase is included in the 1-D and 2-D models. The long-term calculations of the 2-D model show some carbonation of the concrete in the form of calcite precipitation near the gravel/concrete interface. In the models, the flux of CO₂ in the liquid phase was relatively minor and lead neither to fast accumulation of carbonates at the interface nor to a long term accumulation of calcite which was able to compensate the porosity increase due to cement leaching.

The magnitude of the CO₂ flux in the gas phase will depend on the saturation of the medium and the direction and magnitude of the advective gas transport. Due to the much higher diffusion coefficients of gases compared to in water dissolved species, fluxes of gaseous CO₂ that exceed fluxes of dissolved CO₂ seem possible.

The situation is comparable to concrete carbonation of constructions under atmospheric conditions, where a carbonation front moves into the concrete (Trotignon et al. 2011; Winter 2009). The in-diffusion of CO₂ transforms cement minerals (C-S-H, portlandite) into carbonates (calcite). Carbonation decreases porosity and lowers the pH towards 7. A detailed description of the carbonation process can be found for example in Glasser et al. (2008). Trotignon et al. (2011) simulated carbonation of concrete components in a deep geological radioactive waste disposal site during the operation period. They found that porosity changes range from a small increase to a moderate decrease. A test calculation on the concrete system, as defined in Appendix A, Tab. A-1 and Tab. A-2, revealed that one can expect a very small porosity increase after complete carbonation. It should be noted that carbonation requires the existence of a liquid phase in contact with the hydration products of concrete (Winter 2009), as the carbonation reaction involves dissolved CO₂ in the form of bicarbonate at neutral or slightly alkaline pH and carbonate at very alkaline pH. According to Winter (2009), carbonation proceeds most rapidly under humid but non-saturated conditions, with a relative humidity of 50 % – 70 %. Similar restrictions apply to the dissolution of calcite, which is limited by the availability of water and also controlled by the geochemical conditions (pH). For fully water saturated conditions, carbonation proceeds as discussed in Section 3.2.4, since transport of dissolved inorganic carbon is via the liquid phase only. As in the 1-D case, the accumulation of carbonate in

concrete due to transport of dissolved inorganic carbon is additionally prevented by elevated/reduced pH. Under completely dry conditions, carbonation will not occur since the water phase in contact with concrete hydration products is missing. Trotignon et al. (2011) give carbonation progress in the order of 0.6 to 1.1 mm/year. Winter (2009) gives a carbonation depth of 1 and 5 mm in the first year and states that the thickness of carbonation depth is proportional to the square root of time. It may be of interest to conduct a more detailed examination of this process with a reactive multi-phase transport code at some time in the future.

D.5 Mechanical effects

The models described in this report do not consider chemo-mechanical couplings, as taken into account for example in Idiart (2009), Idiart et al. (2011) and Multon et al. (2009a and b). In the present models, mineral precipitation causes porosity decrease with associated decrease in permeability and effective diffusivity, and may eventually leads to porosity clogging. In reality, processes like the ASR or ettringite precipitation caused by sulphate attack on concrete can lead to intensive cracking of the concrete due to crystallisation pressure (Taylor 1997; Winter 2009). This increases permeability and effective diffusivity, which would be favourable to gas transport. Note that, in the safety concept, the backfill of the waste emplacement rooms is not assigned any hydraulic barrier function.

Appendix E: Thermodynamic Data

E.1 Thermodynamic data for the 1-D modelling

GEM-Selektor v.2-PSI: Thermodynamic data for the modelling project:
EGS:GasTransportSystem: 27/11/2013 14:35

P(bar) = 1 T = 25 (C) = 298.15 (K) RT = 2478.97
Water: Ro(g/cm3) = 0.997061 Eps = 78.2451 Visc = 0.000554753

Tab. E-1: Thermodynamic data for Dependent Components (Species).

Record	Key	Flags	gTP	gEx_	VTP
a	Al Al (SO4) +	d + +	-1250429	0	-0.6019
a	Al Al (SO4) 2-	d + +	-2006304	0	3.1112
a	Al Al+3	d + +	-483708	0	-4.5243
a	Al AlO+	d + +	-660420	0	0.0307
a	Al AlO2-	d + +	-827479	0	0.9467
a	Al AlO2H@	d + +	-864277	0	1.3009
a	Al AlOH+2	d + +	-692595	0	-0.2728
a	AlSi AlHSiO3+2	r + +	-1540546	0	-4.0717
a	AlSi AlSiO4-	r + +	-1681439	0	2.5531
a	Ba Ba (CO3) @	d + +	-1104251	0	-1.1799
a	Ba Ba (HCO3) +	d + +	-1153325	0	1.9172
a	Ba Ba (SO4) @	d + +	-1320652	0	0.8182
a	Ba Ba+2	d + +	-560782	0	-1.2901
a	Ba BaOH+	d + +	-721077	0	0.9159
a	Ca Ca (CO3) @	d + +	-1099176	0	-1.5648
a	Ca Ca (HCO3) +	d + +	-1146041	0	1.3330
a	Ca Ca (SO4) @	d + +	-1310378	0	0.4701
a	Ca Ca+2	d + +	-552790	0	-1.8439
a	Ca CaOH+	d + +	-717024	0	0.5762
a	CaSi Ca (HSiO3) +	d + +	-1574238	0	-0.6737
a	CaSi CaSiO3@	r + +	-1517557	0	1.5693
a	Fe+2 Fe (CO3) @	d + +	-644487	0	-1.7228
a	Fe+2 Fe (HCO3) +	d + +	-689860	0	0.8184
a	Fe+2 Fe (HSO4) +	d + +	-853475	0	1.8806
a	Fe+2 Fe (SO4) @	d + +	-848806	0	0.1672
a	Fe+2 Fe+2	d + +	-91504	0	-2.2640
a	Fe+2 FeCl+	d + +	-223593	0	0.0846
a	Fe+2 FeOH+	d + +	-274461	0	-1.6713
a	Fe+3 Fe (HSO4) +2	d + +	-787148	0	0.2320
a	Fe+3 Fe (SO4) +	d + +	-784705	0	-0.2635
a	Fe+3 Fe (SO4) 2-	d + +	-1536813	0	3.0485
a	Fe+3 Fe+3	d + +	-17185	0	-3.7790
a	Fe+3 Fe2 (OH) 2+4	r + +	-491897	0	-3.9444
a	Fe+3 Fe3 (OH) 4+5	r + +	-964326	0	-4.1097
a	Fe+3 FeCl+2	d + +	-156923	0	-2.2857
a	Fe+3 FeCl2+	d + +	-291923	0	1.0272
a	Fe+3 FeCl3@	d + +	-417505	0	3.5941
a	Fe+3 FeO+	d + +	-222004	0	-4.2021
a	Fe+3 FeO2-	d + +	-368258	0	0.0452
a	Fe+3 FeO2H@	d + +	-419858	0	0.7209
a	Fe+3 FeOH+2	d + +	-241868	0	-2.5341

Tab. E-1: (continued).

Record Key	Flags	gTP	gEx_	VTP
a Fe+3Si FeHSiO3+2	r + +	-1087151	0	-3.3264
a K K(SO4)-	d + +	-1031773	0	2.7464
a K K+	d + +	-282462	0	0.9009
a K KOH@	d + +	-437107	0	1.4965
a Mg Mg(CO3)@	d + +	-998975	0	-1.6776
a Mg Mg(HCO3)+	d + +	-1047022	0	0.9343
a Mg Mg+2	d + +	-453985	0	-2.2014
a Mg MgOH+	d + +	-625868	0	0.1641
a Mg MgSO4@	d + +	-1211972	0	0.1812
a MgSi Mg(HSiO3)+	d + +	-1477145	0	-1.0850
a MgSi MgSiO3@	r + +	-1425031	0	1.2118
a Na Na(CO3)-	d + +	-797112	0	-0.0421
a Na Na(HCO3)@	d + +	-847394	0	3.2318
a Na Na(SO4)-	d + +	-1010336	0	1.8640
a Na Na+	d + +	-261881	0	-0.1208
a Na NaOH@	d + +	-418124	0	0.3509
a Si HSiO3-	d + +	-1014598	0	0.4526
a Si SiO2@	d + +	-833411	0	1.6063
a Si SiO3-2	r + +	-938510	0	3.4132
a Sr Sr(CO3)@	d + +	-1107830	0	-1.5228
a Sr Sr(HCO3)+	d + +	-1157538	0	1.4082
a Sr Sr(SO4)@	d + +	-1321366	0	0.5025
a Sr Sr+2	d + +	-563836	0	-1.7758
a Sr SrOH+	d + +	-725159	0	0.7099
a wC+4 CO2@	d + +	-386015	0	3.2807
a wC+4 CO3-2	d + +	-527982	0	-0.6058
a wC+4 HCO3-	d + +	-586940	0	2.4211
a wC-4 CH4@	d + +	-34354	0	3.7398
a wCl+7 ClO4-	d + +	-8535	0	4.3904
a wCl-1 Cl-	d + +	-131290	0	1.7341
a wH0 H2@	d + +	17729	0	2.5264
a wN0 N2@	d - +	18194	0	3.3407
a wO0 O2@	d + +	16446	0	3.0501
a wS+2 S2O3-2	d + +	-519989	0	2.7592
a wS+4 HSO3-	d + +	-529098	0	3.2957
a wS+4 SO3-2	d + +	-487886	0	-0.4116
a wS+6 HSO4-	d + +	-755805	0	3.4841
a wS+6 SO4-2	d + +	-744459	0	1.2918
a wS-2 H2S@	d + +	-27930	0	3.4951
a wS-2 HS-	d + +	11969	0	2.0210
a wS-2 S-2	r + +	120422	0	2.0210
a wX OH-	d + +	-157270	0	-0.4708
a w_ H+	d + +	0	0	0.0000
a w_ H2O@	d + +	-237181	0	1.8068
g C+4 CO2	d + +	-394393	0	2478.9712
g C-4 CH4	d + +	-50659	0	2478.9712
g H0 H2	d + +	0	0	2478.9712
g O0 O2	d + +	0	0	2478.9712
g S-2 H2S	d + +	-33752	0	2478.9712
s AlSiMgCaCa_Mont	r + +	-33705719	0	113.1977
s AlSiMgFeFe_Mont	r + +	-33244020	0	112.7775
s AlSiMgK K_Mont	r + +	-16862125	0	58.4217
s AlSiMgMgMg_Mont	r + +	-33606501	0	112.8402

Tab. E-1: (continued).

Record Key	Flags	gTP	gEx_	VTP
s AlSiMgNaNaMont	d + +	-16838107	0	57.4000
s AlSiMgSrSr_Mont	r + +	-33716765	0	113.2658
s CaSOH Tob-I	d + +	-4186454	22222	14.0800
s SiO Amor-Sl	d + +	-848903	22222	2.9000
s CaSOH Jennite	d + +	-2480808	0	7.8400
s CaSOH Tob-II	d + +	-1744356	0	5.8700
s CaAlOH C2AH8	d + +	-4812761	0	18.3860
s CaFeOH C2FH8	d + +	-3917378	0	19.3590
s CaAlOH C3AH6	d + +	-5010096	0	14.9702
s CaFeOH C3FH6	d + +	-4116295	0	15.5287
s CaAlOH C4AH13	d + +	-7326555	0	27.3980
s CaFeOH C4FH13	d + +	-6430942	0	28.5940
s CaAlOsH ettringite	d + +	-15205936	0	70.7030
s CaFeOsH Fe-ettringite	d + +	-14282356	0	71.7560
s CaAlOsH ettringite	d + +	-15205936	22222	70.7030
s CaFeOsH Fe-ettringite	d + +	-14282356	22222	71.7560
s CaAlOsH monosulphate	d + +	-7778504	0	30.9030
s CaFeOsH Fe-monosulphate	d + +	-6882552	0	32.1140
s CaAlOSH straetlingite	d + +	-5705148	0	21.6110
s CaFeOSH C2FSH8	d + +	-4809526	0	22.7000
s CaAlOcH hemicarbonate	d + +	-7335973	0	28.4515
s CaFeOcH Fe-hemicarbonate	d + +	-6440192	0	29.6472
s CaAlOcH monocarbonate	d + +	-7337459	0	26.1958
s CaFeOcH Fe-monocarbonate	d + +	-6679204	0	29.0190
s CaAlOH C4AH13	d + +	-7326555	0	27.3980
s CaAlOsH monosulphate	d + +	-7778504	0	30.9030
s CaAlOH C4AH13	d + +	-7326555	0	27.3980
s CaAlOsH monosulphate	d + +	-7778504	0	30.9030
s MgAlOH hydrotalcite	d + +	-6394560	0	22.0200
s MgFeOH Fe-hydrotalcite	d + +	-5498840	0	23.2400
s CaAlSiO Phillipsite_Ca	r + +	-8843044	5708	30.2299
s KAlSiO Phillipsite_K	r + +	-4440546	5708	14.8970
s NaAlSiO Phillipsite_Na	r + +	-4411974	5708	14.9681
s AlOH Gbs	d + +	-1150986	0	3.1956
s AlSiOH Kln	d + +	-3777714	0	9.9520
s BaCO witherite	r + +	-1137634	0	1.1309
s BaSO Brt	d + +	-1362152	0	5.2100
s CaAlOH CAH10	d + +	-4622388	0	19.3985
s CaCO Cal	d + +	-1129176	0	3.6934
s CaMgCO Ord-Dol	d + +	-2160289	0	6.4340
s CaOH Portlandite	d + +	-897013	0	3.3060
s CaSO Anh	d + +	-1322122	0	4.5940
s CaSO Gp	d + +	-1797763	0	7.4690
s CasOH hemihydrate	d + +	-1436340	0	6.1730
s FeCO Sd	d + +	-681647	0	2.9378
s FeO Mag_hyd	r + +	-1468946	0	11.6180
s FeOH Fe(OH)3(mic)	r + +	-711610	0	1.6415
s FeS Py	d + +	-173165	0	2.3940
s KMgAlSi Illite-Berchel	d + +	-5442750	0	13.9346
s CaKSOH syngenite	d + +	-2884913	0	12.7540
s MgCO Mgs	d + +	-1029275	0	2.8020
s MgOH Brc	d + +	-832227	0	2.4630
s SiO Qtz	d + +	-854793	0	2.2688

Tab. E-1: (continued).

Record Key		Flags	gTP	gEx_	VTP
SiO	Inert_Qtz	d + +	-854793	0	2.2688
s	SiO Qtz	d + +	-854793	0	2.2688
s	SrCO Str	d + +	-1144735	0	3.9010
s	SrSO Cls	d + +	-1346150	0	4.6250

Molar Gibbs energies are in J/mol, volumes in J/bar (0.1 cm³/mol).
 Flags: first column - data source (d-DComp, r-ReacDC);
 second column - on/off in the current system definition;
 third column - within (+) or out of (e) the source TP intervals.

E.2 Thermodynamic data for the 2-D modelling

GEM-Selektor v.2-PSI: Thermodynamic data for the modelling project:
 RefNew:new reference project: 10/12/2012 10:49

P(bar) = 1 T = 25 (C) = 298.15 (K) RT = 2478.97
 Water: Ro(g/cm3) = 0.997061 Eps = 78.2451 Visc = 0.000554753

Tab. E-2: Thermodynamic data for Dependent Components (Species).

Record	Key	Flags	gTP	gEx_	VTP
a	Al Al (SO4) +	d + +	-1250429	0	-0.6019
a	Al Al (SO4) 2-	d + +	-2006304	0	3.1112
a	Al Al+3	d + +	-483708	0	-4.5243
a	Al AlO+	d + +	-660420	0	0.0307
a	Al AlO2-	d + +	-827479	0	0.9467
a	Al AlO2H@	d + +	-864277	0	1.3009
a	Al AlOH+2	d + +	-692595	0	-0.2728
a	AlSi AlHSiO3+2	r + +	-1540546	0	-4.0717
a	AlSi AlSiO4-	r + +	-1681439	0	2.5531
a	Ba Ba (CO3) @	d + +	-1104251	0	-1.1799
a	Ba Ba (HCO3) +	d + +	-1153325	0	1.9172
a	Ba Ba (SO4) @	d + +	-1320652	0	0.8182
a	Ba Ba+2	d + +	-560782	0	-1.2901
a	Ba BaOH+	d + +	-721077	0	0.9159
a	Ca Ca (CO3) @	d + +	-1099176	0	-1.5648
a	Ca Ca (HCO3) +	d + +	-1146041	0	1.3330
a	Ca Ca (SO4) @	d + +	-1310378	0	0.4701
a	Ca Ca+2	d + +	-552790	0	-1.8439
a	Ca CaOH+	d + +	-717024	0	0.5762
a	CaSi Ca (HSiO3) +	d + +	-1574238	0	-0.6737
a	CaSi CaSiO3@	r + +	-1517557	0	1.5693
a	Fe+2 Fe (CO3) @	d + +	-644487	0	-1.7228
a	Fe+2 Fe (HCO3) +	d + +	-689860	0	0.8184
a	Fe+2 Fe (HSO4) +	d + +	-853475	0	1.8806
a	Fe+2 Fe (SO4) @	d + +	-848806	0	0.1672
a	Fe+2 Fe+2	d + +	-91504	0	-2.2640
a	Fe+2 FeCl+	d + +	-223593	0	0.0846
a	Fe+2 FeOH+	d + +	-274461	0	-1.6713
a	Fe+3 Fe (HSO4) +2	d + +	-787148	0	0.2320
a	Fe+3 Fe (SO4) +	d + +	-784705	0	-0.2635
a	Fe+3 Fe (SO4) 2-	d + +	-1536813	0	3.0485
a	Fe+3 Fe+3	d + +	-17185	0	-3.7790
a	Fe+3 Fe2 (OH) 2+4	r + +	-491897	0	-3.9444
a	Fe+3 Fe3 (OH) 4+5	r + +	-964326	0	-4.1097
a	Fe+3 FeCl+2	d + +	-156923	0	-2.2857
a	Fe+3 FeCl2+	d + +	-291923	0	1.0272
a	Fe+3 FeCl3@	d + +	-417505	0	3.5941
a	Fe+3 FeO+	d + +	-222004	0	-4.2021
a	Fe+3 FeO2-	d + +	-368258	0	0.0452
a	Fe+3 FeO2H@	d + +	-419858	0	0.7209

Tab. E-2: (continued).

Record Key			Flags	gTP	gEx_	VTP
a	Fe+3	FeOH+2	d + +	-241868	0	-2.5341
a	Fe+3Si	FeHSiO3+2	r + +	-1087151	0	-3.3264
a	K	K(SO4) -	d + +	-1031773	0	2.7464
a	K	K+	d + +	-282462	0	0.9009
a	K	KOH@	d + +	-437107	0	1.4965
a	Mg	Mg(CO3) @	d + +	-998975	0	-1.6776
a	Mg	Mg(HCO3) +	d + +	-1047022	0	0.9343
a	Mg	Mg+2	d + +	-453985	0	-2.2014
a	Mg	MgOH+	d + +	-625868	0	0.1641
a	Mg	MgSO4@	d + +	-1211972	0	0.1812
a	MgSi	Mg(HSiO3) +	d + +	-1477145	0	-1.0850
a	MgSi	MgSiO3@	r + +	-1425031	0	1.2118
a	Na	Na(CO3) -	d + +	-797112	0	-0.0421
a	Na	Na(HCO3) @	d + +	-847394	0	3.2318
a	Na	Na(SO4) -	d + +	-1010336	0	1.8640
a	Na	Na+	d + +	-261881	0	-0.1208
a	Na	NaOH@	d + +	-418124	0	0.3509
a	Si	HSiO3-	d + +	-1014598	0	0.4526
a	Si	SiO2@	d + +	-833411	0	1.6063
a	Si	SiO3-2	r + +	-938510	0	3.4132
a	Sr	Sr(CO3) @	d + +	-1107830	0	-1.5228
a	Sr	Sr(HCO3) +	d + +	-1157538	0	1.4082
a	Sr	Sr(SO4) @	d + +	-1321366	0	0.5025
a	Sr	Sr+2	d + +	-563836	0	-1.7758
a	Sr	SrOH+	d + +	-725159	0	0.7099
a	wC+4	CO2@	d + +	-386015	0	3.2807
a	wC+4	CO3-2	d + +	-527982	0	-0.6058
a	wC+4	HCO3-	d + +	-586940	0	2.4211
a	wC-4	CH4@	d + +	-34354	0	3.7398
a	wCl+7	ClO4-	d + +	-8535	0	4.3904
a	wCl-1	Cl-	d + +	-131290	0	1.7341
a	wH0	H2@	d + +	17729	0	2.5264
a	wO0	O2@	d + +	16446	0	3.0501
a	wS+2	S2O3-2	d + +	-519989	0	2.7592
a	wS+4	HSO3-	d + +	-529098	0	3.2957
a	wS+4	SO3-2	d + +	-487886	0	-0.4116
a	wS+6	HSO4-	d + +	-755805	0	3.4841
a	wS+6	SO4-2	d + +	-744459	0	1.2918
a	wS-2	H2S@	d + +	-27930	0	3.4951
a	wS-2	HS-	d + +	11969	0	2.0210
a	wS-2	S-2	r + +	120422	0	2.0210
a	wX	OH-	d + +	-157270	0	-0.4708
a	w_	H+	d + +	0	0	0.0000
a	w_	H2O@	d + +	-237181	0	1.8068
g	C+4	CO2	d + +	-394393	0	2478.9712
g	C-4	CH4	d + +	-50659	0	2478.9712
g	H0	H2	d + +	0	0	2478.9712
g	N0	N2	d - +	0	0	2478.9712
g	O0	O2	d + +	0	0	2478.9712

Tab. E-2: (continued).

Record Key	Flags	gTP	gEx_	VTP
g S-2 H2S	d + +	-33752	0	2478.9712
s AlSiMgBaBa_Mont	r + +	-33713711	0	113.7515
s AlSiMgCaCa_Mont	r + +	-33705719	0	113.1977
s AlSiMgFeFe_Mont	r + +	-33244020	0	112.7775
s AlSiMgK K_Mont	r + +	-16862125	0	58.4217
s AlSiMgMgMg_Mont	r + +	-33606501	0	112.8402
s AlSiMgNaNaMont	d + +	-16838107	0	57.4000
s AlSiMgSrSr_Mont	r + +	-33716765	0	113.2658
s CaSOH Jennite	d + +	-2480808	0	7.8400
s CaSOH Tob-II	d + +	-1744356	0	5.8700
s CaAlOH C2AH8	d + +	-4812761	0	18.3860
s CaFeOH C2FH8	d + +	-3917378	0	19.3590
s CaAlOH C3AH6	d + +	-5010096	0	14.9702
s CaFeOH C3FH6	d + +	-4116295	0	15.5287
s CaAlOH C4AH13	d + +	-7326555	0	27.3980
s CaFeOH C4FH13	d + +	-6430942	0	28.5940
s CaAlOsH ettringite	d + +	-15205936	0	70.7030
s CaFeOsH Fe-ettringite	d + +	-14282356	0	71.7560
s CaAlOsH ettringite	d + +	-15205936	0	70.7030
s CaFeOsH Fe-ettringite	d + +	-14282356	0	71.7560
s CaAlOsH monosulphate	d + +	-7778504	0	30.9030
s CaFeOsH Fe-monosulphate	d + +	-6882552	0	32.1140
s CaAlOSH straetlingite	d + +	-5705148	0	21.6110
s CaFeOSH C2FSH8	d + +	-4809526	0	22.7000
s CaAlOcH hemicarbonate	d + +	-7335973	0	28.4515
s CaFeOcH Fe-hemicarbonate	d + +	-6440192	0	29.6472
s CaAlOcH monocarbonate	d + +	-7337459	0	26.1958
s CaFeOcH Fe-monocarbonate	d + +	-6679204	0	29.0190
s CaAlOH C4AH13	d + +	-7326555	0	27.3980
s CaAlOsH monosulphate	d + +	-7778504	0	30.9030
s CaAlOH C4AH13	d + +	-7326555	0	27.3980
s CaAlOsH monosulphate	d + +	-7778504	0	30.9030
s KAlMgSiOIlliteEx-Al	r + +	-113101044	68496	283.3093 xx
s KAlMgSiOIlliteEx-Ca	r + +	-75633588	45664	190.0452 xx
s KAlMgSiOIlliteEx-Mg	r + +	-75534700	45664	189.6877 xx
s KAlMgSiOIlliteEx-Na	r + +	-37800246	22832	95.8237 xx
s KMgAlSi IlliteEx-K	d + +	-37827110	22832	96.8455 xx
s MgAlOH hydrotalcite	d + +	-6394560	0	22.0200
s MgFeOH Fe-hydrotalcite	d + +	-5498840	0	23.2400
s CaAlSiO Phillipsite_Ca	r + +	-8843044	5708	30.2299
s KAlSiO Phillipsite_K	r + +	-4440546	5708	14.8970
s NaAlSiO Phillipsite_Na	r + +	-4411974	5708	14.9681
s AlOH Gbs	d + +	-1150986	0	3.1956
s AlSiOH Kln	d + +	-3777714	0	9.9520
s BaCO witherite	r + +	-1137634	0	1.1309
s BaSO Brt	d + +	-1362152	0	5.2100
s CaAlOH CAH10	d + +	-4622388	0	19.3985
s CaAlSiO Laumontite	r + +	-6673304	0	15.7476 xx

Tab. E-2: (continued).

Record Key	Flags	gTP	gEx_	VTP
s CaAlSiO Mordenite	r + +	-6224436	0	18.7208 xx
s CaCO Cal	d + +	-1129176	0	3.6934
s CaMgCO Ord-Dol	d + +	-2160289	0	6.4340
s CaOH Portlandite	d + +	-897013	0	3.3060
s CaSO Anh	d + +	-1322122	0	4.5940
s CaSO Gp	d + +	-1797763	0	7.4690
s CasOH hemihydrate	d + +	-1436340	0	6.1730
s FeCO Sd	d + +	-681647	0	2.9378
s FeO Mag_hyd	r + +	-1468946	0	11.6180
s FeOH Fe(OH)3(mic)	r + +	-711610	0	1.6415
s FeS Py	d + +	-173165	0	2.3940
s CaKSOH syngenite	d + +	-2884913	0	12.7540
s MgCO Mgs	d + +	-1029275	0	2.8020
s MgOH Brc	d + +	-832227	0	2.4630
s NaAlSiO Analcime	r + +	-3065824	0	9.7481 xx
s SiO Qtz	d + +	-854793	0	2.2688
s SiO Inert_Qtz	d + +	-854793	0	2.2688
s SiO Qtz	d + +	-854793	0	2.2688
s SiO Qtz	d + +	-854793	0	2.2688
s SrCO Str	d + +	-1144735	0	3.9010
s SrSO Cls	d + +	-1346150	0	4.6250

Molar Gibbs energies are in J/mol, volumes in J/bar (0.1 cm³/mol).
 Flags: first column - data source (d-DComp, r-ReacDC);
 second column - on/off in the current system definition;
 third column - within (+) or out of (e) the source TP intervals.
 xx: data according to Shao et al. (2013)